Surface potentials of ceria and their influence on the surface exchange of oxygen

Zur Erlangung des akademischen Grades Doktor-Ingenieur (Dr.-Ing.)
genehmigte Dissertation von M.Sc. Hans Florian Wardenga aus Erkelenz
Tag der Einreichung: 4. April 2019, Tag der Prüfung: 12. Juli 2019
Darmstadt — D 17

1. Gutachten: Apl. Prof. Dr. Andreas Klein
2. Gutachten: Prof. Dr. Wolfgang Ensinger

TECHNISCHE
UNIVERSITÄT
DARMSTADT

Materials Science Department

Surface Science Division

Electronic Structure of Materials

Surface potentials of ceria and their influence on the surface exchange of oxygen

Genehmigte Dissertation von M.Sc. Hans Florian Wardenga aus Erkelenz

1. Gutachten: Apl. Prof. Dr. Andreas Klein
2. Gutachten: Prof. Dr. Wolfgang Ensinger

Tag der Einreichung: 4. April 2019
Tag der Prüfung: 12. Juli 2019

Darmstadt — D 17

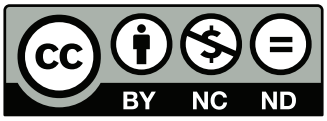

Erklärung zur Dissertation

Hiermit versichere ich, die vorliegende Dissertation ohne Hilfe Dritter nur mit den angegebenen Quellen und Hilfsmitteln angefertigt zu haben. Alle Stellen, die aus Quellen entnommen wurden, sind als solche kenntlich gemacht. Diese Arbeit hat in gleicher oder ähnlicher Form noch keiner Prüfungsbehörde vorgelegen.

Darmstadt, den 4. April 2019

(Hans Florian Wardenga)

Abstract

Cerium oxide is an important material for modern three-way catalysts for automotive exhaust emission control and an interesting candidate for the use in solid oxide fuel cells as electrode and electrolyte. For these application, the surface exchange of oxygen plays an important role as it is assumed, especially at lower temperatures, to be the limiting factor for the device performance.
The transfer of electrons from the oxide to adsorbed oxygen molecules is often discussed to be rate determining for the oxygen incorporation. Based on this assumption, this thesis will investigate a possible direct relation between the surface exchange coefficient k and the electrochemical potential of electrons, i.e. the Fermi level, at the CeO_2 surface. The absolute position of the Fermi level in reference to the vacuum energy is given by the work function of the material. Thus, following the hypothesis of this thesis, the work function of ceria should have a direct effect on the surface exchange coefficient.

This thesis constitutes a systematic investigation of the Fermi level, ionization potential and work function in dependence of surface orientation for acceptor-, donor- and undoped ceria thin films. The films, prepared by magnetron sputtering from ceramic targets, were analyzed using photoelectron spectroscopy. To obtain information about the crystal orientation of the films, X-ray diffraction was performed. In addition, oxygen tracer exchange experiments combined with secondary ion mass spectrometry and conductivity relaxation measurements were executed in collaboration with the IPC at RWTH Aachen for the purpose of determining the exchange and diffusion coefficients. From conductivity measurements at different temperatures and oxygen partial pressures the defect structure of CeO_2 was investigated by comparing the measured conductivities with calculations from a point defect model.

While a direct correlation of the work function with oxygen exchange coefficient could not be shown with ceria as a model system, this thesis provides new insights to CeO_2 surface potentials. Furthermore, it provides the first systematic study of these properties as a reference for other studies, where surface potentials of ceria are of importance.

Zusammenfassung

Ceroxid ist ein wichtiges Material für moderne Drei-Wege-Katalysatoren für die automobile Abgasnachbehandlung und ein vielversprechender Kandidat als Elektrode und Elektrolyt für die Verwendung in Festoxid-Brennstoffzellen. Für diese Anwendungen spielt der Austausch von Sauerstoff an der Oberfläche des Materials eine entscheidende Rolle, da vermutet wird, dass der Sauerstoff-Austausch, insbesondere bei niedrigen Temperaturen, der limitierende Faktor für die Bauteil Leistung ist.
Der Elektronentransfer vom Oxid zu adsorbierten Sauerstoffmolekülen wird häufig als ratenbestimmend für den Einbau von Sauerstoff angenommen. Auf Grundlage dieser Annahme wird diese Arbeit einen möglichen direkten Zusammenhang zwischen dem Austauschkoeffizienten k und dem elektrochemischen Potential der Elektronen, dem Fermi Level, an der CeO_2 Oberfläche untersuchen. Die absolute Position des Fermi Levels in Relation zur Vakuumenergie ist durch die Austrittsarbeit des Materials gegeben. Der Hypothese dieser Arbeit folgend, sollte daher die Austrittsarbeit von Ceroxid einen direkten Effekt auf den Sauerstoff-Austauschkoeffizient an der Oberfläche haben.
Diese Arbeit stellt eine systematische Untersuchung des Fermi Levels, Ionisationspotentials und der Austrittsarbeit in Abhängigkeit der Oberflächenorientierung von Akzeptor-, Donator und undotierten Ceroxid Dünnschichten. Die Schichten, welche durch Magnetron-Kathodenzerstäubung von keramischen Targets hergestellt wurden, wurden mittels Photoelektronen-Spektroskopie analysiert. Um Informationen über die kristallographische Orientierung der Schichten zu erlangen, wurden Röntgenbeugungs-Messungen durchgeführt. Zusätzlich wurden Sauerstoff-Tracer Austausch-Experimente in Kombination mit Sekundärionen-Massenspektrometrie und Leitfähigkeits-Relaxations Messungen, in Kollaboration mit dem IPC an der RWTH Aachen, durchgeführt um Austausch- und Diffusionskoeffizienten zu bestimmen. Durch Leitfähigkeits-Messungen bei verschiedenen Temperaturen und Sauerstoff-Partialdrücken wurde die Defektstruktur von CeO_2 untersucht, indem die gemessenen Leitfähigkeiten mit Berechnungen aus einem Punktdefekt-Model verglichen wurden.
Obwohl eine direkte Korrelation zwischen Austrittsarbeit und Sauerstoff-Austauschkoeffizient mit Ceroxid als Modellsystem nicht gezeigt werden konnte, bietet diese Arbeit neue Erkenntnisse zu CeO_2 Oberflächenpotentialen. Desweiteren stellt diese Arbeit die erste systematische Studie dieser Eigenschaften als eine Referenz für andere Forschungsfelder, in denen die Oberflächenpotentiale von Ceroxid von Bedeutung sind.

Contents

1 Introduction

Cerium dioxide is a mixed ionic electronic conductor, which shows a good reducibility and oxygen storage capacity. These properties make it an important material for heterogeneous catalysis. Due to the good CO oxidation and water-gas-shift reaction rates of catalysts on ceria based supports, CeO_2 is of great importance for three-way catalysts for exhaust emission control in automotive applications [1–3]. In addition, ceria is an interesting candidate for the use in solid oxide fuel cells (SOFC) working at intermediate temperature [4–10]. The good ionic conductivity of acceptor-doped ceria makes it a suitable electrolyte material. Furthermore, the mixed ionic and electronic conductivity enables the use of CeO_2 as electrode material for SOFCs.

A key feature for these applications is the exchange of oxygen at the surface, especially in an intermediate temperature regime, where the oxygen exchange can become a limiting factor for the device performance. While oxygen incorporation into a material consists of several processes, including adsorption, charge transfer, dissociation, and surface and bulk diffusion, the rate determining step for oxygen exchange in most oxides is expected to be electron transfer [11–13].

In order to incorporate oxygen into an oxide semiconductor, the gaseous O_2 has to be reduced to O^{2-}. The necessary electrons for the reduction are typically provided by the semiconductor. Thus, the transfer of an electron to an adsorbate should depend on the potentials of the electrons in the material compared to the adsorbate. In Fig. 1.1a the surface potentials of a semiconductor are shown. In general, the influence of the Fermi level (E_F) and work function (ϕ) of the semiconductor on heterogeneous catalysis has been discussed in literature for some time [14–17]. However, surface potentials are rarely considered in more recent discussions, despite their importance on gas reactions at semiconductor surfaces. Figure 1.1b illustrates the effect of the work function of CeO_2 on the electron transfer to an oxygen adsorbate. If the vacuum energy levels (E_{vac}) of ceria and the oxygen molecule are aligned, there will be an energetic barrier for electron transfer from ceria to oxygen depending on the work function of CeO_2 and the electron affinity (χ) of adsorbed O_2. The work function, on the other hand, depends on the Fermi level and the ionization potential (I_P). A variation of the Fermi energy can be achieved by doping. I_P is typically affected by surface termination and orientation of the material [18].

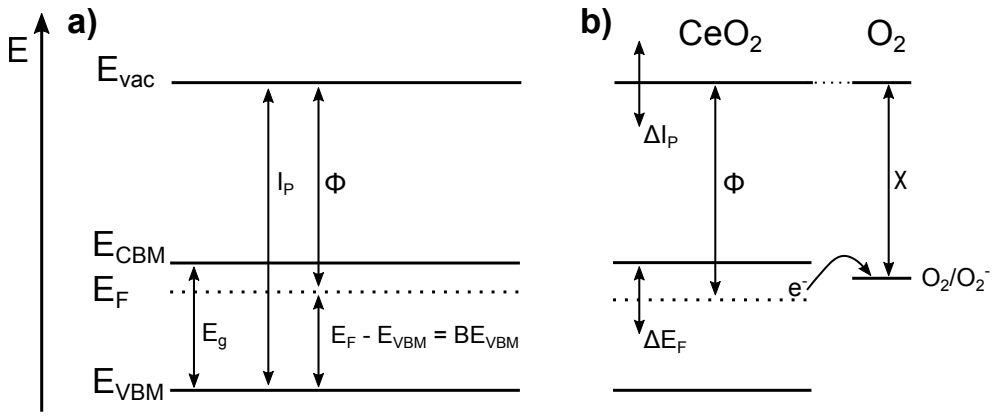

Fig. 1.1: a) Definition of surface potentials with E_g, E_F, E_{CBM}, E_{VBM}, E_{vac}, I_P and ϕ as band gap, Fermi level, conduction band minimum, valence band maximum, vacuum level, ionization potential and work function, respectively. b) Schematic model for electron transfer from the semiconductor to adsorbed oxygen including the effect of the work function. The lower the work function of the semiconductor, the lower is the activation energy for electron transfer. The work function depends on the ionization potential and the Fermi energy.

The goal of this thesis is a systematic investigation of the influence of the surface potentials on the oxygen exchange. CeO_2 is chosen as a model system, due to its relevance in applications and, primarily, since its bulk properties and defect model are fairly well understood in literature [19–28]. Variation of the Fermi level position of CeO_2 is accomplished by doping with Gd or Nb as acceptor or donor, respectively. In addition, undoped ceria thin films are investigated. For the purpose of varying the ionization potential, differently oriented thin films are prepared. Further variations of I_P due to a change of surface termination are investigated by thin film deposition under reducing or oxidizing conditions.

The surface potentials within this thesis are determined by photoelectron spectroscopy. In a second step, the obtained data on surface potentials are compared to oxygen exchange data of doped and undoped CeO_2 from conductivity relaxation measurements and tracer exchange experiments. For better comparability of the samples prepared in this work with literature reports, conductivity measurements in dependence of temperature and oxygen partial pressure are performed.

2 Basics

2.1 Bulk structure of CeO_2

2.1.1 Crystal structure of CeO_2

CeO_2 crystallizes in the cubic fluorite structure (space group Fm-3m) in which Ce forms a face centered cubic (fcc) lattice and oxygen is occupying the octahedral voids. The lattice parameter is $a = 5.411$ Å and the bulk density is 7.22 g/cm^3 [29, 30]. A schematic of the structure is shown in Fig. 2.1.

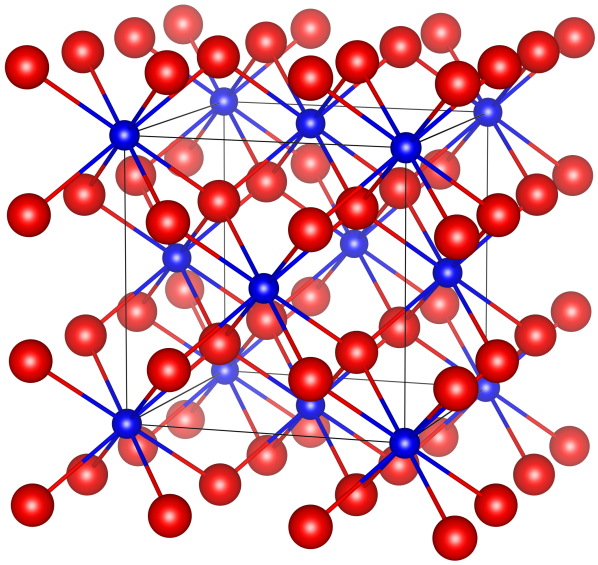

Fig. 2.1: Crystal structure of CeO_2 with Ce (blue) forming an fcc lattice and O (red) occupying the octahedral voids. Drawn with VESTA [31].

2.1.2 Electronic structure of CeO_2

CeO_2 is a wide band gap semiconductor with a fundamental energy gap of 3 eV [32–34]. The valence band consists of O2p states, while Ce4f states form the conduction band (see Fig. 2.2a). As a consequence of the low dispersion of the f-bands, the effective mass of the electrons (m_e^*) is very high. Contrary to a charge transport in a conventional semiconductor, where the charge carriers can move freely within the corresponding bands, the electrons in CeO_2 are strongly localized on a Ce atom, forming a small polaron [35].

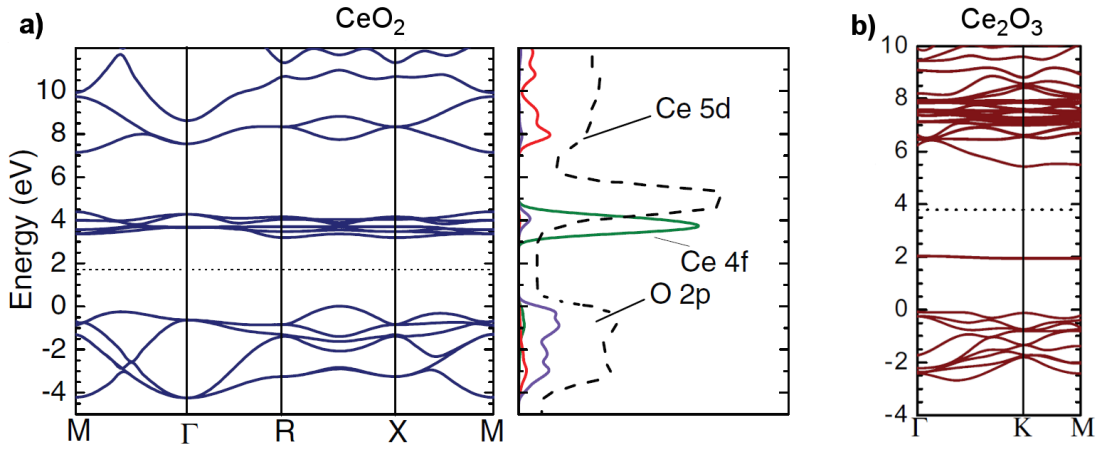

Fig. 2.2: a) Band structure and (partial) density of states of CeO_2 and b) band structure of Ce_2O_3 as calculated from HSE06. The dashed (grey) line in the DOS plot depicts the experimentally measured DOS from Ref. [32] for comparison. The valence band maximum was chosen as the zero energy. The dotted lines in the band structure plots depict the Fermi energy. From Fig. 1 and Fig. 3 from Ref. [33]. Reprinted figures with permission from R. Gillen, S. J. Clark, and J. Robertson, Phys Rev B, vol. 87, no. 125116, 2013. Copyright 2013 by the American Physical Society.

Generally, a polaron is a quasiparticle formed by an electron (or hole) with the potential of the atomic displacement caused by itself [36, 37]. Polarons can be divided into large and small polarons depending on their radius. Transport of large polarons can often be treated similar as free electrons with high effective masses, accounting for the "drag" of the caused lattice distortion. However, this classical model does not represent small polarons very well. A small polaron is characterized by its radius in the order of a unit cell, in which the electron is trapped on an atom by the potential of the self induced ionic displacement [37]. In order to move, the electron has to first overcome the energy of the trapping potential before it can jump to the next atom, where it forms a polaronic state again. This process is referred to as *hopping* [35, 37, 38].

When CeO_2 is reduced to Ce_2O_3 the band structure changes. Due to the reduction of Ce^{4+} to Ce^{3+} the electronic configuration changes from unoccupied f-states ($4f^0$) to an occupied f-state ($4f^1$). As a consequence of this, the f-band shifts down in energy by more than 1 eV in Ce_2O_3 compared to CeO_2 (see Fig. 2.2b) [33].

2.2 Structure of CeO_2 surfaces

In order to discuss the influence of surface orientation on surface potentials (cf. chapter 5) one has to take the structure of the surface into account. Within this thesis, CeO_2 films

with three different orientations were investigated: (111), (110) and (100) oriented films were considered because they represent type II, type I and type III surfaces according to the classification of polar surfaces by Tasker [39, 40], respectively. A schematic drawing of the bulk truncated surfaces for these orientations is shown in Fig. 2.3.

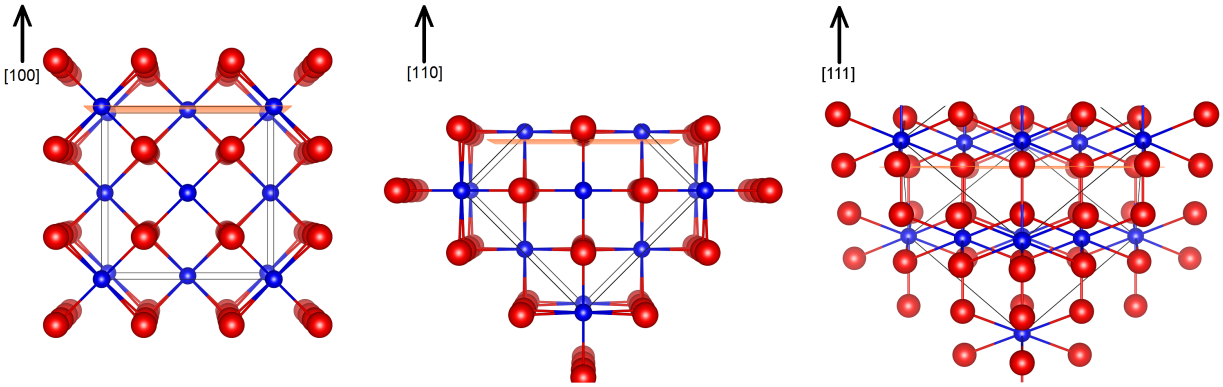

Fig. 2.3: Side view on the bulk truncated (100), (110) and (111) surfaces of CeO_2. Ce and O atoms are shown as blue and red balls, respectively. Drawn with VESTA [31].

Tasker type I and type II surfaces are typically non-polar in contrast to polar type III surfaces (see Figure 2.4). Bulk truncated type III surfaces have an electrical dipole moment perpendicular to the surface (μ_d), which will result in high surface energies. In general, to reduce the surface energy and stabilize the surface, surface reconstruction occurs. Especially surfaces with a high electrical dipole moment (type III) are expected to reconstruct [39]. In the following, a short overview of possible surface reconstructions for the (111), (110) and (100) surfaces of CeO_2 will be given.

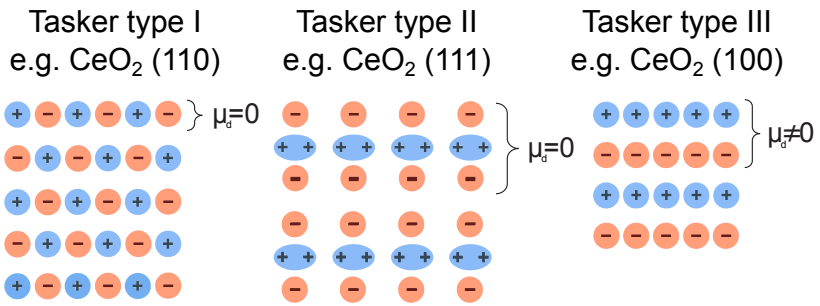

Fig. 2.4: Schematic Tasker classification for low-index crystal surfaces of CeO_2.

The (111) surface has been reported to be O terminated and not expected to show a significant reconstruction of the surface [41–46]. Only a small contraction of the first atomic layers is expected perpendicular to the surface [45, 46]. Furthermore, reduced surfaces show an ordering of oxygen vacancies in a triangular arrangement and line defects for strongly reduced surfaces [44, 47].

The type I (110) surface of ceria is also expected to be oxygen terminated. Skorodumova *et al.* predicted a small inwards relaxation of Ce at the surface resulting in an O

termination [45]. In addition, there is a wide agreement about the occurrence of {111} nanofacets on the (110) surface [41, 48, 49]. Lin *et al.* reported that the (110) surface is made up of around 40 % of {111} facets [41]. This indicates that the (111) surface is more stable than the (110) surface, which is also the case for the analogous In_2O_3 surface with its bixbyite structure similar to the fluorite structure [50–52]. Yang *et al.* report that the (110) surface is made of partially reduced (110) terraces and {111} nanofacets [49]. Additionally, they suggest a possible (2x1) reconstruction of the reduced (110) surface, where 25 % of O is missing, which means that the stoichiometry is resembling a Ce_2O_3 layer. From grazing-emission XPS they evaluated a high Ce^{3+} concentration of 60 cat.% for the (2x1) surface, which is in good agreement with the results from high-resolution electron microscopy (HREM) by Lin *et al.* who measured an oxygen vacancy surface concentration around 30 % on (110) terraces [41]. Furthermore, Yang *et al.* found the reduced (2x1) reconstructed surface difficult to reoxidize [49]. The authors suggested, that the adjacent oxygen next to a surface oxygen vacancy moves toward that vacancy into a bridging site between two Ce atoms, thus, blocking the path for the new O atom. In Fig. 2.5 the reconstruction of the (110) according to Yang *et al.* is illustrated.

A significant reconstruction is expected for the polar (100) CeO_2 surface. Early studies have shown an oxygen termination of the surface [45, 53]. In order to have no dipole moment perpendicular to the surface, half of the oxygen from the outer layer has to be removed [53]. Calculations of surface energies have revealed that an O terminated surface with half of the oxygen removed in a checkerboard style manner is the most stable (100) surface arrangement which would be equivalent to a $(\sqrt{2} \times \sqrt{2})R45°$ reconstruction [45]. Nörenberg *et al.* suggest from results of low energy electron diffraction and scanning tunneling microscopy a $\frac{\sqrt{2}}{2}(3 \times 2)R45°$ reconstruction of the oxidized (100) surface by an oxygen coverage of 50 % while the cerium in the second layer is reduced to Ce^{3+} [53]. They calculated that further reduction of the surface is energetically favorable compared to reduction in the bulk up to an oxygen coverage of 25 %, which would correspond to a complete reduction of all Ce atoms in the second layer. In more recent studies, the reconstruction of the surface with half of the oxygen missing was reported to be oversimplified and also Ce, O and CeO terminated parts were found on {100} surfaces of CeO_2 nanocubes with HREM [41]. Due to the combination of this mixed termination of the outer surface layer and partially occupied near-surface region, the authors suggest a 'quenched' surface dipole. However, the exact surface reconstruction of ceria is still under discussion in literature.

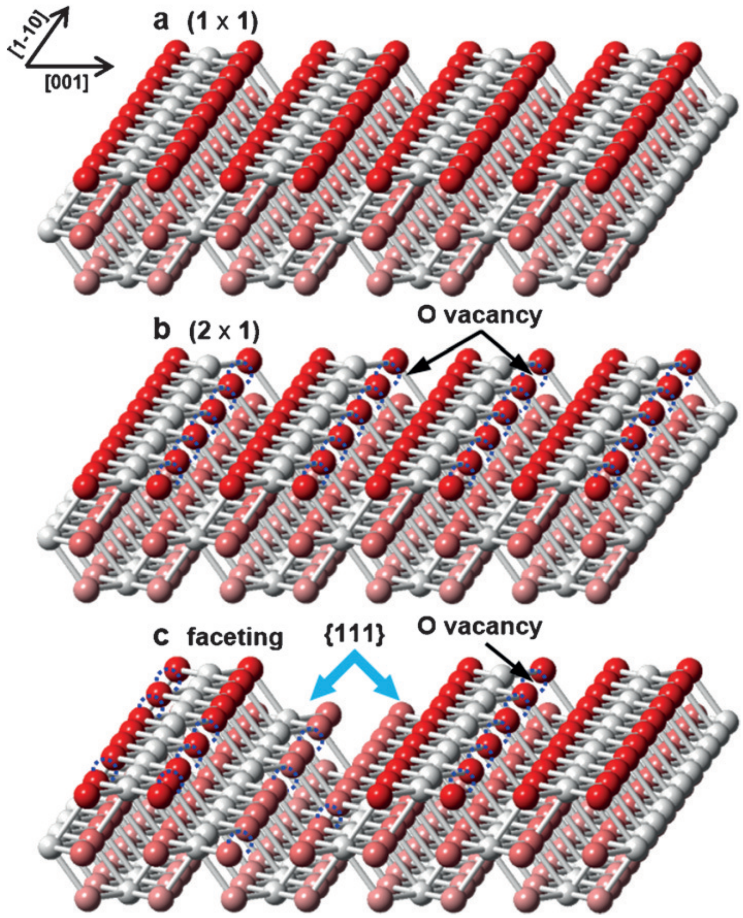

Fig. 2.5: "Structure evolution during the reduction of the CeO_2(110) surface. a) The stoichiometric, fully oxidized (1x1) phase. b) (2x1) Reconstruction. c) {111} Nanofaceting. The oxygen vacancies are indicated by dashed circles." [49]

2.3 Oxygen incorporation

For oxygen incorporation into an oxide, two main processes need to be considered: oxygen exchange and diffusion, characterized by the exchange coefficient k and the diffusivity D. In the first step, oxygen has to pass the surface of the material to be able to diffuse further into the bulk in the second step. While in general D is the proportionality coefficient between a particle flux and the gradient of the chemical potential of the particle (Fick's First Law), the chemical exchange coefficient k_{chem} is equal to the rate constant of the surface exchange reaction.

2.3.1 Oxygen exchange reaction at the surface

The process of incorporating oxygen from its molecular, gaseous state into an oxide as twofold charged oxygen anion can be divided into the following partial reactions [11, 54][1]:

$$1: \quad O_2(g) \rightleftharpoons O_2(ad) \tag{2.1}$$

$$2: \quad O_2(ad) + e' \rightleftharpoons O_2'(ad) \tag{2.2}$$

$$3: \quad O_2'(ad) + e' \rightleftharpoons 2O'(ad) \tag{2.3}$$

$$4: \quad O'(ad) + e' \rightleftharpoons O''(ad) \tag{2.4}$$

with the corresponding reaction rates:

$$r_1 = K_1 pO_2 \tag{2.5}$$

$$r_2 = K_1 K_2 n pO_2 \tag{2.6}$$

$$r_3 = (K_1 K_2 K_3)^{\frac{1}{2}} n pO_2^{\frac{1}{2}} \tag{2.7}$$

[1] Following the Kröger-Vink notation $'$ and $^\bullet$ denote a negative and positive charge, respectively [55].

$$r_4 = (K_1 K_2 K_3)^{\frac{1}{2}} K_4 n^2 \mathrm{pO}_2^{\frac{1}{2}} \tag{2.8}$$

K_i is the rate constant of each equation i, pO_2 the oxygen partial pressure and n is the concentration of electrons. For an oxygen bulk transport via a vacancy mechanism, the adsorbed anion is finally incorporated as shown in Eq. 2.9. Eq. 2.10 is the reaction rate of the last partial reaction including the molar fraction of oxygen vacancies $[\mathrm{V}_\mathrm{O}^{\bullet\bullet}]$ [54].

$$5\mathrm{a}: \quad \mathrm{O}''(\mathrm{ad}) + \mathrm{V}_\mathrm{O}^{\bullet\bullet} \rightleftharpoons \mathrm{O}_\mathrm{O}^{x} \tag{2.9}$$

$$r_{5\mathrm{a}} = (K_1 K_2 K_3)^{\frac{1}{2}} K_4 K_{5\mathrm{a}} n^2 [\mathrm{V}_\mathrm{O}^{\bullet\bullet}] \mathrm{pO}_2^{\frac{1}{2}} \tag{2.10}$$

Analogous to this, if the dominating oxygen transport mechanism is not by vacancies, but by an interstitial mechanism, the final incorporation step is given by:

$$5\mathrm{b}: \quad \mathrm{O}''(\mathrm{ad}) \rightleftharpoons \mathrm{O}_\mathrm{i}'' \tag{2.11}$$

$$r_{5\mathrm{b}} = (K_1 K_2 K_3)^{\frac{1}{2}} K_4 K_{5\mathrm{b}} n^2 [\mathrm{O}_\mathrm{i}'']^{-1} \mathrm{pO}_2^{\frac{1}{2}} \tag{2.12}$$

with the reaction rate including the molar fraction of oxygen interstitials $[\mathrm{O}_\mathrm{i}'']$.

2.3.2 Conversion of exchange and diffusion coefficients

Depending on how the exchange and diffusion coefficients were obtained, they describe different processes. It can be distinguished between the chemical diffusion D_{chem}, self diffusion $\mathrm{D}_{V,i}$ (index V and i for transport via vacancies and interstitials, respectively) and tracer diffusion D^* coefficients. While D_{chem} describes diffusion driven by a gradient in the chemical potential, self diffusion and tracer diffusion characterize the movement of an atom or isotopic tracer, without a directional driving force. This is the reason why self and tracer diffusion coefficients are similar except for a tracer correlation factor f_i, which depends on coordination number in the crystal lattice and transport mechanism [56, 57].

$$D^* = f_i D_{V,i} \tag{2.13}$$

For diffusion via oxygen vacancies in CeO_2 the correlation factor is $f_i = 0.6555$ [58, 59], for diffusion via interstitial oxygen $f_i = 0.9855$ [60], if the defect concentrations are low. For the conversion of self diffusion to chemical diffusion coefficient one has to take into account, that the gradient of the chemical potential itself changes due to the diffusion. This is corrected by dividing the self diffusivity by the thermodynamic factor ω_0 [56, 58, 59]:

$$D_{chem} = \omega_0 D_{V,i} \tag{2.14}$$

$$\omega_0 = \frac{1}{2}\left(\frac{\partial \ln pO_2}{\partial \ln c_O}\right) \tag{2.15}$$

with the oxygen partial pressure pO_2 and the concentration of oxygen c_O in the material. If the defect model of the material is known, and thus the defect concentrations in dependence on temperature and oxygen pressure, the thermodynamic factor can be calculated.
The conversion of tracer exchange k^* to chemical exchange coefficient k_{chem} can be performed analogously with Eq. 2.16.

$$k_{chem} = \omega_0 k^* \tag{2.16}$$

2.4 Conductivity, diffusivity and surface exchange coefficient of CeO_2

This section will give a short overview over typical values for the conductivity, diffusion and exchange coefficients of doped- and undoped CeO_2 reported in literature. In order to understand the conductivity, diffusion and oxygen surface exchange of doped- and undoped ceria, a closer look at the defect chemistry of CeO_2 is necessary. In section 3.4 an introduction into the defect model of ceria will be given.

2.4.1 Conductivity of CeO_2

The conductivity of acceptor- [4, 13, 61–69] and undoped [35, 69–71] ceria has been studied intensively in the past decades. In comparison, only few reports exist about the conductivity of donor-doped CeO_2 [26, 28]. Table 2.1 gives a short overview of reported conductivities (σ) from literature. Since Gd-doped ceria is mostly an ionic conductor, the electronic conductivity (σ_e) is negligible and only ionic conductivities (σ_i) are listed. On the other hand, for undoped and Nb-doped CeO_2 the conductivity is determined by

the electronic part. However, Guo *et al.* determined the the ionic component of the conductivity by impedance spectroscopy for undoped ceria [71]. The reported values of the conductivity and activation energies for similarly doped material vary significantly. The reason for this is likely the different morphology of the samples (grain size, strain, etc.) caused by the different sample preparation routes. In addition, the measurement type is an important factor. As can be seen in Table 2.1, the ionic transport within the grain is favored compared to the transport across grain boundaries. Therefore, the grain size and the measurement mode (in-plane or out-of-plane) have a significant influence on the measured values.

Table 2.1: Conductivites of acceptor-, donor- and undoped CeO_2 from literature reports. σ_i and σ_e are the ionic or electronic conductivities, respectively, at the measuring temperature T_m with the corresponding activation energy $E_{a,\sigma}$ for the transport within the grain (g) or grain boundary (gb).

Ref.	σ_i (S/cm)	σ_e (S/cm)	T_m (°C)	$E_{a,\sigma}$ (eV)	sample type
Gd-doped CeO_2					
[61]	6.3×10^{-3}		600	0.86	thin film
[62]	1.4×10^{-4}		600	1.33	thin film
[63]	9.0×10^{-3}		600	g: 0.42 / gb: 0.92	thin film
[66]	5×10^{-3}		500	g: 0.9 / gb: 1.0	ceramic
[69]	3×10^{-3}		700	1.2	thin film
[69]	4×10^{-2}		700	0.7	thin film
[4]	2.5×10^{-2}		600	0.64	ceramic
undoped CeO_2					
[35]		$3-10 \times 10^{-1}$	600		single crystal
[69]		5×10^{-3}	700	1.5	thin film
[71]	g: 1 × 10—4 gb: 1 × 10—6		700 700	g: 0.8 gb: 1.7 − 2	ceramic
Nb-doped CeO_2					
[28]		1×10^{-5} 4×10^{-3}	300	0.66 0.58	thin film
[26]		1.3×10^{-1}	644	0.34	ceramic

2.4.2 Diffusivity and surface exchange coefficient of CeO_2

Since the conductivity of Gd-doped ceria is mostly ionic over a wide temperature and oxygen partial pressure range, the oxygen diffusivity can be determined from conductivity data with the Nernst-Einstein relation (cf. Eq. 3.14 in section 3.4). However, determining the exchange coefficient is more complicated and typically done by tracer exchange experiments combined with secondary ion mass spectrometry (SIMS). Values for D^* and k^* for 10 mol% Gd-doped CeO_2 ceramic samples have been reported by Manning *et al.* [12]. They reported tracer diffusion coefficients from 5.2×10^{-14} to 5.2×10^{-11} m^2/s in

a temperature range from 475 to 1050 °C with an activation energy of 0.9 eV. The exchange coefficient has been reported ranging from 2.1×10^{-12} to 5.4×10^{-8} m/s within the same temperature interval. The activation energy of k^* has been reported to be 0.6 eV for temperatures below 700 °C and 3.3 eV for temperature above 700 °C [12].
Kamiya *et al.* reported tracer diffusion and exchange coefficients for undoped CeO_2 bulk ceramics [72]. With an activation energy of 2.34 eV for D^* between 800 and 1300 °C, tracer diffusion coefficients from 2.2×10^{-14} up to 8.7×10^{-12} m^2/s were determined. The surface exchange coefficient increased in the same temperature interval from 3.0×10^{-10} to 7.1×10^{-8} m/s with an eactivation energy of 1.4 eV.
To the author's best knowledge, there are no published results for oxygen diffusion or exchange coefficients for donor-doped CeO_2. The determination of D and k for Nb-doped ceria are a part of this work and will be shown in detail in section 6.2 and chapter 8. The determination of these values will be performed mostly by conductivity relaxation measurements (cf. section 3.3).

3 Methods and experimental procedure

3.1 Preparation of thin film samples

Thin films of cerium oxide were deposited by radio frequency magnetron sputtering from ceramic targets with a diameter of 2" and a purity of 99.99 %. The nominally undoped CeO_2 (UDC) target was purchased from Kurt J. Lesker Company. Nb- and Gd-doped ceria targets were purchased from EVOCHEM Advanced Materials. The targets had a specified doping concentration of 1 wt.% Nb_2O_5 (NDC), 1 wt.% Gd_2O_3 (GDC1) and 10 wt.% Gd_2O_3 (GDC10), which equals to atomic concentrations of 1.3 at.% Nb, 0.95 at.% Gd and 9.5 at.% Gd, respectively. The films were deposited with a sputter power of 25 W and a total pressure of 0.5 Pa. The resulting deposition rate at a target-to-substrate distance of 7 cm was around 1 nm/min. Films were deposited with 100 % Ar or a 10 % O_2/90 % Ar mixture as process gas at substrate temperatures of 300, 500 and 600 °C. In order to further vary surface conditions, post deposition annealing was conducted for 2 h at 700 °C in 0.5 Pa Ar or vacuum ($< 10^{-7}$ mbar) and by annealing for 1.5 h at 400 °C in H_2O [73]. For the latter treatment, the H_2O pressure in the chamber was controlled by an atomic layer deposition (ALD) valve connected to a reservoir of purified water. By continuously pumping the ALD chamber and opening the valve for 300 ms every 30 s, a H_2O pressure of 10^{-4} to 10^{-3} Pa was adjusted. In addition, films were annealed under oxidizing condition (0.5 Pa O_2) for 2 h at 700 °C or treated for 15 min under an oxygen plasma from a GenII plasma source (tectra) operated in atom mode.

To avoid charging of the samples during photoelectron spectroscopy, the used substrates had to be electrically conductive and the films relatively thin with thicknesses between 20 and 80 nm. The films were deposited on Al_2O_3(0001)/Pt(111), MgO(110)/Pt(110) and $SrTiO_3$(100) (STO) single crystals doped with 0.05 wt.% Nb. Single crystal substrates were purchased from CrysTec. The Pt(111) and Pt(110) films on Al_2O_3(0001) and MgO(110), respectively, were deposited by direct current magnetron sputtering with a sputter power of 5 W in 0.5 Pa Ar at a substrate temperature of 650 °C. With a deposition time of 60 min and a target-to-substrate distance of 7.5 cm, the resulting Pt layer thickness is around 150 nm.

In addition, films on insulating substrates were prepared for conductivity measurements. Here, the search for suitable substrates for differently orientated films turned out to be challenging, since most substrates that could enable epitaxial growth of CeO_2 were

electrically too conducting at the high temperatures required for the conductivity measurement of the thin films. In the end, suitable substrates for all orientation could not be found. Therefore, the films for conductivity measurements were deposited only on Al_2O_3(0001) substrates. Their film thickness was between 300 and 900 nm. The film thicknesses of thin films with a thickness up to 100 nm were determined by X-ray reflectivity [74], while the thickness was determined by profilometry for thicker films.

All film depositions and post-deposition annealing were carried out in the oxide 3 chamber of the Darmstadt's Integrated System for Materials Research (DAISY-MAT). Annealing with H_2O exposure was performed in an ALD chamber. An additional "quenching" experiment was executed in the oxide 0 chamber. For this experiment, a GDC10 film was annealed at 600 °C at defined oxygen pressures from 2×10^{-5} bar stepwise down to 4×10^{-11} bar[1] and subsequently quenched to room temperature. This experiment was carried out in the oxide 0 chamber due to the possibility there to transfer the hot sample directly from the heater to a steel block to enable fast cooling rates. From 600 °C to 300 °C an average cooling rate of 75 K/min was achieved. The cooling rate decreased significantly below 300 °C. It took approximately 30 min for the sample to cool below 80 °C.

It should be noted, that substrate temperatures above 600 °C during the ceria deposition resulted in very low deposition rates (< 0.1 nm/min). For this reason, the films were not directly deposited at 700 °C, but had to be deposited at 600 °C and were annealed immediately after the deposition at 700 °C. Another issue with the deposition was a contamination of the films with F and Cl, as was found with secondary ion mass spectroscopy. The origin of this contamination could not be identified. Possible F sources that could be ruled out were the adhesive on the graphite contact pads used for target mounting and the supporting polymer within the glass fiber cable insulation from the sample heater. Other sources could have been polytetrafluoroethylene (PTFE), which is sometimes used as seal in valves and could release fluorine when heated in vacuum, or it might be present as an impurity in the sputter target. However, fluorine was found in films from all four different targets from two manufacturers. This means, that either the F is a contamination from the production of the CeO_2 raw material or that the fluorine contamination in the films comes from an unidentified source during the deposition process.

[1] It should be noted that the lowest oxygen pressure from the last step was only estimated from the specified oxygen impurity of the Ar gas, i.e. the actual oxygen partial pressure might be lower.

3.2 Photoelectron spectroscopy measurements

Photoelectron spectroscopy measurements (PES) were executed with a PHI 5700 spectrometer (Physical Electronics), which is attached to the DAISY-MAT. This enables in situ PES measurements without exposure of the samples to air for avoiding surface contamination by adsorption of hydrocarbons and water. X-ray photoelectron spectroscopy (XPS) measurements were carried out with monochromatic Al-Kα radiation with an energy of 1486.6 eV at an emission angle of 45° and with a pass energy of 5.85 eV. For ultraviolet photoelectron spectroscopy (UPS) an excitation energy of 21.22 eV (HeI radiation) was used. UPS measurements were executed in normal emission and with a pass energy of 2.95 eV. In addition a bias of −4 V was applied to the sample for the UPS measurements. The spectrometer was calibrated using a sputter cleaned silver specimen for both pass energies on a daily basis.

The stoichiometry of the samples was determined using equation 3.1 with c_i as the concentration, I_i the integrated intensity of the emission line and S_i the corresponding atomic sensitivity factor of the element i [75, 76]. The used atomic sensitivity factors are summarized in Table 3.1. For peak fitting and the determination of the stoichiometry a Shirley background correction was performed [77].

$$c_i = \frac{I_i/S_i}{\sum_i I_i/S_i} \tag{3.1}$$

Table 3.1: Atomic sensitivity factors (S) from [78].

Element	Emission line	S
Ce	3d	7.399
O	1s	0.711
Gd	4d	2.207
Nb	3d	2.517

In Fig. 3.1 exemplary survey spectra for undoped (UDC) and 1.3 cat.% Nb-doped (NDC) CeO_2 and ceria films doped with 0.95 cat.% Gd (GDC1) and 9.5 cat.% Gd (GDC10) deposited at 300 °C in 100 % Ar atmosphere are shown. For UDC, all peaks can be attributed to cerium or oxygen. The Nb- and Gd-concentration in NDC and GDC1, respectively, is below the detection limit of the XPS. This is partly owned to the fact, that the peaks with the highest intensity of Nb and Gd overlap with emission lines from Ce. The Nb3d emission line overlaps with Ce4p and Gd3d overlaps with Ce3p$_{3/2}$. For this reason the dopant concentration could only be determined for GDC10. In order to avoid

the peak overlap, the Gd4d emission line was used to evaluate Gd content in the GDC10 films.

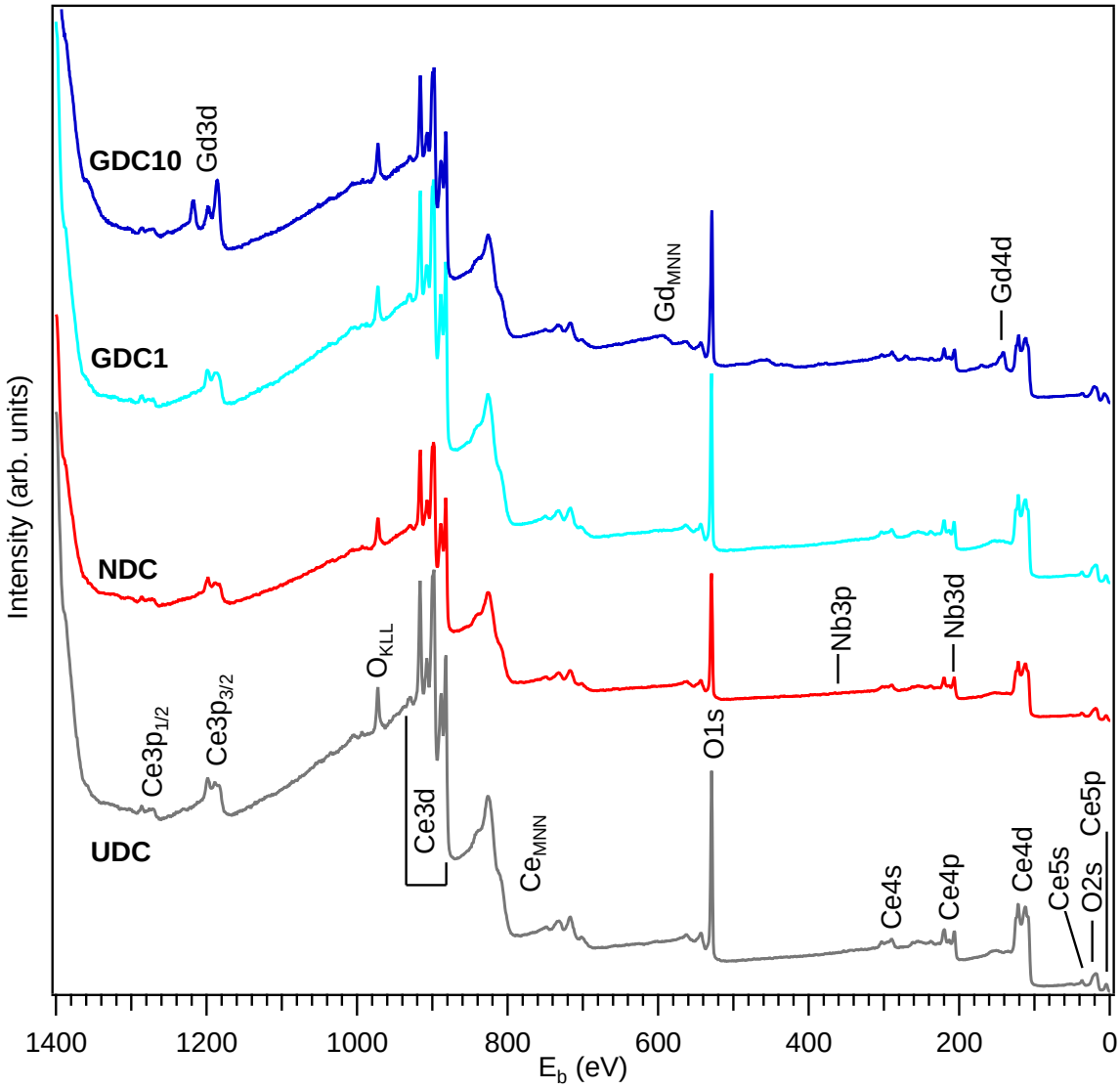

Fig. 3.1: XP survey spectra of undoped (UDC) and 1.3 cat.% Nb-doped (NDC) CeO_2 and ceria films doped with 0.95 cat.% Gd (GDC1) and 9.5 cat.% Gd (GDC10) deposited at 300 °C in 100 % Ar atmosphere.

3.2.1 Evaluation of Ce^{3+} concentration

The following section is adapted from [79].

To correlate the changes of surface potentials with changes in surface termination and Ce oxidation state, the stoichiometry of the samples has to be taken into account. The easiest approach would be to correlate the concentration of oxygen ($c(O)$) with the surface

potentials. This was not possible since no significant trend with oxygen content could be detected (cf. Fig. 3.2).

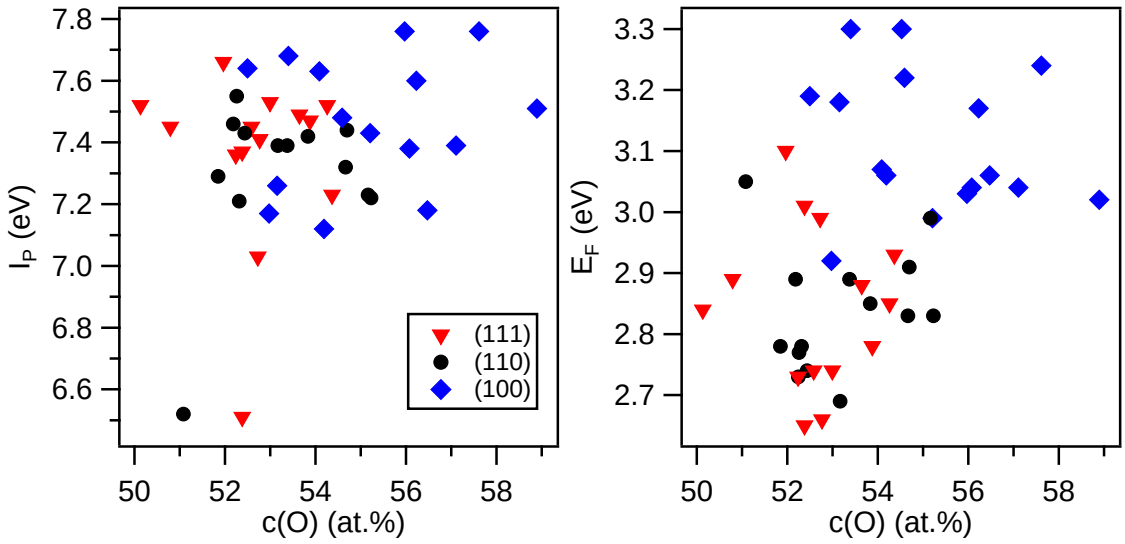

Fig. 3.2: Ionization potential and Fermi level position of differently oriented nominally undoped CeO_2 films in dependence of oxygen concentration.

For this reason the oxidation state of cerium was analyzed to obtain information about the chemical state of the surface of the films. The Ce^{3+} cation (cat.) concentration $c(Ce^{3+})$ ($c(Ce^{3+}) = [Ce^{3+}]/([Ce^{3+}]+[Ce^{4+}])$ can be evaluated by fitting the Ce3d spectra. For pure CeO_2 and Ce_2O_3, three and two different final states, respectively, are expected to be present in the Ce3d spectrum. Taking into account doublet splitting, this results in six peaks related to Ce^{4+} and four peaks related to Ce^{3+} contributing to the Ce3d emission line [80–86]. In order to obtain a reliable quantification despite the high number of fitted peaks, the fit parameters were constrained using two multiplets for the Ce^{4+} or Ce^{3+} contributions. From these fits, the binding energy difference and intensity ratios between corresponding doublet peaks was extracted and kept constant for all further fits. The doublet splitting of corresponding $3d_{5/2}$ and $3d_{3/2}$ peaks is $\sim$ 18.5 eV, which is in good agreement with literature reports by Creaser *et al.* [87] and Burroughs *et al.* [88] where the doublet splitting was determined as 18.4 eV and 18.7 eV, respectively. The top spectrum in Fig. 3.3 corresponds to a spectrum with predominant Ce^{4+} contribution, while the bottom spectrum corresponds to a strongly reduced film that was obtained by sputtering with He ions. The latter contains an almost pure Ce^{3+} spectrum. Spectrum c) shows an example fit for a Ce^{3+} concentration of $c(Ce^{3+})$= 48 %. It should be noted that, while intensity ratios and energy differences between doublets were kept constant, the intensity ratios and binding energy differences between different final states might change for different states of reduction. This effect is pronounced for very low concentrations of Ce^{3+} or Ce^{4+}. As can be seen in the top spectrum of Fig. 3.3

for example, only two emission lines from Ce^{3+} were required to fit the spectrum while photoemission from the other Ce^{3+} final state is below the detection limit of the XPS. The photoemission from final state effects originates from hybridization between Ce4f and O2p valence band states. A change of hybridization is hence expected to affect the intensity ratios and energies of the measured final states [86, 89, 90]. Differences in oxidation state of the mixed valence state of cerium are likely influencing this hybridization and thus the binding energies and photoemission intensities between different final state peaks in the Ce3d emission lines.

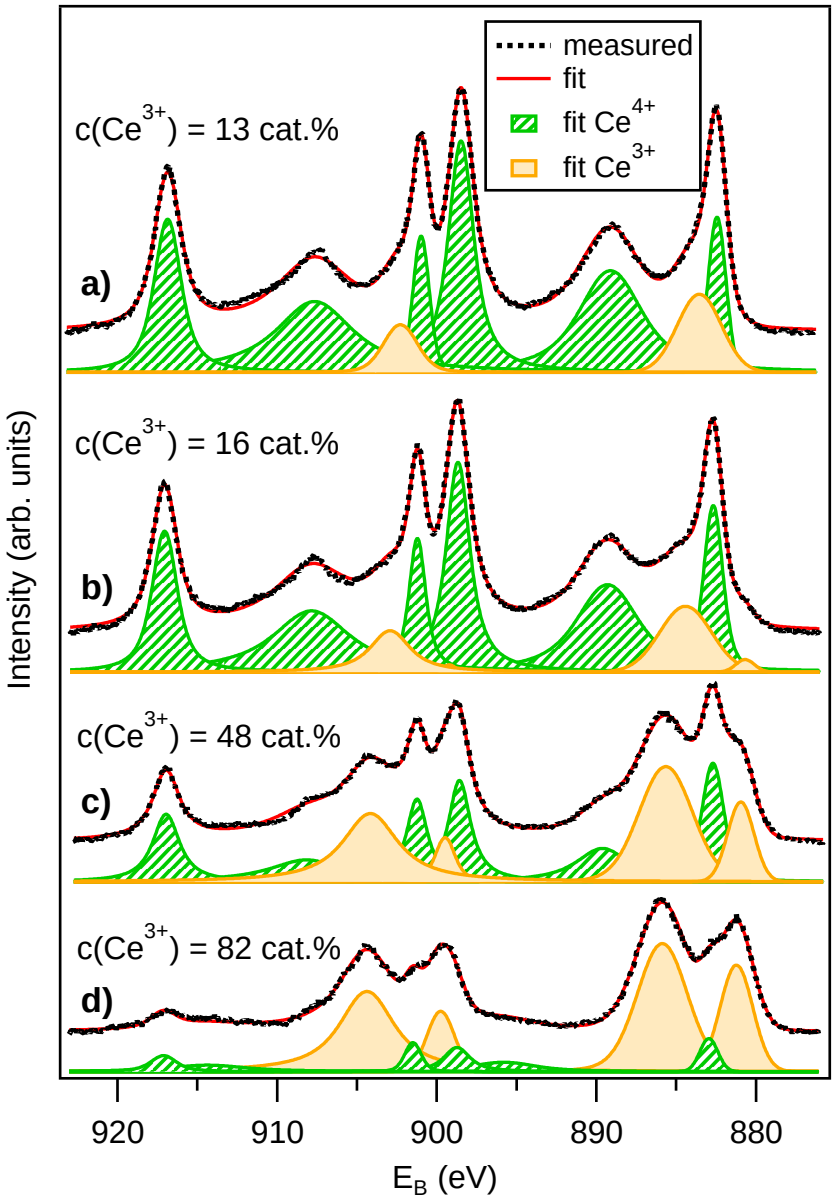

Fig. 3.3: Ce3d spectra after Shirley background correction and fit of CeO_2 films a) deposited at 500 °C in 100 % Ar, b) annealed at 400 °C in H_2O pressure of 10^{-4} to 10^{-3} Pa, c) annealed at 700 °C in vacuum and d) sputtered with He ions.

The second doublet corresponding to Ce^{3+} is typically detectable at a concentration of $c(Ce^{3+}) \approx 16$ cat.% (see spectrum b) in Fig. 3.3) or more. The uncertainty of the obtained values is estimated to be ±2 cat.%, the reproducibility is within a range of ±1 cat.%.

3.3 Van-der-Pauw electrical conductivity measurements

Conductivity measurements were carried out in van-der-Pauw geometry in a homemade setup consisting of a small quartz tube forming the furnace enabling measurement temperatures up to to 700 °C. The oxygen partial pressure in the furnace was controlled by different mixtures of argon and oxygen gas flow and the use of a commercial electrolysis cell (ZIROX SGM5EL). NDC samples (thin films and ceramics) were measured in a similar setup, but with N_2 used as inert gas instead of Ar. Measurements were performed in oxygen partial pressures (pO_2) from 10^{-6} to 10^{-1} atm. Details about the setup are described in [91]. NDC ceramic samples with $5 \times 5 \times 0.5$ mm^3 dimensions were provided by the project partners from RWTH Aachen. The samples were contacted in each corner with Pt electrodes that were deposited at room temperature with a conventional sputtercoater ("Q300T D" from Quorum).

The equilibrium conductivities at different pO_2 and temperatures were used to draw conclusions about underlying defect mechanisms in the material, while the kinetics of the conductivity change due to oxygen incorporation with increasing oxygen pressure can in principle be used to evaluate the exchange and diffusion coefficients of the sample [92]. For this, the diffusion problem can be modeled as an infinite sheet with thickness d in a constant source. While for the thin film samples the film substrate interface is blocking and oxygen is only incorporated from one side, for ceramic samples, oxygen incorporation occurs from both sides of the sample. Due to the symmetry of the problem, the general solution is the same. According to the book of Crank [93], the conductivity profiles can be described by equation 3.2.

$$\frac{\sigma - \sigma_{in}}{\sigma_{end} - \sigma_{in}} = 1 - \sum_{n=1}^{\infty} \frac{2L^2 \exp(-\beta_n^2 D_{chem} t / l^2)}{\beta_n^2 (\beta_n^2 + L^2 + L)} \tag{3.2}$$

σ is the conductivity at time t, σ_{in} and σ_{end} the initial and equilibrium conductivity, respectively, D_{chem} the chemical diffusion constant and β_n are the positive roots of

$$\beta \tan \beta = L$$

and

$$L = lk_{chem}/D_{chem}$$

with k_{chem} the chemical surface exchange coefficient. In case of thin film samples it is $d = l$, for ceramic samples $d = 2l$. D_{chem} and k_{chem} were estimated by fitting equation 3.2 to the measured conductivity profiles.
Despite this straight forward approach, the determination of exchange and diffusion coefficient from conductivity profiles proved to be challenging. While it worked well for thicker ceramic samples, it was difficult for thin films. The reason for this lies in the considerably higher resistance caused by the thin film geometry, which was close to the limit of the setup. In order to obtain reliable conductivity data, the measurement temperature had to be higher than 400 °C. On the other hand, for temperatures above 500 °C the equilibration time of the sample was in the same order of magnitude as the time for gas exchange in the oven. For comparison, thin film samples measured at 650 °C were nearly in equilibrium after 10−15 min, which is also the estimated time needed for the gas exchange in the oven. For this reason, D_{chem} and k_{chem} could only be evaluated in the temperature range from 400 to 500 °C for thin film samples. A possible solution for this could be the measurement at lower pressures, using the vacuum chamber attached to the oven. This reduces the gas exchange time significantly to about 1 − 2 min. However, the accessible pO_2 range is limited to the range 10^{-4} to 10^{-3} atm in this case. Moreover, the pressure in the oven tends to increase over time.

3.3.1 Influence of electrode material

During early measurements of GDC10 films, there was an issue that theses films could not be measured with Pt electrodes. Since it was assumed that the Pt electrodes were oxygen blocking and the mostly ionic conductivity of GDC10 could thus not be measured with Pt electrodes, In_2O_3:Sn (ITO) with a doping concentration of 10 wt.% SnO_2 was used as electronically and ionically conducting electrode. Since the measurements were working well with ITO electrodes, it was concluded, that Pt electrodes were oxygen blocking, while ITO electrodes should be conducting for both ions and electrons. In principle this should have enabled the distinction between ionic and electronic conductivity with direct current measurements, similar to the Hebb-Wagner method [94, 95], since the conductivity measured with Pt electrodes should correspond to electronic conductivity and the difference between conductivities measured with ITO and Pt electrodes should thus be the ionic contribution to the overall conductivity.
Results of measurements with different electrodes on samples from the same deposition are shown in Fig. 3.4. For UDC and NDC, a significant difference between the conduc-

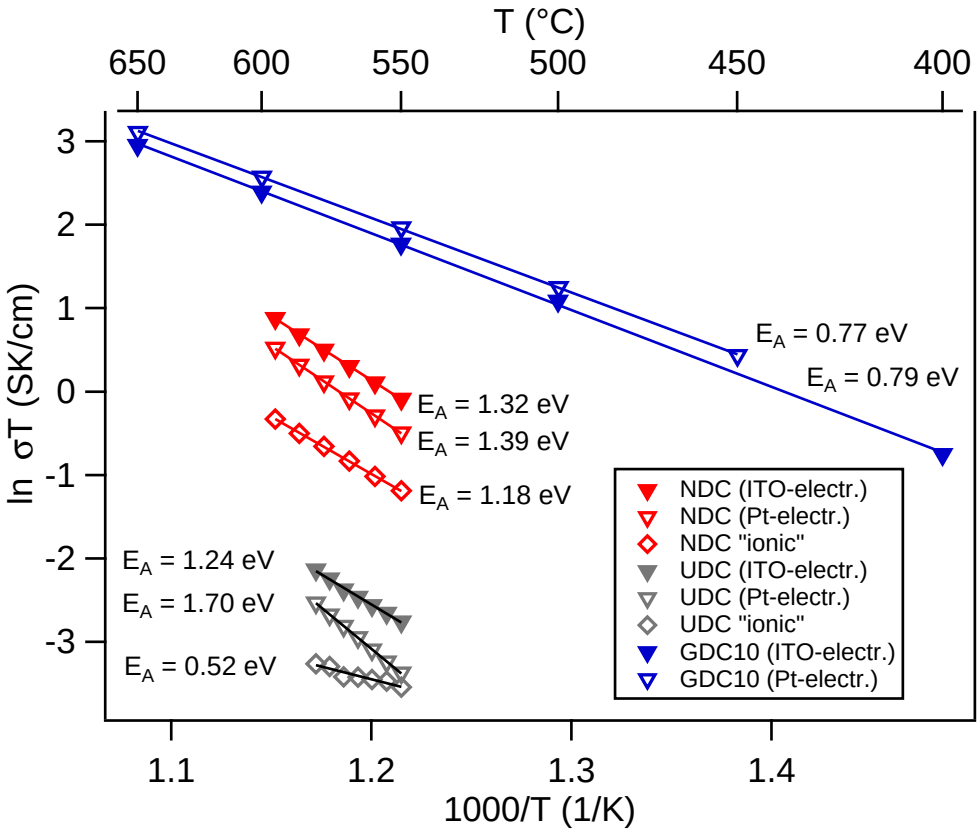

Fig. 3.4: Conductivity measured with Pt and In_2O_3:Sn (ITO) electrodes for undoped (UDC) and 1.3 cat.% Nb-doped (NDC) 9.5 cat.% Gd-doped (GDC10) CeO_2.

tivity with Pt and ITO electrodes is detected. In addition, the activation energies of the calculated ionic conductivities fit very well to expected migration enthalpies. For UDC, the oxygen migration is expected via a vacancy mechanism with an enthalpy of 0.54 eV[2], which matches the activation energy of 0.52 eV for ionic conductivity. The activation energy for the ionic conductivity of NDC is with 1.18 eV similar to the expected oxygen migration enthalpy via an interstitial mechanism (1.28 ± 0.13 eV) [96].Despite this good agreement, the overall ionic conductivity, especially for NDC, seems too high. Furthermore, newer measurements of GDC10 films were achievable even with Pt electrodes and revealed similar conductivities as the measurements with ITO electrodes. The underlying assumption, that Pt is oxygen blocking, hence turned out to be incorrect. While the electrode effect on the conductivity for UDC and NDC could still be partly related to the different oxygen permeability of the electrodes, the complete origin of this effect is still unclear.

[2] Oxygen migration enthalpies are unpublished results from molecular dynamics calculations performed by S. P. Waldow at RWTH Aachen.

3.4 Calculation of defect concentrations

In CeO_2 oxygen vacancies from the thermal reduction reaction (Eq. 3.3) are considered as intrinsic donors [19–21], while interstitial oxygen from an Anti-Frenkel reaction (Eq. 3.4) acts as intrinsic acceptor [21–23].

$$O_O^x \rightleftharpoons V_O^{\bullet\bullet} + 2Ce_{Ce}^{'} + \frac{1}{2}O_2(g) \tag{3.3}$$

$$O_O^x \rightleftharpoons O_i^{''} + V_O^{\bullet\bullet} \tag{3.4}$$

The corresponding equilibrium constants are

$$K_{red} = \frac{[V_O^{\bullet\bullet}] \times [Ce_{Ce}^{'}]^2 \times pO_2^{1/2}}{[O_O^x]} = \exp\left(-\frac{\Delta G_{red}}{k_B T}\right) \tag{3.5}$$

and

$$K_{AF} = \frac{[O_i^{''}] \times [V_O^{\bullet\bullet}]}{[O_O^x]} = \exp\left(-\frac{\Delta G_{AF}}{k_B T}\right) \tag{3.6}$$

The Gibb's free energies $\Delta G = \Delta H - T\Delta S$ is obtained using $\Delta H_{red} = 4.67$ eV [19], $\Delta S_{red} = 17.5\ k_B$ [22, 23], $\Delta H_{AF} = 4.14$ eV [21–23] and $\Delta S_{AF} = 10\ k_B$ [23]. The Frenkel defect reaction can be neglected for ceria due to the significantly higher formation enthalpy of $\Delta H_F = 7.36$ eV [97].

In order to increase ionic conductivity in ceria, the oxygen vacancy concentration is usually increased by doping with a trivalent acceptor (A) [9, 98, 99]. For example, Gd-doping in CeO_2 is expected to be mostly compensated by oxygen vacancies [20, 24, 25]:

$$Gd_2O_3 \rightleftharpoons 2Gd_{Ce}^{'} + 3O_O^x + V_O^{\bullet\bullet} \tag{3.7}$$

CeO_2 can be donor-doped (D) with pentavalent atoms to enhance the electronic conductivity [26–28]. In this case, the donors are mostly compensated by polarons (see Eq. 3.8). However at higher oxygen pressures, donor compensation by oxygen interstitials has to be taken into account as well.

$$Nb_2O_5 \rightleftharpoons 2Nb_{Ce}^{\bullet} + 5O_O^x + 2Ce_{Ce}^{'} \tag{3.8}$$

Assuming that all extrinsic dopants are always singly-charged, the charge neutrality condition is given by

$$2 \times c(\mathrm{V_O^{\bullet\bullet}}) + c(\mathrm{D^{\bullet}}) + p = 2 \times c(\mathrm{O_i^{''}}) + c(\mathrm{A^{'}}) + n \tag{3.9}$$

where c is the concentration of the defect and p and $n = c(\mathrm{Ce_{Ce}^{'}})$ are the hole and electron polaron concentration, respectively. With the mass action law for thermal carrier generation in a semiconductor

$$n \times p = N_C N_V \exp\left(-\frac{E_G}{k_\mathrm{B} T}\right) \tag{3.10}$$

where N_C and N_V are the effective density of states of the valence and conduction band, respectively, and $E_g = 3$ eV [32–34] is the O2p-Ce4f band gap of CeO_2, the defect and charge carrier concentrations can be calculated together with equations 3.5, 3.6 and 3.9. Since the underlying transport mechanism is small polaron hopping [35], N_C is equal to the density of Ce atoms in the material with $N_C = 2.55 \times 10^{22}$ cm^{-3}, as obtained from the density and molar mass of cerium dioxide. N_V was calculated, assuming an effective mass of $m_h^* = m_e$ for holes, according to [100]

$$N_V = 2\left(\frac{2\pi m_h^* k_\mathrm{B} T}{h^2}\right)^{3/2} \tag{3.11}$$

In addition, the Fermi level position in reference to the valence band maximum was calculated from the carrier concentration for the respective equilibration temperature. In order to compare the calculated Fermi level position with measured data from room temperature XPS measurements, a “quenched” Fermi level ($\mathrm{E_{F,qu}}$) was calculated by fixing the high temperature equilibrium ionic defect concentrations and only allowing for adjusting electronic carrier concentrations of this non-equilibrium state at room temperature. Since the samples were cooled with a rate of approximately 10 K/min it is reasonable to assume that the samples were not in their room temperature defect equilibrium state but closer to their high temperature ionic defect concentrations during the XPS measurements.

This method only works well assuming that all dopants are always charged since it does not include charge transition levels (CTL) of dopants. The CTL defines weather a dopant in a semiconductor is charged or neutral depending on the Fermi level position. For example, for an acceptor-doped semiconductor, if $\mathrm{E_F}$ is located above the CTL of the acceptor, the acceptor is charged. If the Fermi level is below the CTL of the acceptor, it is

neutral. By using a more physical approach to the defect calculation, the charge transition levels can be considered. For this, the formation enthalpies for an oxygen vacancy and interstitial, the electron (polaron) and hole concentrations and the concentrations of charged dopants are expressed as a function of the Fermi level position. For a given chemical potential of oxygen, i.e. temperature and oxygen pressure, the charge neutrality condition (see Eq. 3.9) is only fulfilled for a specific Fermi level position, which in turn defines all defect concentrations. This model has been implemented in IGOR Pro software (Wavemetrics) by Andreas Klein.

Fig. 3.5 shows exemplary calculated defect calculations for undoped, Nb- and Gd-doped CeO_2 at 600 °C. For undoped ceria, the reduction reaction is dominant, causing the electron concentration to be determined by the number of thermal oxygen vacancies. In contrast to this, the oxygen vacancy concentration is mostly constant with oxygen pressure for GDC1 and GDC10 since the vacancy concentration is determined by the acceptor concentration. The electron concentration for GDC is much lower than for undoped CeO_2 due to a steeper slope of the pO_2 dependence. Analogous to this, the electron hole concentration is higher in GDC and even excels the electron concentration at high oxygen pressures. The electron concentration in NDC is constant except for high pO_2, because the electron concentration is defined by the donor concentration. While the oxygen interstitial concentration can mostly be neglected for undoped ceria and GDC, it plays an important role in NDC. At high oxygen pressures, the interstitial concentration is in the order of the electron concentration and causes a decrease of n. On the other hand, the oxygen vacancy concentration is significantly lower in NDC compared to UDC or GDC as a consequence of the donor-doping.

Electronic conductivities (σ_e) were calculated with mobility data from Tuller and Nowick [35] assuming a small polaron hopping transport with an activation energy of $E_a = 0.4$ eV (see Eq. 3.12).

$$\sigma_e = ne\,\frac{B}{T}\exp\left(\frac{-E_a}{k_B T}\right) \tag{3.12}$$

with

$$B = 3.94 \times 10^2\ \frac{\mathrm{K\ cm^2}}{\mathrm{V\ s}} \tag{3.13}$$

For GDC samples, the ionic conductivities (σ_i) are dominant. They were calculated assuming a vacancy transport mechanism with the Nernst-Einstein relation:

$$\sigma_i = \frac{c_V q_i^2}{k_B T} D_V \tag{3.14}$$

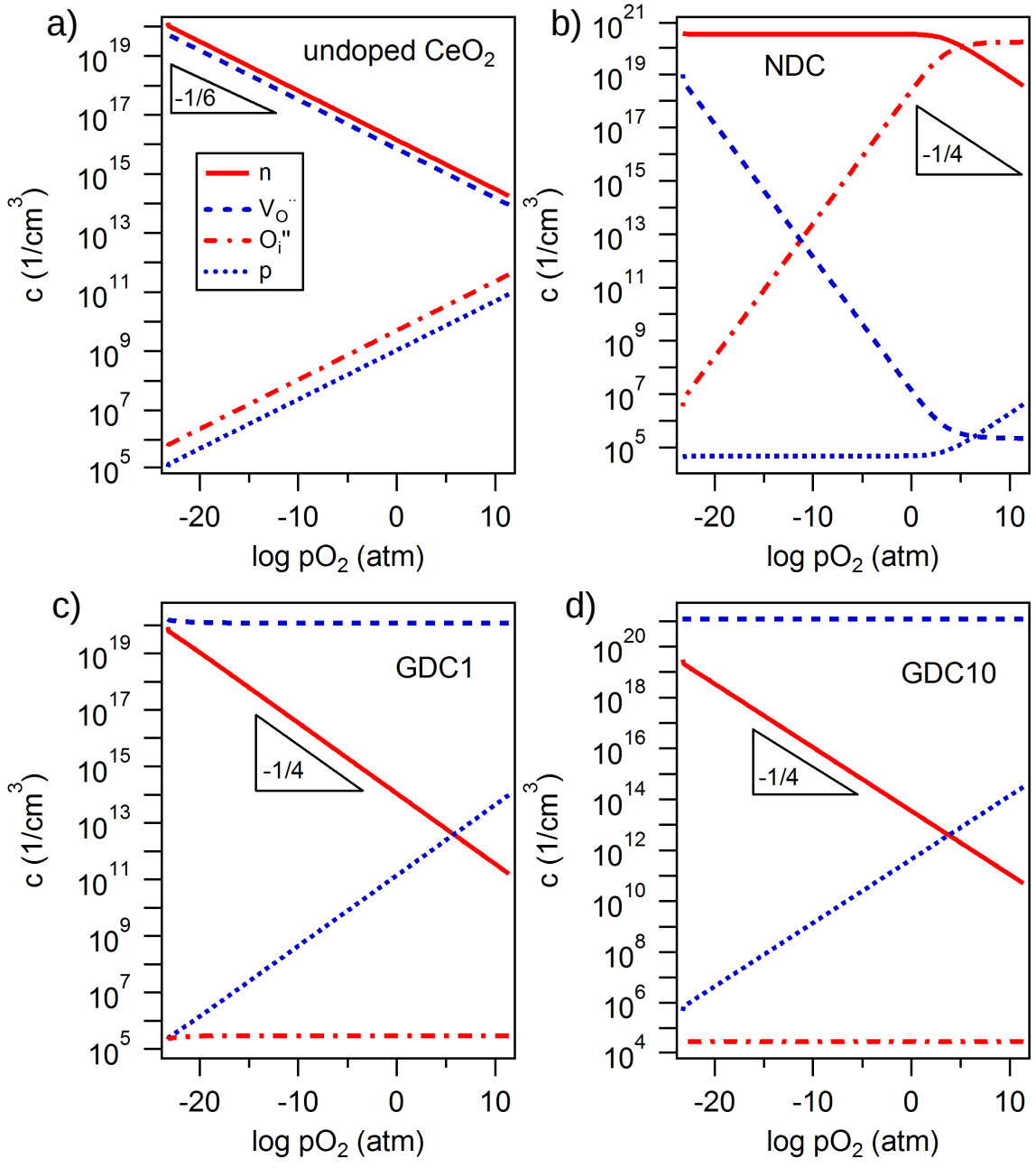

Fig. 3.5: Calculated defect concentrations for a) undoped, b) 1.3 cat.% Nb-doped (NDC) CeO_2 and ceria doped with c) 0.95 cat.% Gd (GDC1) and d) 9.5 cat.% Gd (GDC10) at 600 °C as a function of oxygen partial pressure.

c_V and q_i are the oxygen vacancy concentration and the corresponding charge of the carrier, here $q_i = 2e$. The diffusion coefficient for the oxygen vacancy transport (D_V) can be calculated with Eq. 3.15 [65].

$$D_V = \frac{Z_V}{6}(1 - n_V) d_V^2 \nu_0 \exp\left(\frac{\Delta S_{mig}}{k_B}\right) \exp\left(\frac{-\Delta H_{mig}}{k_B T}\right) \tag{3.15}$$

Z_V	:	number of neighboring atoms around vacancy	$\equiv 6$
$1 - n_V$	:	probability that sites are occupied	$\equiv 1 - (c_V / 5.1 \times 10^{22}\ \mathrm{cm}^{-3})$
d_V	:	jump distance	$\equiv a/2 = 2.705$ Å [29]
ν_0	:	jump frequency	$\equiv 10^{13}$ Hz [65]
ΔS_{mig}	:	migration entropy	$\equiv 2.2\ k_B$ [65]
ΔH_{mig}	:	migration enthalpy	$\equiv 0.92$ eV [65]

4 Structural characterization by X-ray diffraction and X-ray reflection

In order to investigate the influence of crystal orientation on surface potentials, strongly oriented CeO_2 films had to be prepared. To determine the crystal orientation of the films X-ray diffraction (XRD) measurements were conducted on a SmartLab X-ray diffractometer (Rigaku) in parallel beam geometry. All XRD measurements were carried out with Cu-Kα radiation monochromated by a Ge-(220)×2 channel cut monochromator on the primary side. On the secondary side, a 5 mm Soller slit was used for beam collimation. Parts of this chapter were published in similar form in [79].

Fig. 4.1 shows exemplary $\theta - 2\theta$ patterns for CeO_2 films deposited at 500 °C on Al_2O_3(0001)/Pt(111), MgO(110)/Pt(110) and $SrTiO_3$:Nb(100) substrates. The attribution of the reflections were done by comparison to powder diffraction files 00-004-0593 (CeO_2), 00-004-0802 (Pt), 00-046-1212 (Al_2O_3), 00-004-0829 (MgO) and 00-005-0634 ($SrTiO_3$). It can be seen that (111), (110) and (100) oriented ceria films were grown on Pt(111), Pt(110) and $SrTiO_3$:Nb(100), respectively. Only reflections corresponding to the desired orientations of CeO_2 and the underlying substrates are observed. It is noted, that films deposited with pure Ar and the O_2/Ar mixture at temperatures from 300 to 600 °C showed no significant difference in the corresponding $\theta - 2\theta$ scans.

Fig. 4.2 shows rocking curve measurements and ϕ scans of the differently oriented films. The ϕ scans proof an epitaxial relation between film and substrate. The full width at half maximum (FWHM) obtained from the rocking curve measurements, however, range from 0.5 to 1.0° indicating high mosaicity of the films.

The ϕ scan of the (220) reflections of Pt and CeO_2 of the (111) oriented film shows six peaks from $\phi = 0$ to 360°. For a single domain film only three reflections should be visible since only three corresponding crystal planes are accessible under the given measurement conditions. The Pt film hence grows in two domains rotated by 60° to each other while the CeO_2 film adopts the orientation of the Pt substrate layer. The oriented growth of CeO_2(111) on Pt(111) is in good agreement with literature. Luches *et al.* reported the growth of ultrathin CeO_2(111) films on Pt(111). They suggested a coincidence lattice, in which three unit cells of ceria grow over four Pt unit cells [81, 82].

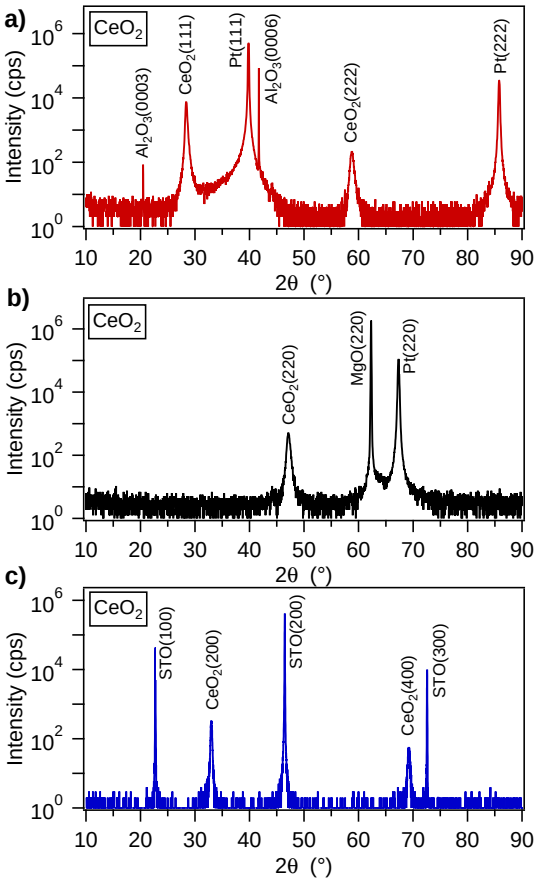

Fig. 4.1: $\theta - 2\theta$ XRD scans of undoped CeO_2 (UDC) films deposited at 500 °C on a) Al_2O_3(0001)/Pt(111), b) MgO(110)/Pt(110) and c) $SrTiO_3$:Nb(100).

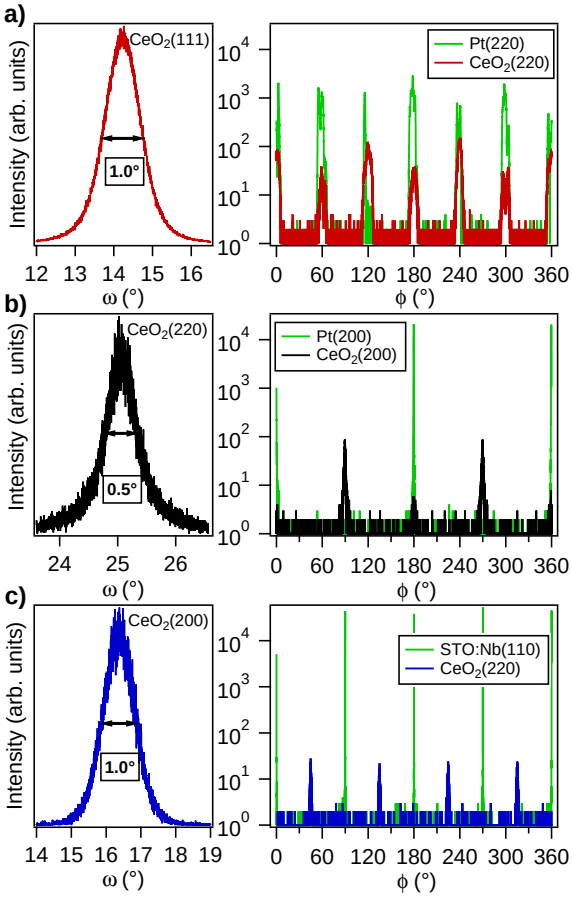

Fig. 4.2: Rocking curve and ϕ scans of CeO_2 films deposited at 500 °C on a) Al_2O_3(0001)/Pt(111), b) MgO(110)/Pt(110) and c) $SrTiO_3$:Nb(100).

The (110) oriented ceria film was grown on a single domain Pt(110) film as can be seen from the ϕ scan of the (200) reflections. The CeO_2 layer grows preferentially in one domain, however, a second domain can be seen that likely corresponds to a Pt[004]||CeO_2[003] orientation similar to the (111) oriented film. The main peaks of CeO_2(200) in the ϕ scan are shifted by 90° with respect to the Pt(200) reflections. This suggests a Pt[110]||CeO_2[001] orientation of the film. Due to the expected smaller lattice mismatch for this growth mode compared to the growth of three CeO_2 cells over four Pt cells, Pt[110]||CeO_2[001] is likely the preferred orientation for the growth of CeO_2(110) on Pt(110).

The ϕ scan of the (220) and (110) reflection of the (100) oriented ceria film and the STO:Nb substrate, respectively, shows a single domain growth of CeO_2 with the ceria cell rotated by 45° from the STO:Nb cell. An epitaxial relationship of CeO_2(100)||$SrTiO_3$:Nb(100) and CeO_2[001]||$SrTiO_3$:Nb[011] has also been reported

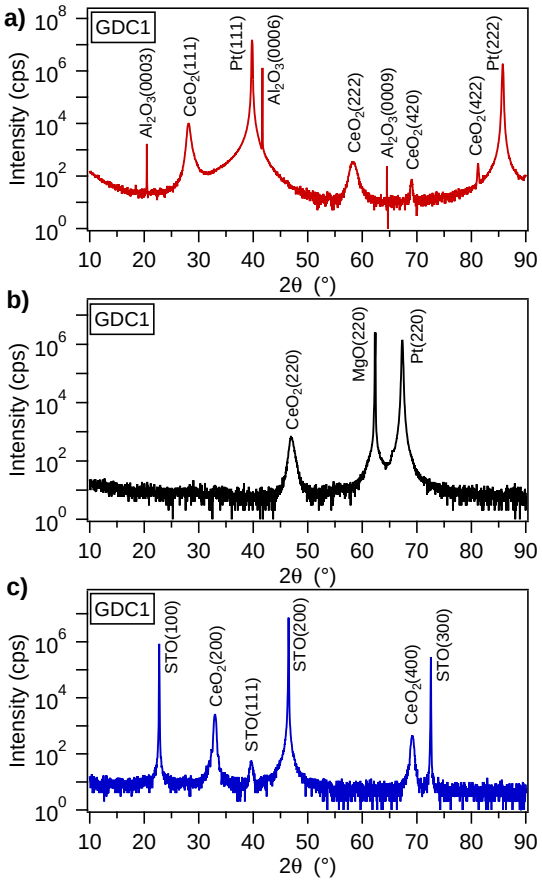

Fig. 4.3: $\theta - 2\theta$ XRD scans of 0.95 cat.% Gd-doped CeO_2 (GDC1) films deposited at 500 °C on a) Al_2O_3(0001)/Pt(111), b) MgO(110)/Pt(110) and c) $SrTiO_3$:Nb(100).

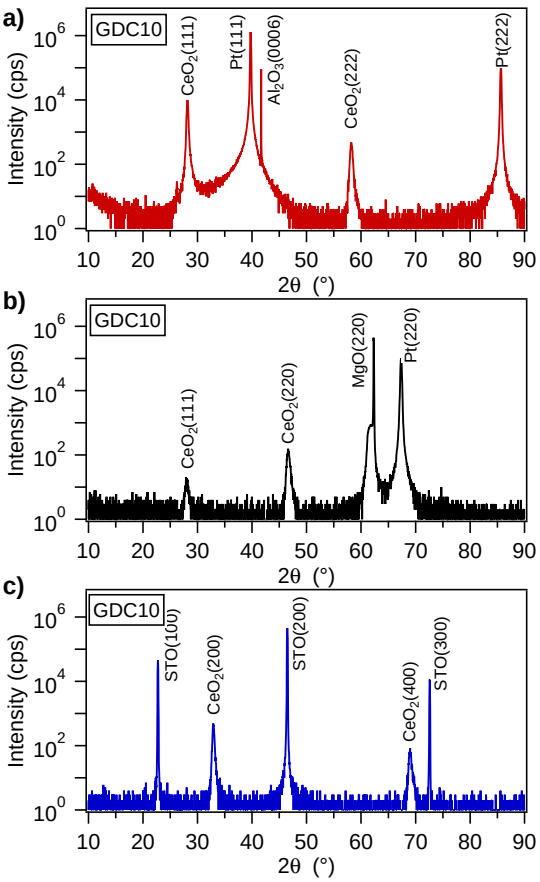

Fig. 4.4: $\theta - 2\theta$ XRD scans of 9.5 cat.% Gd-doped CeO_2 (GDC10) films deposited at 500 °C on a) Al_2O_3(0001)/Pt(111), b) MgO(110)/Pt(110) and c) $SrTiO_3$:Nb(100).

in literature [83, 84, 101]. Besides the small lattice mismatch of approximately 2 %, a good overlap of the oxygen sublattices of $SrTiO_3$ and CeO_2 is expected to promote this growth mode.

$\theta - 2\theta$ scans of GDC1, GDC10 and NDC films are shown in Figs. 4.3, 4.4 and 4.5, respectively. All films show the desired orientation as already shown for the undoped films. However, reflections from other crystal planes than the desired orientation can be seen for some samples (see Figs. 4.3a, 4.4b and 4.5b) indicating that the films are partly polycrystalline. In the diffractogram of (100) oriented NDC and GDC1 (see Figs. 4.3c and 4.5c) an additional reflection occurs that can be attributed to the (111) reflection of the $SrTiO_3$:Nb substrate. This is not expected for a single crystal substrate, but since it does not affect the film orientation, it will not be discussed further here.

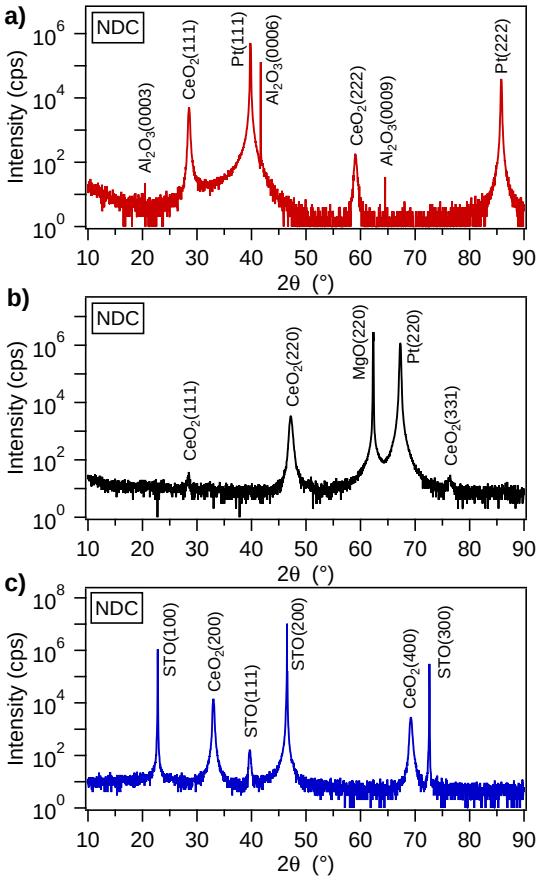

Fig. 4.5: $\theta - 2\theta$ XRD scans of differently oriented 1.3 cat.% Nb-doped CeO_2 (NDC) films deposited at 500 °C on a) Al_2O_3(0001)/Pt(111), b) MgO(110)/Pt(110) and c) $SrTiO_3$:Nb(100).

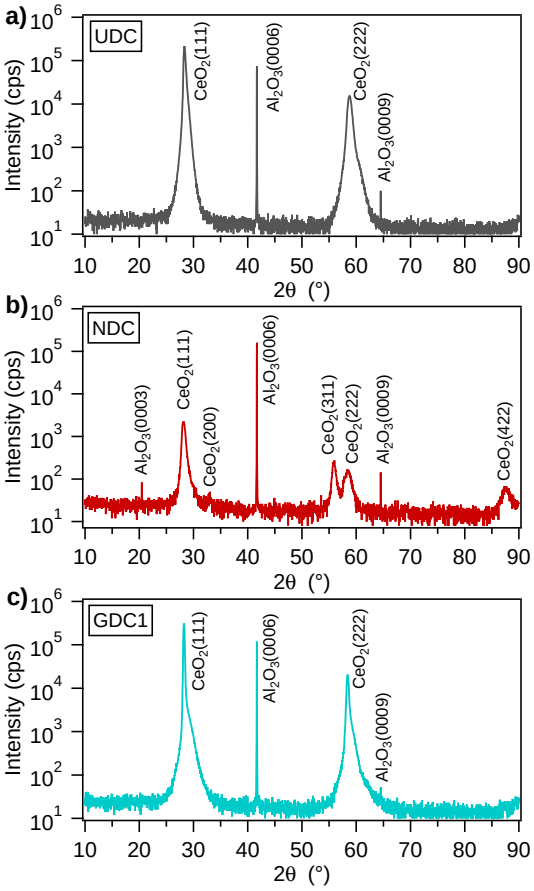

Fig. 4.6: $\theta - 2\theta$ XRD scans of differently doped CeO_2 films deposited at 550 °C on Al_2O_3(0001). a) undoped (UDC), b) 1.3 cat.% Nb-doped (NDC) and c) 0.95 cat.% Gd-doped (GDC1).

For the conductivity measurements, films were directly deposited on Al_2O_3(0001) substrates. From literature, epitaxial growth of CeO_2 on c-cut sapphire is expected [69, 102]. The results for UDC and GDC1 are in good agreement with these reports as can be seen in Fig. 4.6. Only sharp (111) and (222) film reflections occur in the $\theta - 2\theta$ diffractogram, which indicates that the films are at least strongly oriented in [111] direction or even epitaxial. Besides this, an asymmetric broadening of the reflections can be seen, which could originate from inhomogeneous strain within the films, i.e. a relaxation of the films with increasing film thickness. In contrast to this, the NDC film on sapphire is polycrystalline as evident from the additional reflections from differently oriented crystal planes in the diffractogram. Furthermore, the intensity is significantly lower despite a similar film thickness. However, the NDC film still exhibits a preferred (111) orientation.

While the thicknesses of the films were obtained by profilometry for thicker films, the error for small film thicknesses below 100 nm becomes too large when measured with profilometry. For this reason, thin films below 100 nm thickness were measured with X-ray reflectivity (XRR), which is an accurate method for determining film thicknesses in this range. In addition, the surface roughness of the samples can be estimated by XRR. The measured reflectograms were fitted using the software GenX [74] with a layer model assuming specular reflectivity. From the fit, the film thickness and the root-mean-square (RMS) roughness of the surface can be obtained.
In Fig. 4.7 exemplary XRR curves and fits for (111), (110) and (100) oriented CeO_2 films on Al_2O_3(0001)/Pt(111), MgO(110)/Pt(110) and $SrTiO_3$:Nb(100) substrates, respectively, are shown. The obtained RMS roughnesses of (111) and (110) oriented films typically lie between 0.7 and 1.5 nm with the roughness of the (110) surfaces being slightly higher compared to (111) surfaces. The surface roughnesses of (100) oriented films are below 0.5 nm. The obtained roughnesses agree well with roughnesses obtained from exemplary atomic force microscopy (AFM) measurements. Some reflectograms of (110) oriented films showed no oscillations and were thus not further evaluated. The absence of the reflections is likely related to a higher surface roughness. RMS roughnesses up to 4 nm were measured with AFM for some (110) oriented films, which would explain why no oscillations occur in the XRR measurements.
Example AFM images (see Fig. 4.8) show flat surfaces for (100) oriented films on $SrTiO_3$:Nb(100). For (111) oriented films on Al_2O_3(0001)/Pt(111), grain growth is observed at higher temperatures, while the RMS roughness is not significantly affected. Comparing the AFM images of (110) oriented films, deposited on MgO(110)/Pt(110) at 500 °C and post-deposition annealed at 700 °C, shows a significant increase in surface roughness. In addition, a pronounced linear peak and valley morphology occurs, which fits well to the expected surface faceting for (110) surfaces described in section 2.2. Since the higher surface roughness was only observed for films that were deposited or annealed at temperature above 500 °C it is likely, that the surface of films that were deposited at lower temperatures were not properly reconstructed.

In conclusion, (111), (110) and (100) oriented films of doped and undoped ceria were deposited. All films have a low surface roughness and show at least a strong preferred orientation in the distinct direction with the majority of films being epitaxial. Therefore, the deposited films are suitable for an orientation dependent investigation of the surface properties with photoelectron spectroscopy.

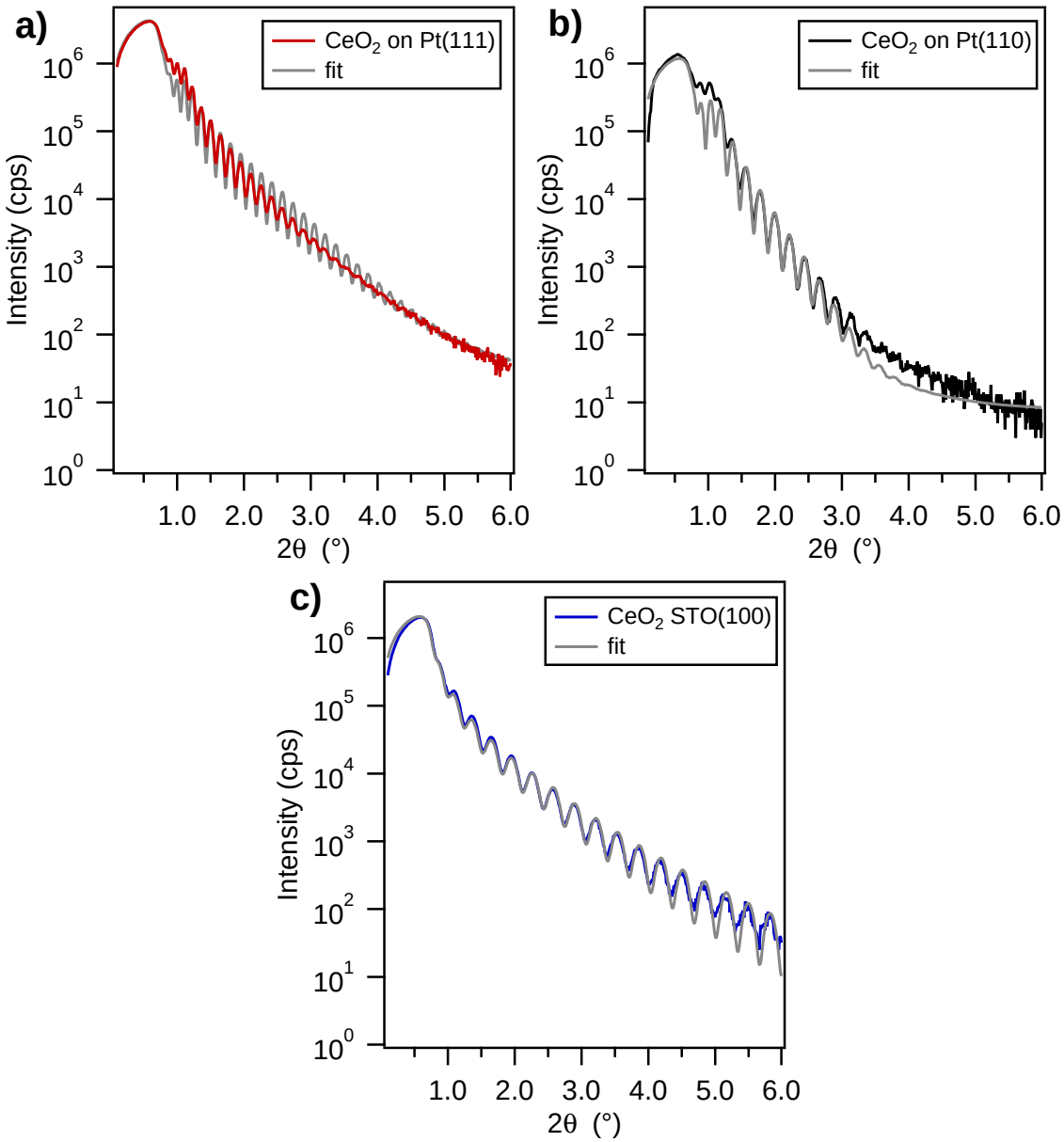

Fig. 4.7: XRR scans and fits of CeO_2 films on a) Al_2O_3(0001)/Pt(111), b) MgO(110)/Pt(110) and c) $SrTiO_3$:Nb(100).

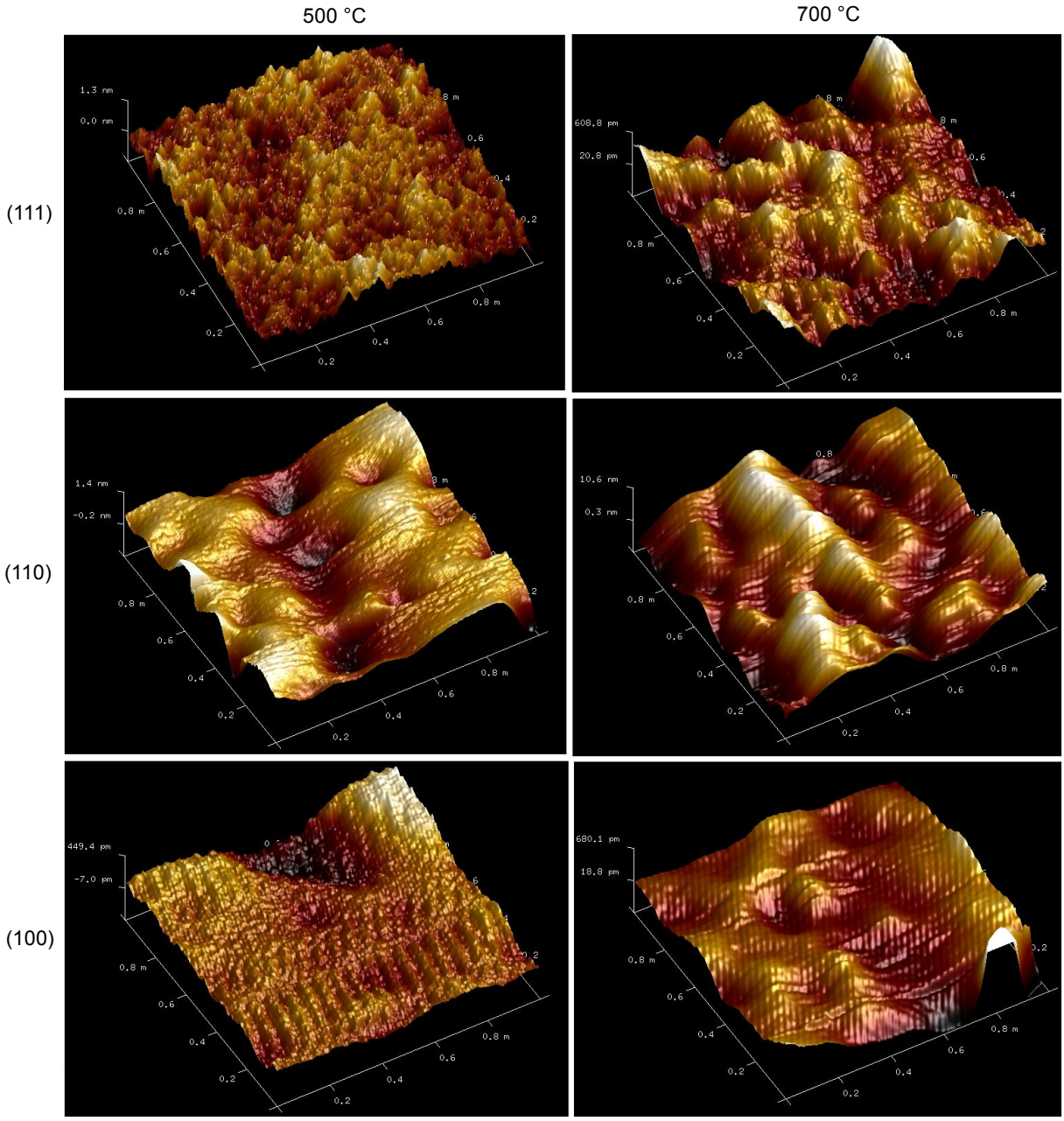

Fig. 4.8: Atomic force microscopy images of differently oriented CeO_2 films deposited on Al_2O_3(0001)/Pt(111) ([111] oriented), MgO(110)/Pt(110) ([110] oriented) and $SrTiO_3$:Nb(100) ([100] oriented). The films were deposited at 500 °C (left) or post-deposition annealed at 700 °C (right).

5 Surface potentials of CeO_2

In this chapter, the surface potentials, namely the work function, ionization potential and Fermi level positions of ceria as determined by photoelectron spectroscopy will be presented and discussed. The first section will deal with nominally undoped CeO_2 and a more general discussion about the influence of surface treatment and orientation on the surface potentials. In the second section the effects of doping on Fermi level and ionization potential will be discussed in comparison to nominally undoped ceria. Parts of this chapter were already published in similar form in [79].

5.1 Surface potentials of nominally undoped CeO_2

Example XP and UP valence band spectra of differently oriented and treated ceria films are shown in Fig. 5.1. While the spectra a) and b) in Fig. 5.1 correspond to (111) and (100) oriented films deposited on Pt(111) and $SrTiO_3$:Nb(100) substrates, respectively, at 500 °C in 100 % Ar, spectra c) and d) correspond to (100) oriented films on $SrTiO_3$:Nb(100) substrates that were annealed at 700 °C for 2 h in 0.5 Pa O_2 (oxidizing) or vacuum (reducing), respectively. The binding energies of the valence band maxima (BE_{VBM}), i.e. the Fermi level positions, were extracted from the intercept of linear extrapolation of the valence band onsets to zero intensity after background correction. The work functions (ϕ_{UPS}) were obtained from the half-maximum position of the secondary electron cut-off from the UP spectra. Due to the higher photoemission current in UPS compared to XPS, UPS measurements are more likely to be affected by charging. For this reason, the ionization potentials $I_P = BE_{VBM,UPS} + \phi_{UPS}$ from UPS, which is not affected if only small charging of the sample is present, is subtracted by $BE_{VBM,XPS}$ from XPS to obtain ϕ_{XPS}. However, no significant difference between $BE_{VBM,UPS}$ and $BE_{VBM,XPS}$ was observed for all samples indicating no noticeable charging of the films. In the following, $BE_{VBM,XPS}$ and ϕ_{XPS} will be referred to by BE_{VBM} and ϕ, respectively.
Comparing samples c) and d) in Fig. 5.1, the Fermi level position of both samples is at approximately 3 eV but an additional peak at 1.5 eV occurs in the spectrum of the film annealed under reducing conditions. This is in good agreement to previous reports and can be attributed to an occupation of Ce4f states and thus to a reduction from Ce^{4+} to Ce^{3+} [73, 80, 85]. This peak is hardly detectable in the UP spectrum due to a much lower sensitivity for f-states at the excitation energy used in UPS [103]. In contrast to the comparable valence band maxima, a significant shift of the secondary electron cut-off

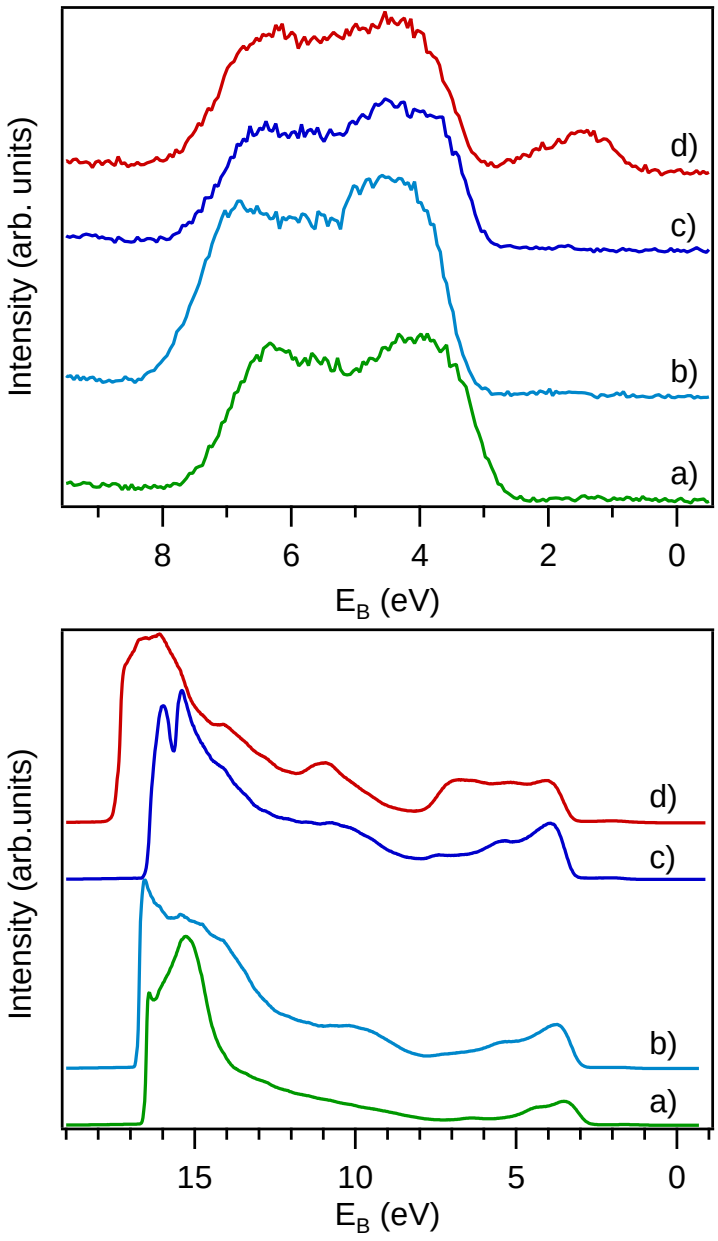

Fig. 5.1: Valence band XP spectra (top) and UP spectra (bottom) of CeO_2 films. a) (111) oriented film deposited on Pt(111) and b) (100) oriented film deposited on $SrTiO_3$:Nb(100) at 500 °C in 100 % Ar. c) and d) (100) oriented films on $SrTiO_3$:Nb(100) annealed at 700 °C for 2 h in 0.5 Pa O_2 and vacuum, respectively.

to higher binding energies can be seen for the reduced film. This shift corresponds to a reduction of work function and ionization potential by 1 eV. Furthermore, the shape of the valence band emissions has changed considerably after reduction.

Spectra a) and b) recorded from (111) and (100) oriented films, respectively, also show a difference in the valence band features, which is likely related to the different surface orientation. In addition to the different shape of the valence band emissions, spectra a) and b) in Fig. 5.1 differ in Fermi level position by 0.4 eV. This might not be expected since both samples were deposited under the same conditions. While the difference might be related to the different surface orientations of the samples, the different Fermi level positions are more likely explained by the different substrates used. Valence band spectra of (111) oriented films deposited on Pt and $SrTiO_3$:Nb(110) [1] substrates are compared in Fig. 5.2. BE_{VBM} is 0.4 eV higher for the film deposited on $SrTiO_3$:Nb(110). Since the films exhibit the same orientation and were deposited under the same conditions, it is anticipated that films grown on Nb-doped STO substrates show higher Fermi level positions. For further confirmation of this assumption, a (100) film has been grown on a $SrTiO_3/La_{0.7}Sr_{0.3}MnO_3$ substrate. This film exhibits a BE_{VBM} similar to the (111) oriented film deposited on Pt, which confirms that the higher Fermi level of the (100) oriented films on $SrTiO_3$:Nb is not a surface orientation effect.

The fact that the Fermi level is influenced by the substrate material for the given CeO_2 film thickness of > 30 nm could indicate that the net charge density in the CeO_2 is rather low ($\lesssim 10^{18}$ cm^{-3}) as the space charge layer must have an extension larger than the film thickness in order to observe such a dependence. However, this explanation is unlikely since the same effect has been observed for doped CeO_2 (NDC and GDC), where the defect concentrations are too high to fit this explanation. It is more likely, that the high Fermi level positions of (100) oriented films on $SrTiO_3$:Nb(100) are a measuring artifact, rather than intrinsic to the surface orientation. Such artifacts might be caused by non-equilibrium effects during the photoemission process. The Fermi level position at the surface is then different from that of the sample holder, which is used for referencing binding energies. A non-equilibrium situation could be caused either by charging, which is observed at other dielectric/semiconductor heterostructures even if no conventional charging is expected [104]. Alternatively, the photon source can induce significant photovoltages [105], which have particularly been reported for Nb-doped $SrTiO_3$ samples [106]. Non-equilibrium effects only influence the Fermi level positions

[1] X-ray diffraction analysis has revealed that CeO_2 films grown on (110) oriented $SrTiO_3$ single crystal substrates exhibit only (111) reflections. Epitaxial growth of CeO_2(111) on $SrTiO_3$(110) is not expected due to the dissimilar structures. However, for the argument here only surface orientation is important.

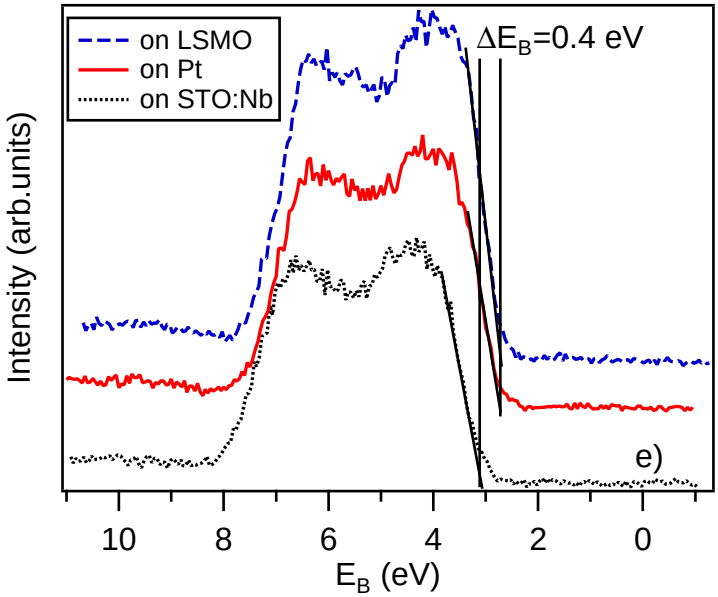

Fig. 5.2: Valence band spectra of (100) oriented CeO_2 film deposited on $La_{0.7}Sr_{0.3}MnO_3$ (LSMO) and (111) oriented CeO_2 films deposited on Pt(111) and on $SrTiO_3$:Nb(110) (e).

and work functions. The determination of the ionization potential is not affected by these phenomena.

The Fermi level positions, work functions and ionization potentials for different deposition conditions and surface orientations are summarized in Fig. 5.3. For the (111) and (110) oriented films deposited on platinum substrates the trend in surface potentials is very similar. From 300 to 600 °C only a small increase of 0.2 eV in Fermi level position is observed independent of deposition atmosphere. The more reducing conditions at higher deposition temperatures is expected to cause an increase in oxygen vacancy and thus Ce^{3+} concentration [69, 107]. This is in good agreement with the observed rise of the Fermi level. The generally higher Fermi level of (100) oriented films compared to the other surface orientations are due to the $SrTiO_3$:Nb substrate used to obtain (100) orientation as discussed above. Surprisingly, the Fermi level position is slightly ($\sim$ 100 meV) higher for films deposited on $SrTiO_3$:Nb under oxidizing conditions than for films deposited under reducing conditions. This agrees well with the occurrence of a photovoltage at the interface to the $SrTiO_3$:Nb substrate. Schafranek *et al.* reported for $SrTiO_3$:Nb/Pt interfaces an increased barrier height for oxidized samples due to a photovoltage in the $SrTiO_3$, which is not present for reduced samples [106].

The temperature of 700 °C in Fig. 5.3 does not correspond to the deposition temperature but to post-deposition annealing at 700 °C in 0.5 Pa Ar or O_2. A substrate temperature of 700 °C during the deposition resulted in a strong reduction of the growth rate to very low values and was therefore not chosen. After annealing at 700 °C in reducing

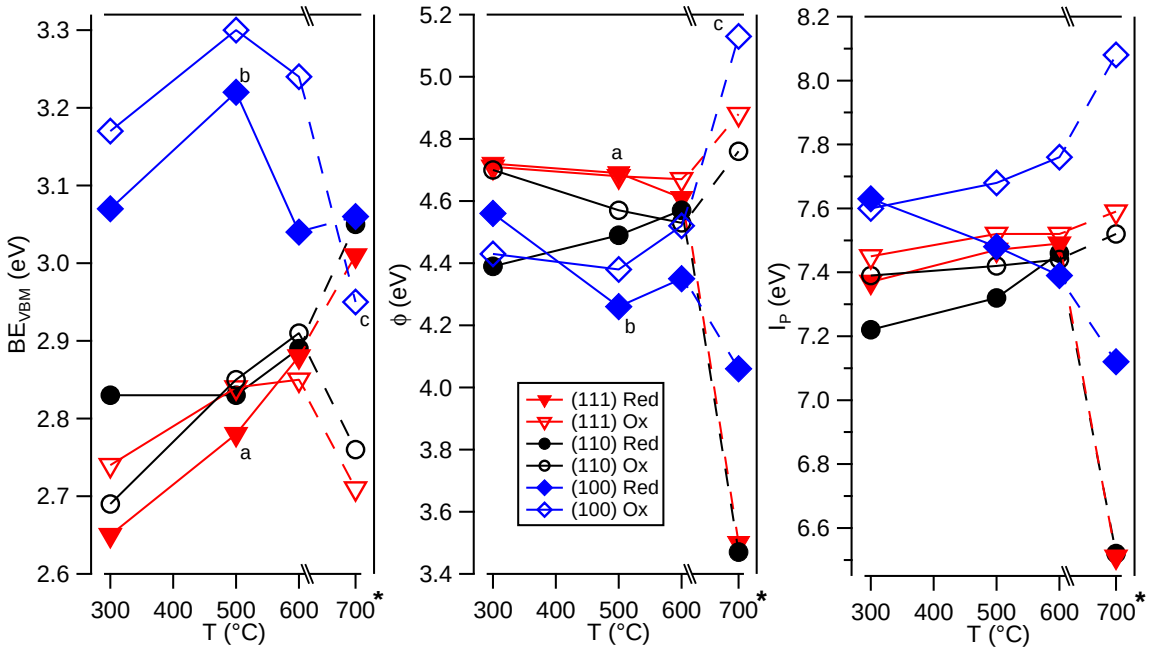

Fig. 5.3: Fermi level position, work function and ionization potential vs. deposition temperature (≤ 600 °C) of nominally undoped CeO_2. Films were either deposited in 100 % Ar (Red) or a 10 % O_2/90 % Ar mixture (Ox). Post-deposition annealing at 700 °C (*) for 2 h in 0.5 Pa Ar (Red) or 0.5 Pa O_2 (Ox) is included. Data points labeled with letters (a/b/c) correspond to spectra shown in Fig. 5.1

atmosphere, BE_{VBM} of the films is around 3 eV for all orientations. This value agrees with a reported value by Pfau and Schierbaum for similar sample conditions [80]. Heating in oxygen at 700 °C results in a decrease of BE_{VBM} as expected from a decrease of oxygen vacancies due to oxygen incorporation. Additionally, the fact, that the Fermi level of the (100) oriented films on $SrTiO_3$:Nb(100) is the same as for the other orientations for strongly reduced films, affirms the aforementioned photovoltage effect for non-reduced $SrTiO_3$:Nb as described by Schafranek *et al.* [106].

Except for the high temperature reducing treatment, no significant changes of I_P are observed for the (110) and (111) oriented films. Their ionization potential is around 7.4 eV. The insensitivity of I_P for these orientations agrees with the fact that Tasker type I (110) and type II (111) oriented surfaces are non-polar. For most oxygen activities no change of surface termination, which would modify the surface dipole contribution to the work function, is expected for such surfaces [51, 108]. The similarity of I_P for these two surface orientations may be fortuitous but would agree with the expected high area fraction of {111} nanofacets on the (110) surface [41, 48, 49] as described in section 2.2. In contrast, the ionization potential of the (100) oriented films treated under oxidizing conditions is up to 1 eV higher than that of the films treated under reducing conditions. The difference increases with deposition temperature and is highest after the 700 °C annealing treatments. Such a dependence of I_P on oxygen activity is to be expected for the polar Tasker type III (100) surface.

For annealing at 700 °C in reducing atmosphere, a strong decrease of the ionization potential is observed for all surface orientations. The reduction of I_P, which is less pronounced for the (100) oriented films, is accompanied by a significant chemical reduction of Ce^{4+} to Ce^{3+} at the surface. This will be addressed in more detail in the following.

The Fermi level positions, work functions and ionization potentials are shown in Fig. 5.4 as a function of the Ce^{3+} concentration, which was determined as described in section 3.2.1. The Fermi level positions of the (111) and (110) oriented films deposited on Pt rises steeply with increasing Ce^{3+} concentration from approximately 2.7 eV to a saturation level at $\sim$ 3 eV. The rise of the Fermi energy upon reduction of the sample is generally expected and Fermi levels of $\sim$ 3 eV are in line with literature reports [32, 34, 80].

The saturation Fermi level corresponds well with the energetic position of the unoccupied $Ce4f^0$ states, which are expected around 3 eV above the valence band maximum [32–34]. A further increase of E_F is not expected as the occupation of the Ce4f states shifts the corresponding occupied $Ce4f^1$ states down in energy [32–34, 109]. This is obvious from the appearance of the Ce4f emission in the valence band spectrum (see Fig. 5.1). As the upper limit of Fermi level position observed for the (110) and (111) oriented films can be understood in terms of the bulk electronic structure of CeO_2, it is

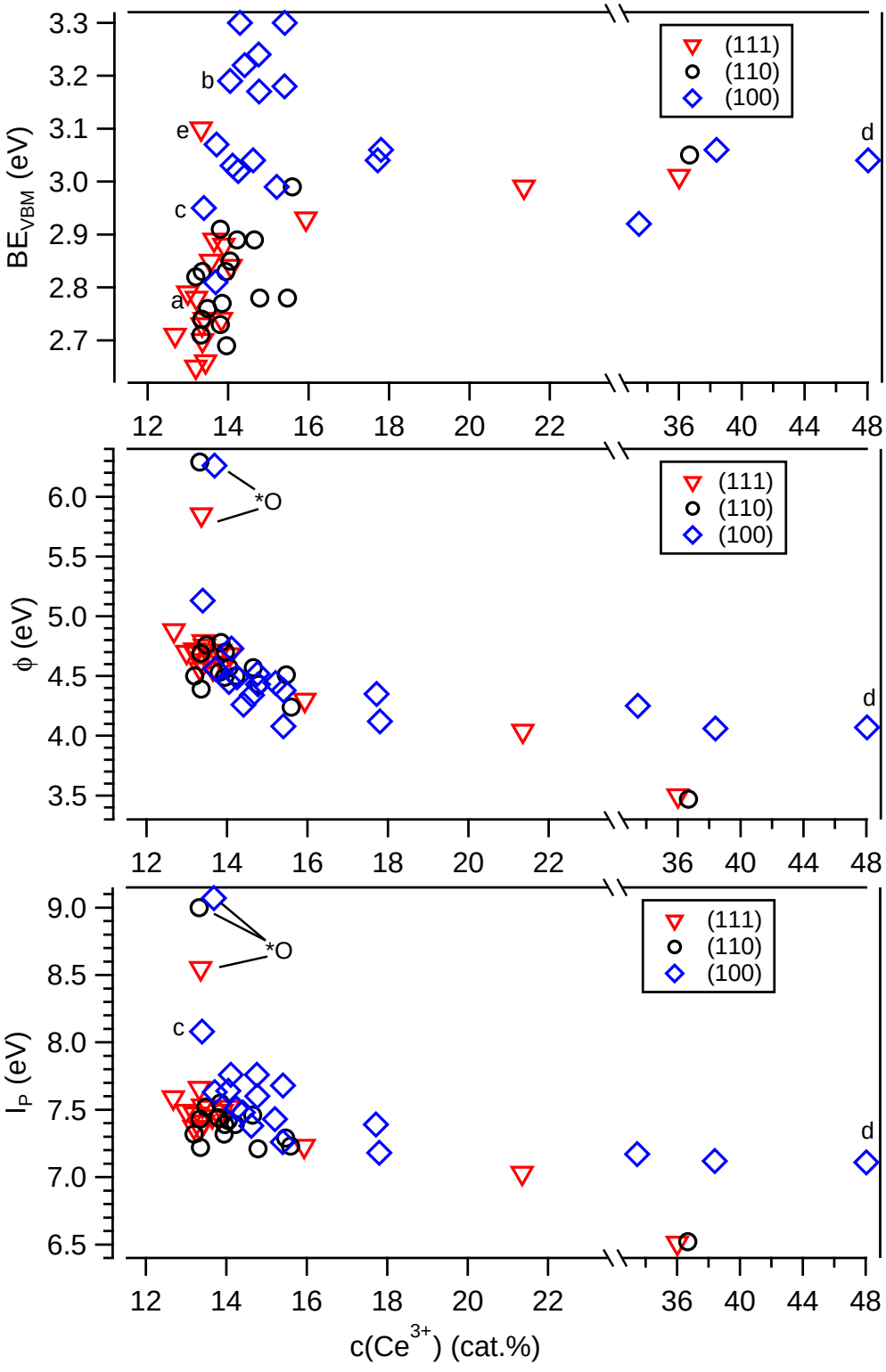

Fig. 5.4: Fermi level position, work function and ionization potential of nominally undoped CeO_2 depending on Ce^{3+} concentration. Data points labeled with letters a-e correspond to spectra shown in Figs. 5.1 and 5.2. *O refers to samples treated in oxygen plasma.

surprising that higher Fermi levels are observed at surfaces of (100) oriented films. It is even more puzzling that these high Fermi levels are observed at comparatively low Ce^{3+} concentrations and that E_F is lowered to the value of (110) and (111) oriented films for more reducing conditions. However, a high Fermi level position with a comparably low Ce^{3+} concentration is also observed for a (111) oriented film deposited on $SrTiO_3$:Nb(110) (see data point labeled e) in Fig. 5.4). It can explained thus by the aforementioned non-equilibrium effect during the photoemission process, i.e. a photovoltage that causes the surface Fermi level to differ from the actual substrate Fermi level position.

In comparison to other semiconducting oxides, where the Fermi level position has been observed to vary by more than 1 eV depending on oxygen activity [18, 110–112], the overall variation of E_F of the investigated CeO_2 films is comparatively small with only ~ 0.3 eV for the different sample orientations.
The work function and ionization potential decreases with increasing c(Ce^{3+}) for films of all orientations with a maximum difference in ϕ and I_P of more than 2 eV.
As already evident from Fig. 5.3, most films included in Fig. 5.4 exhibit ionization potentials of 7.4 ± 0.2 eV and a Ce^{3+} concentration of 14 ± 2 cat.%. Stronger reduction of the surface by heating in H_2O or vacuum increases the Ce^{3+} concentration and lowers I_P to ~ 7.2 eV for the (100) and to ~ 6.5 eV for the (110) and (111) orientations, respectively. A comparable reduction of I_P is also observed for SnO_2 surfaces, where oxidized surfaces with Sn^{4+} cations exhibit an ionization potential which is ~ 1 eV higher than that of reduced surfaces with Sn^{2+} cations [110]. In contrast to the data shown in Figs. 5.3 and 5.4, no significant influence of surface orientation is found for SnO_2 [113].
The data shown in Fig. 5.4 also include films, which were treated by an oxygen plasma. These films exhibit the highest ionization potentials of 8.6 eV for the (111), 9.0 eV for the (110) and to 9.1 eV for the (100) oriented films, respectively. Overall, the maximum variation of ionization potential amounts to 2.0 eV for the (100), 2.5 eV for the (110) and 2.1 eV for the (111) oriented films. It is remarkable that this variation is twice or more than that reported for other oxide materials [40, 52, 108, 110, 113–115]. It is unclear whether this huge dependence of ionization potential and work function on surface condition is intrinsic to the fluorite structure or particular to the surface chemistry of CeO_2. In this context it is particularly intriguing that the strong surface oxidation after oxygen plasma treatment does not result in a reduction of Ce^{3+} concentration.
The huge variation of ionization potential and work function for all surface orientations indicates a strong change of surface termination for all surface orientations. This could have been expected for the polar Tasker type III (100) surface, but not for the non-polar Tasker type I (110) and type II (111) surfaces. One possible reason might be micro-faceting as it has been suggested for In_2O_3 [52, 108]. In_2O_3 has a cubic

bixbyite structure, which is closely related to the fluorite structure of CeO_2. In addition, the surface energies (γ) of indium oxide show the same trend as for CeO_2 with $\gamma(111) < \gamma(110) < \gamma(100)$ [45, 46, 108, 109, 116]. This ordering might be reversed under strongly oxidizing conditions as it is the case for In_2O_3 [51, 52, 108]. Only then (100) facets, which could change surface termination upon oxidation and reduction, could be likely on (111) and (110) surfaces. However, a change in the ordering of surface energies is unlikely in the case of CeO_2 due to the expected much higher surface energy of the (100) surface compared to the (111) and (110) surface [45, 109, 116]. The huge variation of CeO_2 surface potentials is more likely related to the formation of different chemical surface species involving Ce^{3+}, oxygen vacancies and peroxide ions. In addition, the reconstructed surfaces of ceria should be considered since a discussion based on the Tasker types of the bulk truncated surfaces is oversimplified.

The lowest Ce^{3+} concentrations extracted from fitting the Ce3d core level spectra were around 13 cat.%. This is in good agreement with literature where a significantly higher Ce^{3+} concentration at the surface is reported even for fully oxidized films [117]. Chueh *et al.* reported Ce^{3+} concentrations at the surface that were over two orders of magnitude higher compared to bulk Ce^{3+} concentrations, with only a small dependence of the Ce^{3+} concentration at the surface on temperature and oxygen partial pressure [85].

It is nevertheless remarkable that even the oxygen plasma treated samples do not have a significantly lower Ce^{3+} concentration. The strong increase of ionization potential after oxygen plasma treatment indicates a significantly higher oxygen content at the topmost atomic planes of the surface. This should translate to a decrease of oxygen vacancy concentration. The high c(Ce^{3+}) after oxygen plasma treatment therefore could suggest that the Ce^{3+} detected by XPS is not originating from oxygen vacancies in the topmost atomic plane, but from subsurface oxygen vacancies that are apparently not annihilated by oxygen plasma treatment. This assumption is supported by theory, which shows for the (111) surface that the formation energies of subsurface oxygen vacancies is lower than that of surface vacancies [118–120]. A high concentration of subsurface vacancies was also reported from experimental studies [121, 122].

In contrast to this, there is a significant amount of reports about high oxygen vacancy concentration in the top most surface layer for all investigated surface orientations [41, 43–49, 53, 83, 85]. It is thus unlikely that the high Ce^{3+} concentration even after treatment under strongly oxidizing conditions originates solely from subsurface vacancies. Taking surface reconstruction as described in section 2.2 into account, the high Ce^{3+} concentration for oxidized samples can be understood. The (110) and (100) surface have been reported to reconstruct by removing oxygen from the top layer of the surface [41, 49, 53]. Especially for the (100) surface this oxygen deficiency of the top layer can be more than 50 %. Upon removal of surface oxygen, Ce^{4+} cations in the subsurface layer are reduced

to Ce^{3+} [53]. This means that the high surface concentration of Ce^{3+} would be a direct consequence of the surface reconstruction and thus a necessity to reduce the surface energies, which is the driving force for surface reconstruction. Even under strongly oxidizing conditions, e.g. an oxygen plasma treatment, a change in surface reconstruction might be unfavorable compared to the reoxidation of the surface. The strong increase of the ionization potential after the oxygen plasma treatment shown in Fig. 5.4 is therefore more likely related to adsorbed oxygen species, e.g. peroxide (O_2^{2-}) or superoxide (O_2^-), causing the increase in surface dipole.

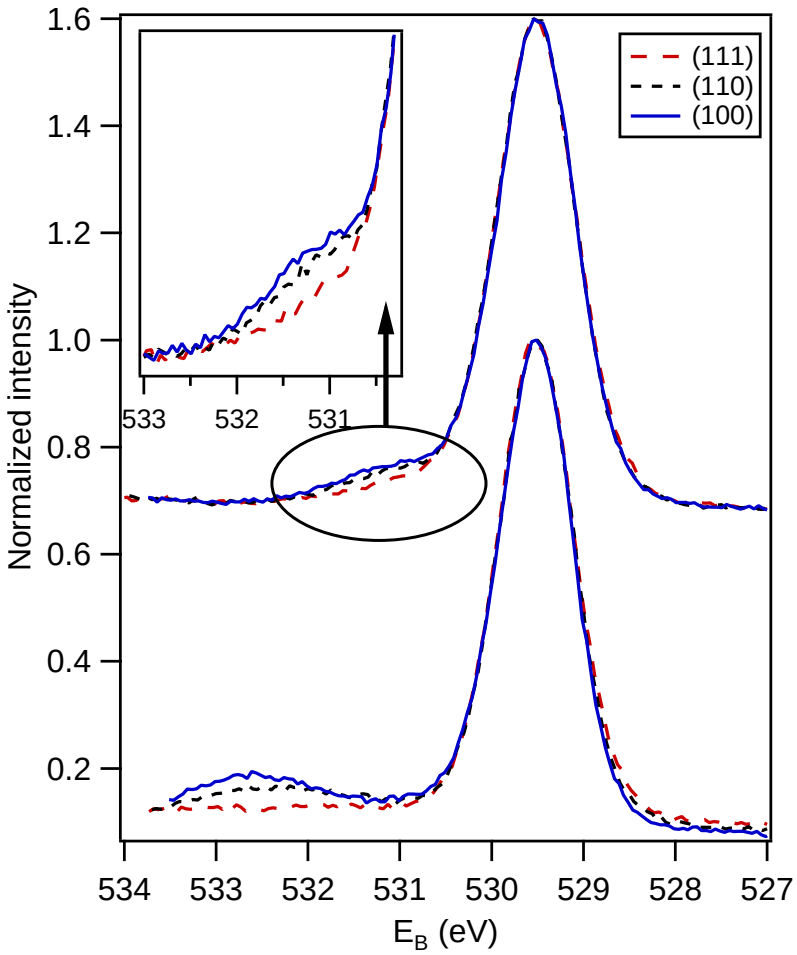

Fig. 5.5: Normalized O1s XP spectra of as deposited CeO_2 films at 300 °C in Ar (top) and CeO_2 films after oxygen plasma treatment (bottom). Main peaks of spectra are all shifted to 529.7 eV for better comparison of shoulder emissions.

In this context, it is interesting to take a closer look at O1s spectra of the films. Fig. 5.5 shows the O1s spectra of the differently oriented films as deposited at 300 °C in Ar and samples after oxygen plasma treatment. Besides the main emission line, a shoulder emission at higher binding energies can be seen in all spectra. For better comparison of the shoulder emissions, the spectra are normalized and shifted along the x-axis so

that the main peaks lie on top of each other. From this representation, it can be seen that the peak shape of the main emission lines is the same for the different orientations. For the as deposited films, a shoulder emission occurs at 1.4 eV higher binding energies relative to the main emission. While secondary peaks in the O1s lines are often reported in literature and typically assigned to oxygen species at the surface, the origin of these emission lines is still in discussion [49, 73, 80, 83, 87, 123–127]. Yang *et al.* reported shoulder emissions at 1.7 eV and 1.4 eV higher binding energies for the reconstructed and unreconstructed (110) surface and the (110) surface with {111} facets, respectively [49]. They suggest that these peaks originate from surface oxygen adjacent to oxygen vacancies. Contrary to this, the peak shifted by 1.4 eV from the main emission line is attributed to surface hydroxyl by Mullins *et al.* [83]. Since the hydroxyl on the (111) surface is less stable and desorbs at much lower temperature compared to the hydroxyl on the (100) surface, the O1s shoulder emission is less pronounced for (111) oriented compared to (100) oriented films. This effect can be seen in the O1s spectra shown in Fig. 5.5. Moreover, these shoulder peaks disappear during O plasma treatment. Thus, the shoulder emission of as deposited films are likely related to surface hydroxyl groups. After oxygen plasma treatment a peak at 2.8 eV and 3.0 eV higher binding energies occurs for the (110) and (100) oriented films, respectively, contrary to the (111) oriented sample, where this shoulder emission could not be detected after plasma treatment. This correlates with the ionization potential of the (111) oriented film, which is 0.5 eV lower after the plasma treatment compared to I_P of the (110) and (100) oriented films after the same treatment (see Fig. 5.4). In literature, a second peak in the O1s spectrum of CeO_2 shifted by $\sim$ 3 eV from the main peak has been assigned to low coordinated oxygen at the surface or grain boundaries [125], adsorption of H_2O [83] or hydroxyl species [123]. These possibilities seem to be unlikely, since this emission cannot be observed for other sample treatments, where hydroxyl or H_2O adsorption would be more likely. Therefore, an assignment of this spectral feature cannot be done with certainty but it seems likely that this shoulder emission originates from peroxide species [87, 128].

5.1.1 Comparison with calculated Fermi level positions (undoped CeO_2)

The bulk electron concentration was obtained from point defect calculations. With this the Fermi level can be calculated. Comparing the expected bulk Fermi level with the measured surface Fermi level could provide information about potential space charge layers at the surface. The calculated Fermi level positions at 300, 500, 600 and 700 °C and Fermi level positions after quenching to room temperature ($E_{F,qu}$) are shown in Fig. 5.6 in dependence of oxygen partial pressure for strongly compensated acceptor-doped CeO_2

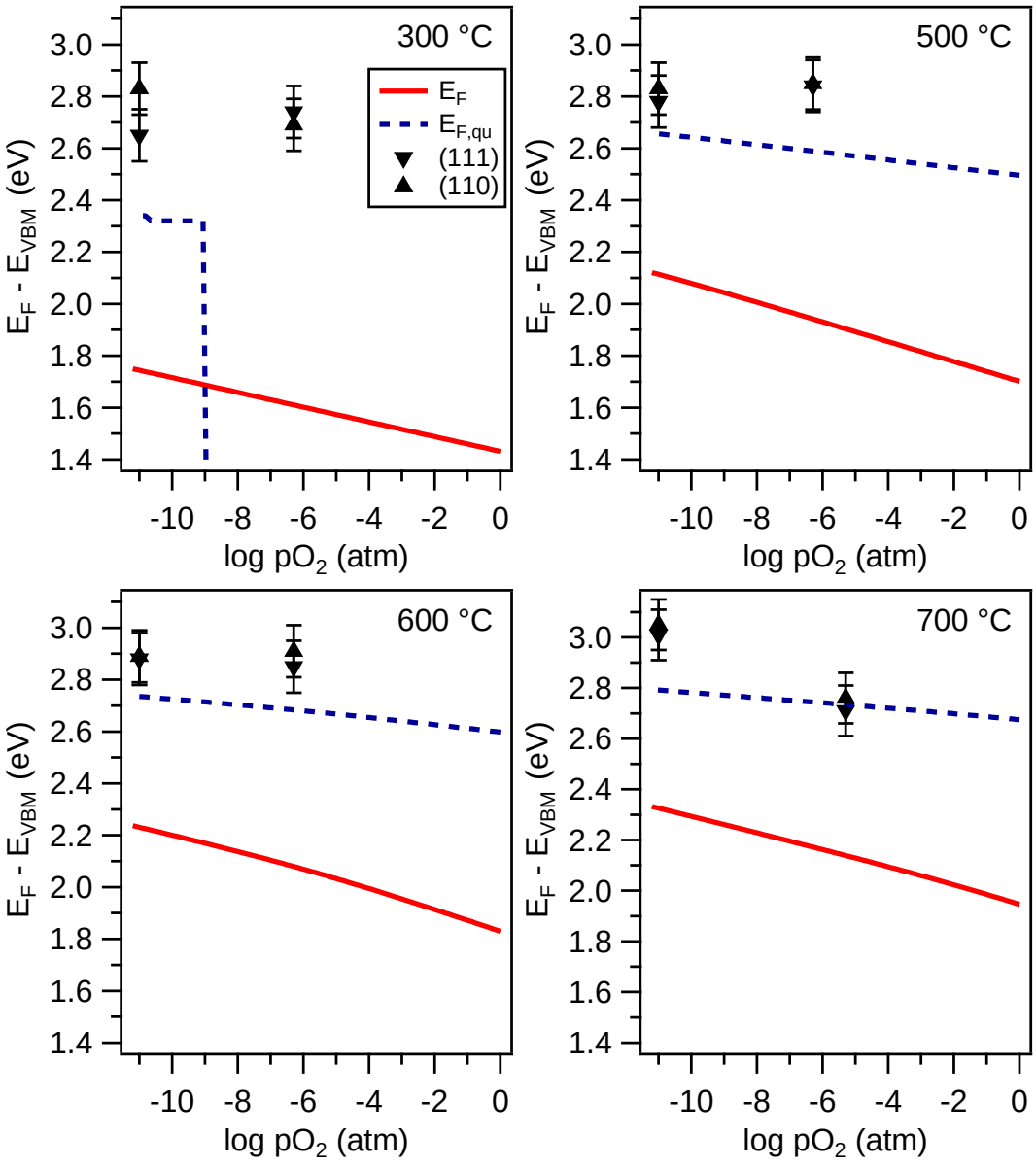

Fig. 5.6: Calculated Fermi level position at high temperatures and after quenching to room temperature for strongly compensated acceptor-doped CeO_2: A+D ($c(\mathrm{A}) = 0.005$ cat.% and $c(\mathrm{D}) = 0.0045$ cat.%) at different temperatures in comparison with experimental data.

together with experimental data from XPS. Details are given in section 3.4. For the calculation, an acceptor concentration of $c(\mathrm{A}) = 0.005$ cat.% and a donor concentration of $c(\mathrm{D}) = 0.0045$ cat.% was used. The reason why these concentrations were chosen will become evident in section 6.1.1. It should be noted that the oxygen partial pressure for the data points at $\log \mathrm{pO_2} = -11$ was estimated from the process pressure and the specified oxygen impurity of the Ar process gas (< 2 ppm), i.e. the actual $\mathrm{pO_2}$ value might be slightly more reducing. Furthermore, it should be taken into consideration that the calculated $\mathrm{E_F}$ and $\mathrm{E_{F,qu}}$ are bulk values, while the experimental data from XPS represents the surface Fermi level.

At 300 °C the measured Fermi level is $300 - 400$ meV higher than the expected $\mathrm{E_{F,qu}}$. A reason for this might be a higher defect concentration originating from the sputter process at the deposition temperature of only 300 °C. Around the sharp decrease of $\mathrm{E_{F,qu}}$ at $\log \mathrm{pO_2} \approx -9$ the material changes from n- to p-type. At lower oxygen pressures excess electrons from thermally generated oxygen vacancies cause the high Fermi level, while at higher $\mathrm{pO_2}$ the acceptors are increasingly compensated by electron holes, due to oxidation of oxygen vacancies. The sharp transition from high to low $\mathrm{E_{F,qu}}$ occurs when the hole concentration exceeds the electron concentration.

The experimental $\mathrm{E_F}$ at 700 °C is higher than $\mathrm{E_{F,qu}}$ at reducing and lower under more oxidizing conditions. The data point at $\log \mathrm{pO_2} = -11$ corresponds to a strongly reduced sample with a Ce^{3+} surface concentration of 36 cat.% and should thus be considered cautiously. The experimental $\mathrm{E_F}$ at $\log \mathrm{pO_2} = -5.3$ agrees well with $\mathrm{E_{F,qu}}$.

For temperatures ≥ 500 °C, the calculated Fermi level positions after quenching are in reasonable agreement with measured ones although the measured surface $\mathrm{E_F}$ from XPS are slightly higher than the calculated bulk Fermi level for quenched samples. Since the samples are not perfectly quenched, the measured Fermi level is expected to be between $\mathrm{E_F}$ at high temperatures and $\mathrm{E_{F,qu}}$. As can be seen in Fig. 5.6, the measured data tend to have a slightly higher $\mathrm{E_F}$ compared to $\mathrm{E_{F,qu}}$. This could be an indication for a space charge layer with an electron accumulation at the surface. The relatively small increase of surface to bulk $\mathrm{E_F}$ suggest that the space charge potential is small or the space charge layer very narrow. Space charge layers are reported for grain boundaries in ceria [129–131] and are potentially present at the surfaces as well [132]. A narrow electron accumulation layer at the surface also fits the high Ce^{3+} concentrations at the surface as discussed above.

5.2 Surface potentials of doped CeO_2

5.2.1 Ionization potentials of doped CeO_2

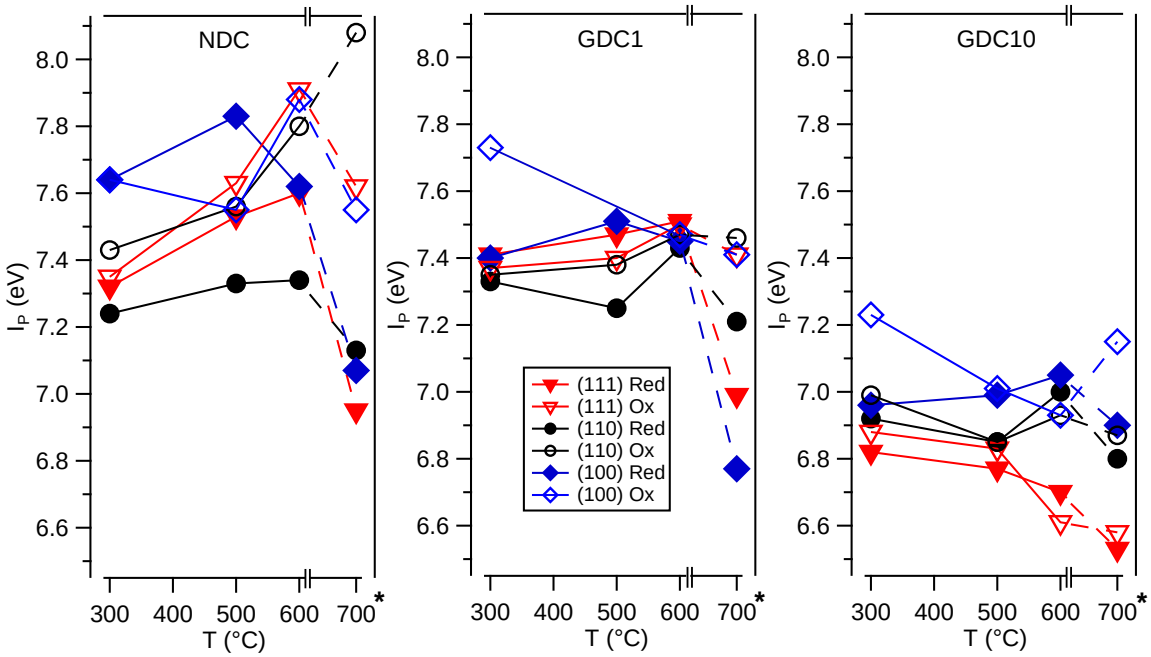

Fig. 5.7: Ionization potential in dependence of deposition temperature ($\leq$ 600 °C) of 1.3 cat.% Nb-doped CeO_2 (NDC) and ceria films doped with 0.95 cat.% Gd (GDC1) and 9.5 cat.% Gd (GDC10). Films were either deposited in 100 % Ar (Red) or a 10 % O_2/90 % Ar mixture (Ox). Post-deposition annealing at 700 °C (*) for 2 h in vacuum (Red) or 0.5 Pa O_2 (Ox) is included.

The ionization potentials of differently doped and oriented ceria films in dependence of temperature are shown in Fig. 5.7. For 0.95 cat.% Gd doped CeO_2 (GDC1), the variation of I_P, except for the (100) oriented films treated under oxidizing conditions, is comparable to undoped CeO_2. For deposition temperatures up to 600 °C the ionization potential is around 7.4 eV. After annealing at 700 °C under reducing conditions, I_P decreases for all orientations. With a decrease of 0.6 eV this effect is the most pronounced for the (100) oriented film as can be expected for the polar type III surface. A lower surface dipole due to surface reduction by oxygen removal has been discussed in the previous section for undoped CeO_2.

A similar decrease of I_P at 700 °C can be seen for 1.3 cat.% Nb-doped CeO_2 (NDC). The NDC films deposited with 100 % Ar as process gas (Red) show only small variations of the ionization potential for T $\leq$ 600 °C. In contrast, an increase of $I_P \sim 0.5$ eV with temperature under oxidizing conditions for (111) and (110) oriented films is observed.

Such a trend could be expected for polar (100) oriented films, as seen for (100) oriented undoped ceria (cf. Fig. 5.3), but is surprising for unpolar (111) and (110) surfaces, especially because this behavior is different compared to GDC and UDC. This increase of the ionization potential may therefore be related to a slight Nb-dopant segregation at the surface. However, such a Nb segregation does not seem to occur under reducing conditions, when the surface is expected to be stronger reduced with a higher concentration of oxygen vacancies present. While the positively charged vacancies at the surface might attract negatively charged acceptors, the segregation of positively charged donors, such as $Nb_{Ce}^{\bullet}$ in CeO_2, to a reduced surface is unlikely as long as solubility of the donors is generally high enough.

Besides a small decrease of ~ 0.2 eV with temperature for the (111) oriented films, independent of oxygen pressure, the ionization potential of the 9.5 cat.% Gd doped CeO_2 (GDC10) films is rather constant around 6.9 eV for all temperatures. The only exception is the (100) oriented film deposited at 300 °C with 10 % oxygen in the sputter gas (Ox). For GDC1 and GDC10, these films have a higher I_P, which decreases with increasing temperature. The significantly lower ionization potential of GDC10 compared to NDC, UDC and GDC1 is assumed to be related to a Gd segregation to the surface and will be discussed further below in more detail.

In Fig. 5.8 the ionization potentials as a function of the Ce^{3+} concentration of the differently oriented and doped CeO_2 samples are shown together with the data for nominally undoped ceria. The general trend for NDC and GDC1 is comparable to the undoped samples. With the Ce^{3+} concentration as a measure of surface reduction, which should be inversely proportional to the oxygen concentration at the surface, the decrease of I_P with $c(Ce^{3+})$ fits the expected reduction of the surface dipole when oxygen is removed from the surface.

High Ce^{3+} concentrations ≥ 22 cat.% could only be reached for (100) oriented films. (111) and (110) oriented films, although treated simultaneously on the same sample holder, do not show the same high reduction of the surface as (100) oriented films. From literature, it is known that the (100) surface of CeO_2 is more reducible than the (110) and (111) orientation [133–135]. While this explains why only the (100) oriented doped films are strongly reducible, it is still unclear why the (111) and (110) surfaces of UDC can be strongly reduced. A reason for this could be the change in defect concentrations caused by doping. In the case of NDC, adding donors to ceria will increase the polaron concentration by roughly the donor concentration, but at the same time the oxygen vacancy concentration in the bulk decreases drastically compared to nominally undoped CeO_2 in the experimentally accessible pO_2 range (cf. Fig. 3.5). Thus, donor-doping

might suppresses the thermal reduction reaction, which could explain why NDC is not as reducible as UDC.

The influence of trivalent dopants on the reducibility of ceria is controversially discussed in literature. While some authors reported a lower reducibility of ceria due to acceptor-doping [136, 137], there are also reports about an increased reducibility by acceptor-doping [24, 99]. In these reports, reducibility is usually understood as the ability of the material to release oxygen by vacancy formation. In undoped ceria, oxygen vacancies are compensated by the reduction of Ce^{4+} to Ce^{3+} (polaron formation), which can be seen in a change in the Ce^{3+} concentration, but the situation in acceptor-doped ceria is different as oxygen vacancies are mostly compensated by acceptor atoms. In GDC, the higher concentration of $V_O^{\bullet\bullet}$ at grain boundaries and at the surface is expected to be compensated by Gd segregation [63, 131, 138–141]. It is possible, that an increase of Gd segregation to the surface is more likely than an increase of polarons when the sample is annealed to reduce the surface. This could explain why high Ce^{3+} concentrations of more than 22 cat.% could only be achieved for (100) oriented GDC films but not for (111) and (110) oriented GDC films.

Different than NDC and GDC1 films, which have a similar dependence of the ionization potential on $c(Ce^{3+})$ as UDC, the higher doped GDC10 films do not share this trend and have a significantly lower I_P. The average distribution of data points of GDC10 is shifted by ~ 0.5 eV to lower ionization potentials. This is likely related to the segregation of Gd to the surface [63, 139–141]. Fig. 5.9 shows the Gd surface concentration determined by XPS in dependence on the temperature the samples were deposited or annealed at. All measured Gd concentrations are above the specified Gd content of 9.5 cat.% of the sputter target, indicating an accumulation of Gd at the surface for all films. In addition, a significant increase of c(Gd) with temperature occurs. With an increase by nearly a factor of 2, the segregation of Gd is the most pronounced for the (100) oriented films. An increase of Gd segregation with increasing annealing temperatures as well as a higher Gd fraction at the surface for (100) oriented films compared to (111) oriented samples has also been reported by Harrington [142]. However, the ionization potential of (111), (110) and (100) oriented GDC10 is independent of the Gd concentration as shown in the left part of Fig. 5.9. I_P of the films is distributed roughly between 6.5 eV and 7.1 eV. Even though the (100) oriented films have higher Gd concentrations, the ionization potential seems not to be significantly affected by this. Only a small trend of the average ionization potential with surface orientation can be seen, as $I_P(100) > I_P(110) > I_P(111)$. Nevertheless, it seems plausible to assume that the lower I_P of GDC10 compared to NDC, UDC and GDC1 (see Fig. 5.8) is related to the high Gd-doping concentration. A possible explanation could be the formation of a Gd_2O_3 surface phase, that would define the surface potential. Since all measured Gd concentrations are still far below the expected solubil-

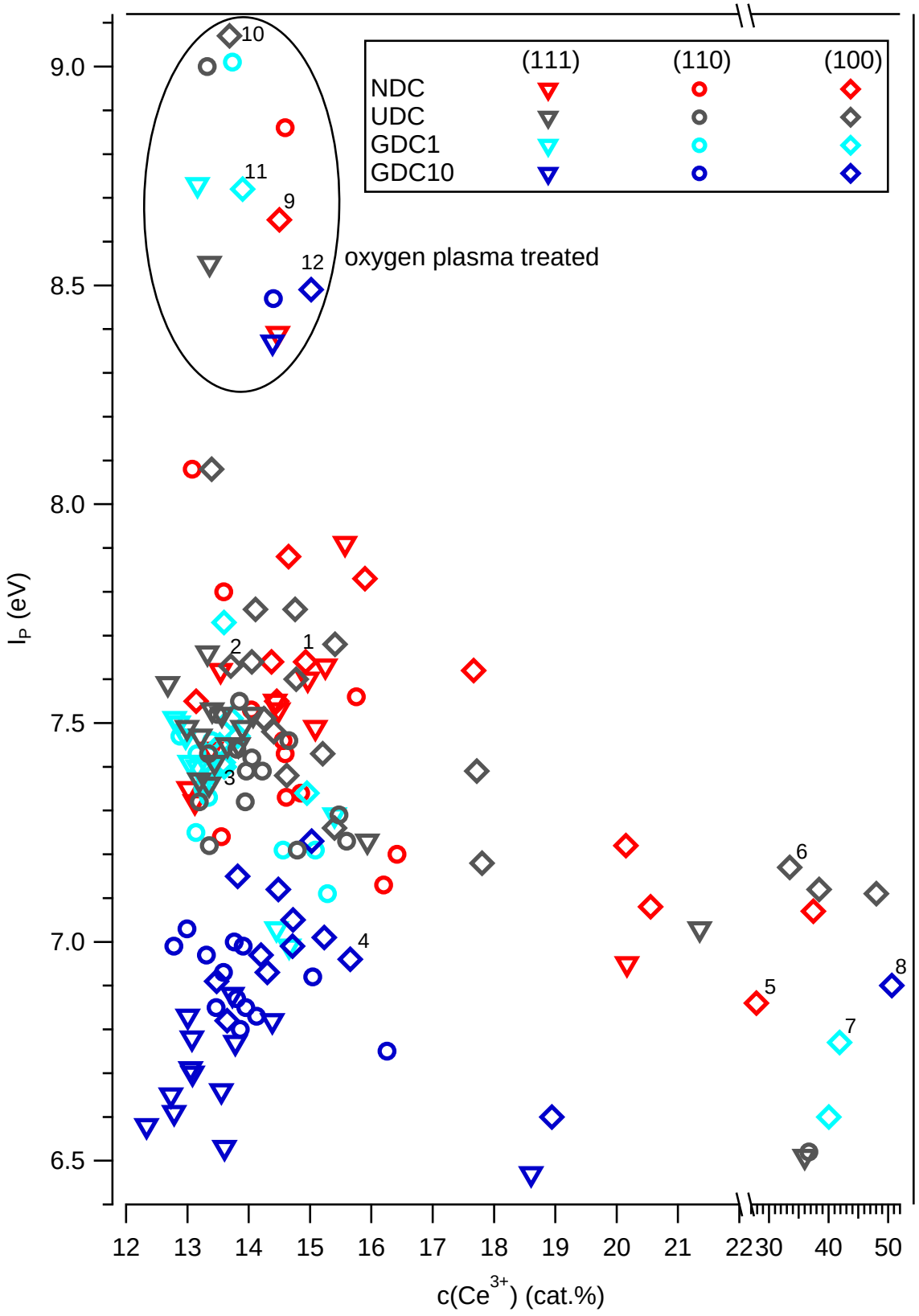

Fig. 5.8: Ionization potential as a function of Ce^{3+} concentration of 1.3 cat.% Nb-doped (NDC) and undoped (UDC) CeO_2 and ceria films doped with 0.95 cat.% Gd (GDC1) and 9.5 cat.% Gd (GDC10). Numbers 1-12 correspond to spectra shown in Fig. 5.10.

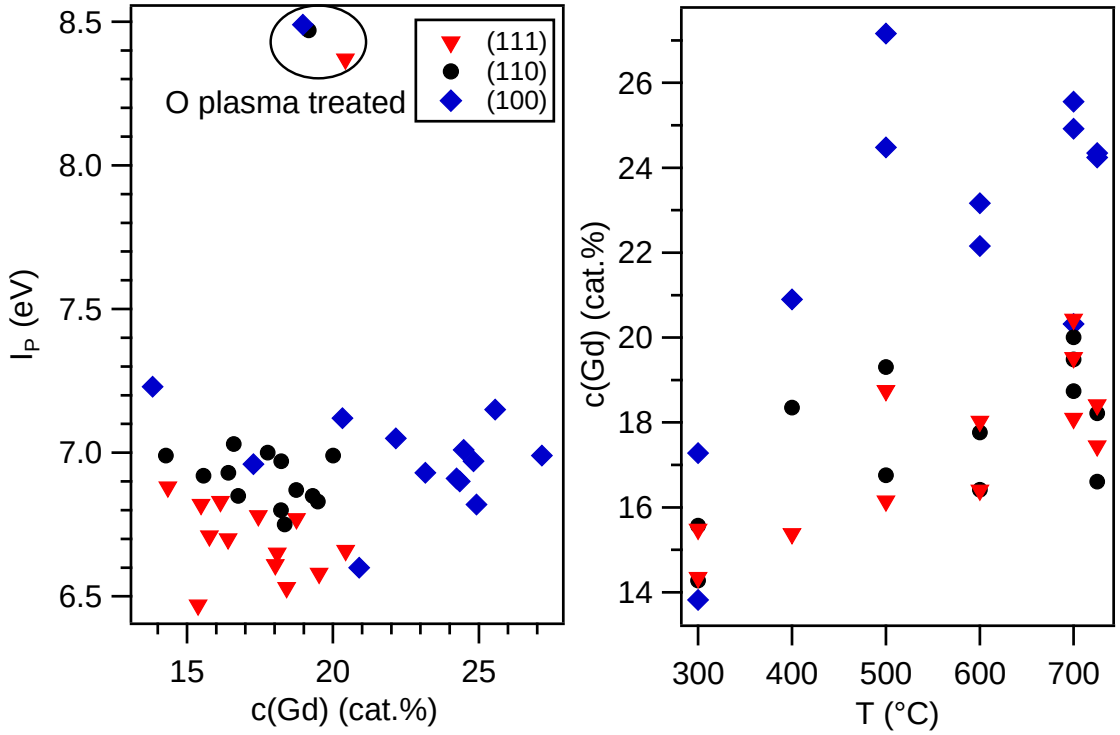

Fig. 5.9: Ionization Potential of differently oriented GDC10 films in dependence of Gd surface concentration and dependence of Gd segregation on treatment temperature.

ity limit of around 50 cat.% Gd in CeO_2 [143] and no additional crystalline phases are detected in XRD, nor a second, amorphous phase is observed at GDC grain boundaries [66], this explanation appears unlikely. However, another hypothesis is that the high acceptor concentration, which is generally reducing the oxygen content in the material, is also causing a permanent reduction of the oxygen content at the surface, which would then reduce the surface dipole. A supporting indicator for this explanation could be that the ionization potential of GDC10 is in the same range as the I_P of thermally reduced NDC, UDC and GDC1 samples with high Ce^{3+} concentrations.

This point becomes clearer by comparing the O1s spectra of the films (see Fig. 5.10)[2]. The O1s spectra of (100) oriented, as deposited NDC, UDC and GDC1 (spectra 1-3) show shoulder emission lines at approximately 1.5 eV higher binding energies compared to the main peak, which has been attributed to hydroxyl species on the surface in the previous section. In contrast, the O1s spectrum of the as deposited GDC10 film shows a pronounced shoulder peak at 2.4 eV higher binding energies compared to the main

[2] Although only spectra of (100) oriented films are shown, the discussed features in the spectra could also be found less pronounced for (111) and (110) oriented samples. Since the binding energy of the O1s core level shifts with Fermi level position, which is influenced by doping and sample treatment, all main O1s emission lines in the graph were shifted to 529.7 eV for better comparability of the shoulder emissions.

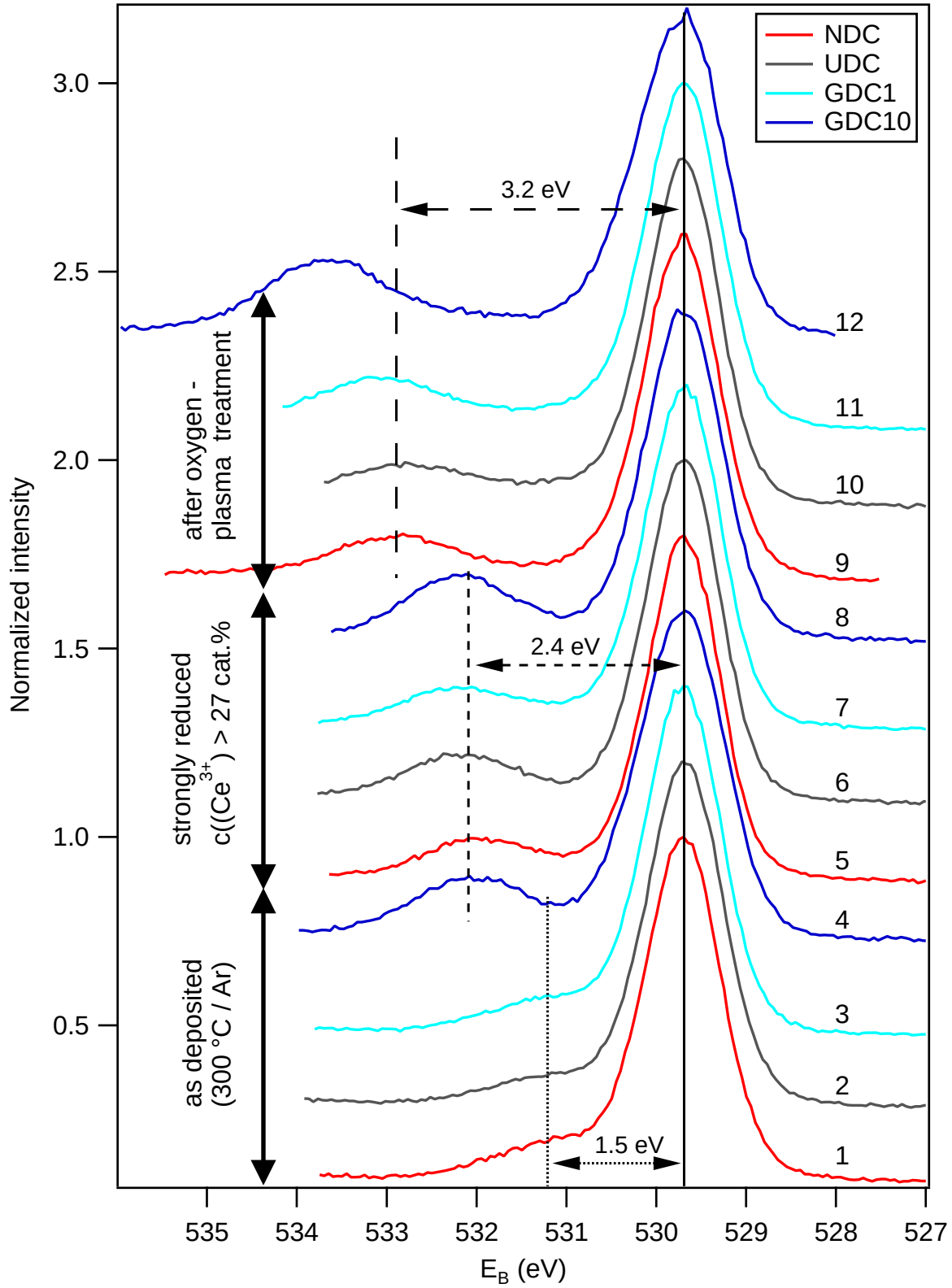

Fig. 5.10: Normalized O1s XP spectra of (100) oriented NDC, UDC, GDC1 and GDC10 films as deposited at 300 °C in Ar (1-4), after annealing at 700°C under reducing conditions (5-8) and after oxygen plasma treatment (9-12). Main peaks of spectra are all shifted to 529.7 eV for better comparison of shoulder emissions. Numbers 1-12 correspond to labeled data points in Fig. 5.8.

peak. Similar shoulder emission lines appear for Nb-, Gd- and undoped ceria films with high Ce^{3+} concentrations (> 27 %) after annealing in reducing atmosphere (spectra 5-8). In literature, this peak is attributed to a next neighbor effect from oxygen vacancies [73, 126] and would thus be related to the vacancy concentration in the material[3]. While high vacancy concentrations are achieved by thermal reduction in lower doped and undoped CeO_2, it is caused directly by the high Gd-doping concentration in GDC. Since the reduced films and all GDC10 films show the same feature in the O1s spectrum it seems reasonable to assume that the generally higher oxygen vacancy concentration in strongly doped GDC has the same effect on the ionization potential as strong surface reduction for undoped ceria. This would explain that I_P of all GDC10 films is in the same range as the ionization potential for NDC,UDC and GDC1 with high Ce^{3+} surface concentrations, as shown in Fig. 5.8. Nonetheless, this might be coincidence. Taking into account the results from Zurhelle *et al.* another explanation for the lower ionization potential of GDC10 compared to ceria with lower doping concentrations appears more likely. Zurhelle *et al.* report a very narrow space charge surface layer of less than 1 nm for acceptor-doped (20 % Sm) CeO_2 with a space charge potential of up to 0.8 eV [132]. In Fig 5.11 the effect of such a narrow space charge layer on the measured I_P of GDC10 is illustrated. Due to the narrow space charge region, the measured binding energy of the valence band is determined by the bulk value. However, the Fermi level position at the surface determines the work function. Since the ionization potential is calculated as the sum of BE_{VBM} and ϕ, the obtained I_P is significantly lower.

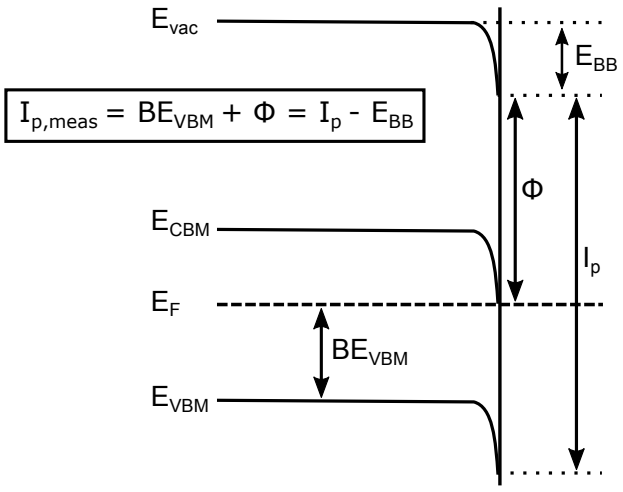

Fig. 5.11: Influence of surface space charge layer on the measured ionization potential of Gd-doped CeO_2.

[3] This peak attribution in a general matter should be considered with caution. In a conventional semiconductor model with delocalized electrons, the charge of the oxygen vacancy would be distributed over a wide volume, thus making only an insignificant change in the binding energies. However, in the case of CeO_2 the strongly localized character of the f-electrons could enable the measured binding energy shift of 2.4 eV.

Spectra 9-12 in Fig. 5.10 show the O1s spectra of the films after oxygen plasma treatment. Here, a shoulder peak at ~ 3 eV from the main peak occurs. As already discussed for undoped CeO_2, this peak is likely related to surface peroxide species [87, 128], which are determining the huge increase of the measured ionization potential of ceria for all investigated surface orientation and doping concentration (see Fig. 5.8). While this shoulder emission is similar for undoped ceria and CeO_2 with low doping concentrations, it is shifted by approximately 0.7 eV to higher binding energies for GDC10. Furthermore, the shoulder emission 2.4 eV from the main peak, that is seen for reduced and all GDC10 films, disappears. Since this peak is indirectly related to the oxygen vacancy concentration, this suggests that the oxygen plasma treatment annihilates the oxygen vacancies at the surface.

5.2.2 Fermi level positions of doped CeO_2

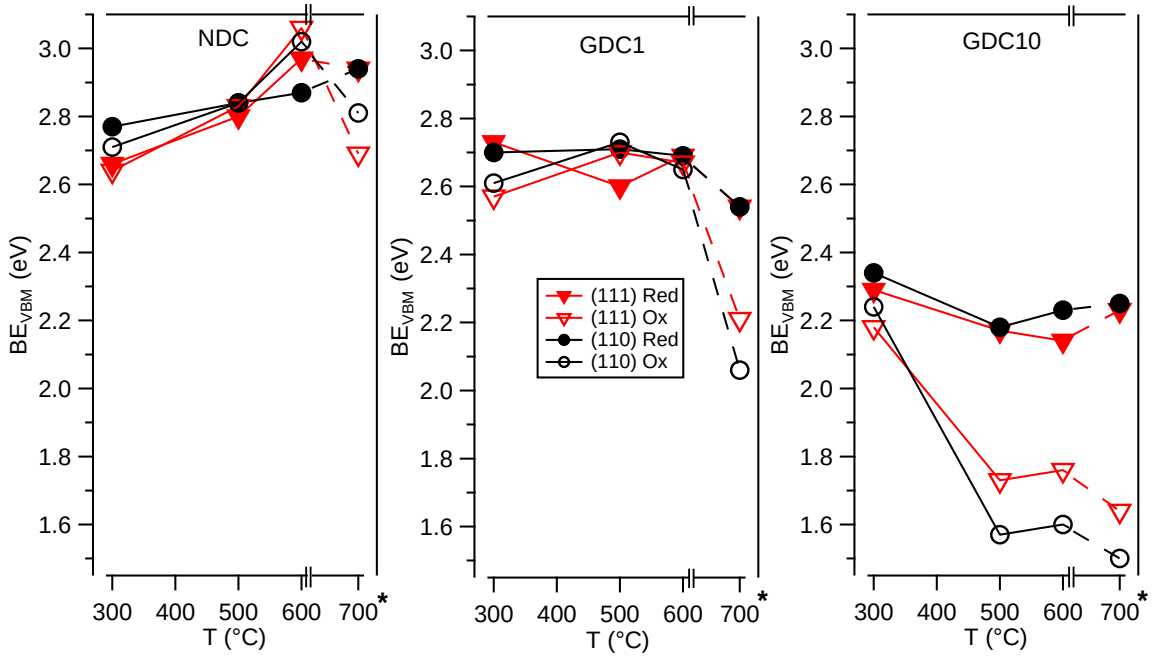

Fig. 5.12: Fermi level in dependence of deposition temperature ($\leq$ 600 °C) of 1.3 cat.% Nb-doped CeO_2 (NDC) and ceria films doped with 0.95 cat.% Gd (GDC1) and 9.5 cat.% Gd (GDC10). Films were either deposited in 100 % Ar (Red) or a 10 % O_2/90 % Ar mixture (Ox). Post-deposition annealing at 700 °C (*) for 2 h in 0.5 Pa Ar (Red) or 0.5 Pa O_2 (Ox) is included.

The Fermi level positions as a function of temperature under reducing and oxidizing conditions for differently doped CeO_2 films are depicted in Fig. 5.12. Due to the substrate effect on the measured Fermi level of (100) oriented films, which has already been

discussed in the previous section, only (111) and (110) oriented films deposited on Pt are shown. For Nb-doped ceria, a small rise of BE_{VBM} with temperature similar to the trend of undoped CeO_2 is observed. This would generally fit the description given for UDC, where more reducing conditions at higher temperature cause an increase in oxygen vacancy concentration, resulting in polaron formation. However, this does not match with the defect chemistry of NDC. The electron (polaron) concentration in NDC should be mostly determined by the Nb-dopant, hence, be largely independent on the chemical potential of oxygen, while the oxygen vacancy concentration should negligibly low [28]. Nevertheless, instead of polarons, oxygen interstitials could partially compensate the donor-doping at oxidizing conditions resulting in a lower E_F, which might be the reason for the observed temperature dependence of the measured BE_{VBM}.

The Fermi level position of GDC1 appears to be independent of atmosphere and deposition temperatures for T$\leq$ 600 °C with a value around 2.7 eV. After annealing at 700 °C in 0.5 Pa O_2, BE_{VBM} decreases by nearly 0.5 eV.

For GDC10 deposited at 300 °C, the Fermi level position is similar with $2.2-2.3$ eV for films treated under reducing and oxidizing conditions. While under reducing conditions, the Fermi level does not change significantly at higher temperatures, E_F is $0.4-0.7$ eV lower when treated in oxidizing atmosphere at temperatures $\geq$ 500 °C. The decrease of the Fermi level under oxidizing conditions for Gd-doped films can be explained by electron hole generation due to oxidation of oxygen vacancies, which are present because of the acceptor-doping. The difference of E_F between oxidizing and reducing conditions should in principle be detected for all temperatures, but it is likely that the defect concentrations of samples deposited at 300 °C are not in equilibrium. Sputtered films have typically a high defect concentration and the substrate temperature during sputtering might not be high enough in order to enable the film to reach equilibrium within the time of the experiment. The same effect is likely for GDC1, however, higher temperatures are needed in order to equilibrate the sample propably due to the much lower diffusivity or oxygen exchange of GDC1 compared to GDC10 [144].

Fig. 5.13 shows the Fermi level position as a function of Ce^{3+} concentration in comparison for all (111) and (110) oriented films . In principle, E_F for all differently doped samples show a similar increasing trend with increasing c(Ce^{3+}) as would be expected. BE_{VBM} of NDC and UDC films are in the same range and vary by maximum 0.4 eV. Despite the n-doping of NDC, significantly higher Fermi level positions compared to undoped ceria were not found. This behavior fits the aforementioned maximum E_F of around 3 eV limited by the position of the Ce4f states [32–34, 109], as already discussed in more detail in the previous section for undoped CeO_2.

GDC1 and especially GDC10 have lower Fermi level positions than NDC and UDC as can be expected for a p-doped material. In addition, huge variations of E_F up to 1.1 eV

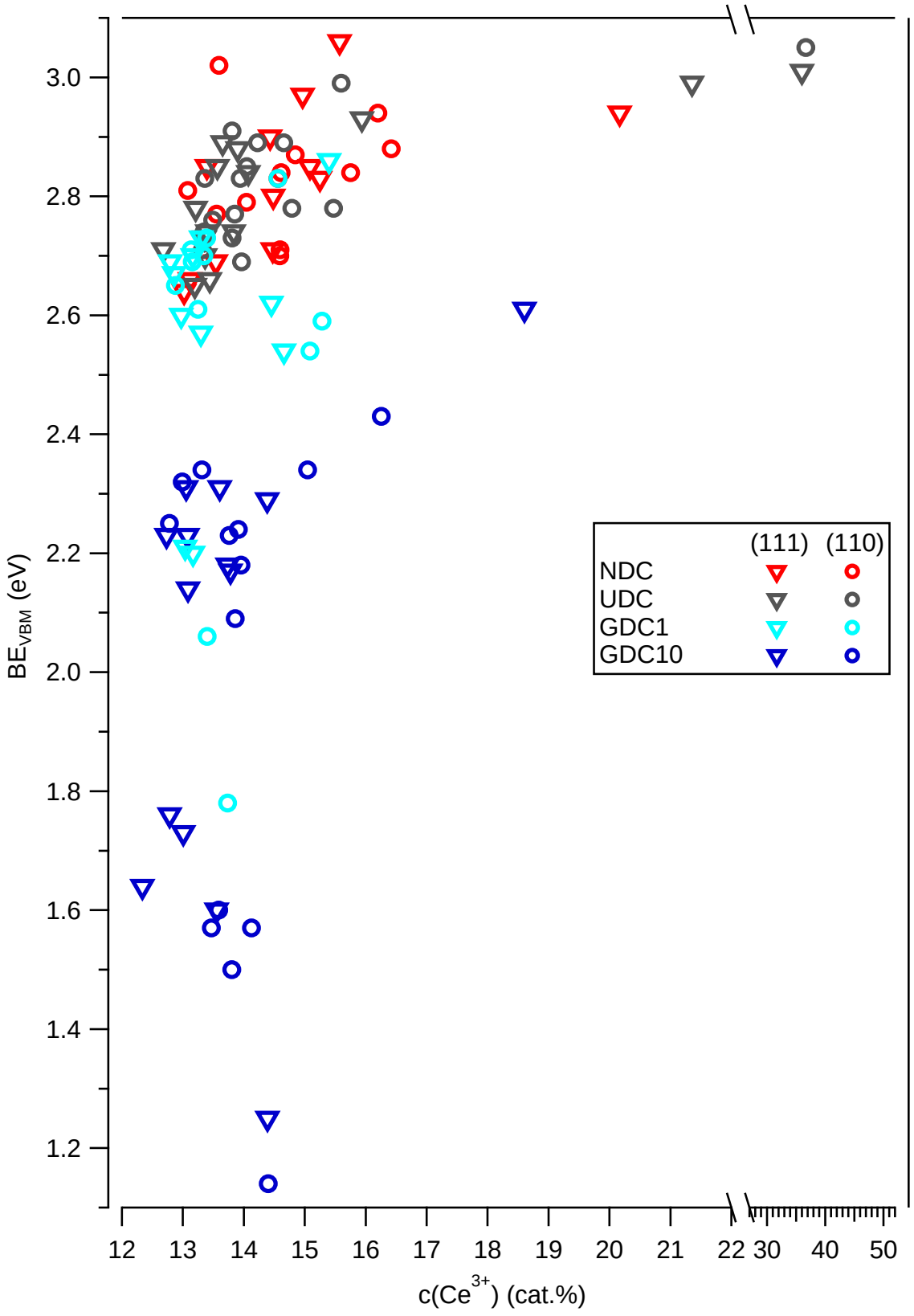

Fig. 5.13: Fermi level position as a function of Ce^{3+} concentration of 1.3 cat.% Nb-doped (NDC) and undoped (UDC) CeO_2 and ceria films doped with 0.95 cat.% Gd (GDC1) and 9.5 cat.% Gd (GDC10).

for GDC1 and 1.5 eV for GDC10 were found depending on weather the samples were treated in oxidizing or reducing atmosphere. Including differently doped samples, this results in an overall Fermi level variation of 1.9 eV in CeO_2, which is high compared to that observed for other oxides so far. In order to explain these huge variations, especially those observed in Gd-doped films, the measured E_F will be compared with expected Fermi level positions obtained from point defect calculations.

5.2.3 Comparison with calculated Fermi level positions (doped CeO_2)

Fig. 5.14 displays the calculated Fermi level positions as well as the expected Fermi level positions after quenching to room temperature in comparison to experimentally obtained values. The samples deposited at 300 °C were very unlikely in equilibrium and will thus not be included in the following discussion.
Since the electron concentration in NDC is expected to be determined by the Nb-doping concentration, it is not surprising that the calculated bulk Fermi level position is close to the conduction band and not depending on the oxygen partial pressure. Within the measurement error, there is a good agreement between the measured BE_{VBM} and the calculated bulk Fermi level position. As for UDC, this indicates that a possible surface space charge layer has to be very narrow, so that mostly bulk is probed by XPS.
The measured Fermi level of GDC1 coincides well with $E_{F,qu}$ at 500 and 600 °C. These data points should, however, be considered with care, because it is likely that the corresponding samples were not in equilibrium. At 700 °C the experimental values lie between the calculated E_F and $E_{F,qu}$. This behavior can be expected since the cooling rate after deposition or annealing is too low to produce well quenched samples. When taking into account that the measured data should lie between calculated E_F and $E_{F,qu}$ it becomes evident, that for GDC10, the measured and calculated data do not fit properly. While the Fermi level at $\log pO_2 = -11$ is located in between E_F and $E_{F,qu}$, the data points at higher oxygen pressures match the Fermi level at high temperature or, as for 700 °C, are even below that level.
To understand the measured Fermi level positions in Gd-doped ceria, especially the huge variation of E_F, the Fermi level position after the sample has been quenched to room temperature is important to be considered in more detail. While the high temperature Fermi level only shows relatively small changes within the investigated pO_2 range, $E_{F,qu}$ shows a sharp drop of more than 1.5 eV at the transition where the material switches from n- to p-type, i.e. when more electron holes than electrons are present. The oxygen pressure at which this transition occurs depends on the acceptor concentration and on the charge transition level of the acceptor. The calculations shown in Fig. 5.14 assume that every Gd acceptor in CeO_2 is always charged, which means that the charge transition

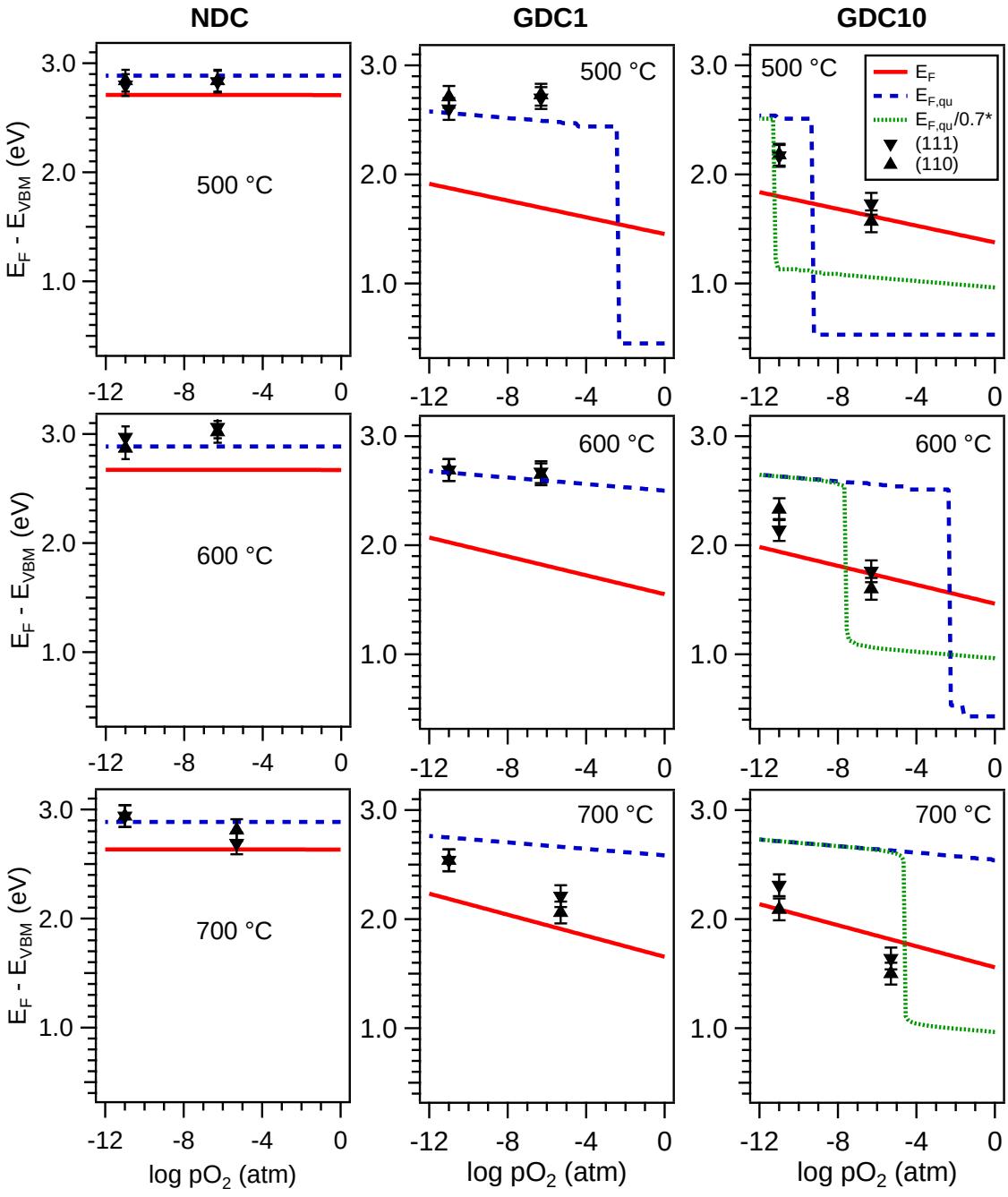

Fig. 5.14: Calculated Fermi level position at high temperatures and after quenching to room temperature for 1.3 cat.% Nb-doped CeO_2 (NDC) and ceria films doped with 0.95 cat.% Gd (GDC1) and 9.5 cat.% Gd (GDC10) at different temperatures in comparison with experimental data. $E_{F,qu}/0.7^*$ corresponds to a calculation assuming the Gd^{4+}/Gd^{3+} charge transition level 0.7 eV above the valence band. Details of the calculations are given in section 3.4.

level Gd^{4+}/Gd^{3+} is at the valence band maximum. By shifting this level into the band gap, the transition from high to low $E_{F,qu}$ shifts to more reducing conditions. The green dotted lines in Fig. 5.14 depict the $E_{F,qu}$ calculated with the charge transition level 0.7 eV above the valence band for GDC10.

By shifting the n- to p-type transition to lower oxygen pressures, the experimental E_F is in better agreement with the expectation, that the measured Fermi level positions should be between the high temperature E_F and $E_{F,qu}$, although the accordance is still not ideal. It is possible that the above mentioned Gd segregation is partially responsible for these deviations, since the Gd concentration influences at which pO_2 the drop in $E_{F,qu}$ occurs. It should be noted that a different charge transition level does not affect the equilibrium Fermi level at elevated temperatures.

The influence of the charge transition level on the Fermi level positions of quenched samples enables, in principle, the determination of the Gd^{4+}/Gd^{3+} transition level within the electronic bandgap of ceria. By annealing a sample in different atmospheres over a wide oxygen partial pressure range, subsequent quenching to room temperature and measuring BE_{VBM} with XPS, $E_{F,qu}$ can theoretically be monitored. By adjusting the model to fit the data, the charge transition level of Gd could be identified. The results of such an experiment can be seen in Fig. 5.15. Unfortunately, the sharp transition of the quenched Fermi level could not be observed clearly in the experiment. While a general increase in BE_{VBM} is observed with decreasing oxygen pressure, only a small step can be seen from $\log pO_2 = -6.3$ to $\log pO_2 = -7$. This is not significant enough for a unique determination of the charge transition level of Gd in CeO_2. The reason for this is likely the high oxygen diffusivity of $\sim 6 \times 10^{-7}$ cm^2/s in GDC10 (cf. chapter 8) combined with the still too low quenching rates in the vacuum chamber, although quenching was performed by directly transferring the hot sample together with the sample holder onto a cold steel block. In addition to the generally low cooling rates in vacuum, where heat is mostly dissipated by radiation, the large mass of the sample holder might strongly limit the cooling rates.

Nevertheless, if faster quenching options can be realized, such an experiment could be a simple, yet powerful tool to determine the charge transition levels of acceptors in oxide semiconductors.

5.3 Summary

In this chapter, the Fermi level position, work function and ionization potential of undoped and differently doped ceria thin films were investigated in dependence of surface orientation and reduction. The executed investigation constitutes, to the author's best

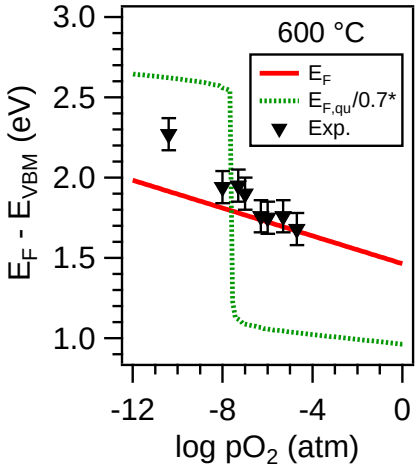

Fig. 5.15: Calculated Fermi level position at high temperatures and after quenching to room temperature assuming the Gd^{4+}/Gd^{3+} charge transition level 0.7 eV above the valence band for 9.5 cat.% Gd-doped CeO_2 (GDC10) in comparison with experimental data of samples annealed at 600 °C at different pO_2 with subsequent quenching to room temperature.

knowledge, the first systematic study of the work function of a material with fluorite structure.

The comparisons of the measured Fermi level position of undoped and Nb-doped CeO_2 with calculated Fermi level positions from point defect calculations reveals a similar E_F at the surface and in the bulk. This indicates that a possible space charge region at the surface, if present at all, has to be very narrow compared to the information depth of the XPS. For Gd-doped ceria this comparison is not conclusive, because the defect concentrations of the films are not defined. The low diffusivity or oxygen exchange causes the defect concentration in the film to be determined by the deposition. In addition, the slow quenching rates result in an undefined state of the samples at room temperature.

A dependence of the ionization potential on the surface orientation, which is expected from the corresponding Tasker types of the surfaces, is not observed. It is expected that the surface dipole of the polar type I (100) surface of ceria strongly depends on surface termination and thus sample treatment, while the non-polar (110) and (111) type I and II surfaces should only show small variations of the ionization potential. In contrast to this, huge variations of the ionization potential are found for all surface orientation, although more pronounced for the (100) surface. The similar behavior of the different surface orientations must be related to details of the surface reconstruction. The formation of facets on a nanometer scale might contribute to this behavior. Furthermore, the high Ce^{3+} concentrations observed even for fully oxidized samples can be understood as a consequence of the oxygen deficiency caused by the surface reconstruction. Another possible explanation for the high Ce^{3+} concentration could be the existence of a surface

dipole involving Ce^{3+} and peroxide species, that could be also related to surface reconstruction. The similar Ce^{3+} surface concentration for acceptor-, donor- and undoped CeO_2 suggests that such a dipole might exist instead or in addition to a surface space charge layer.

The surface potentials of (111) and (110) oriented and differently doped CeO_2 films are summarized in Fig. 5.16. As discussed above, UDC and NDC films only show relatively small Fermi level variations of $\sim$ 0.4 eV, while variations of up to 1.5 eV of E_F are observed for GDC. Overall, a huge variation of the Fermi level position of 1.9 eV is found for ceria. This is higher than values reported for other oxides [18, 145]. Ionization potentials ranging from 6.5 to 9.1 eV for differently doped CeO_2 were measured with the I_P of the majority of samples around 7.5 eV and the lowest values of 6.5 eV for GDC10 films with pronounced Gd segregation. However, ionization potentials above 8.3 eV are only reached for oxygen plasma treated films. Since the work function depends on the ionization potential and the Fermi level position, the changes in I_P and E_F result in a huge overall variation of the work function of 3.9 eV for ceria depending on doping, surface orientation and sample treatment.

The results from this chapter supply the necessary data for an investigation of a correlation between work function and oxygen exchange, which is the subordinate goal of this thesis. Besides this, the knowledge of the surface potentials of CeO_2 are of general interest for the prediction of the electronic structure during interface formation with other materials.

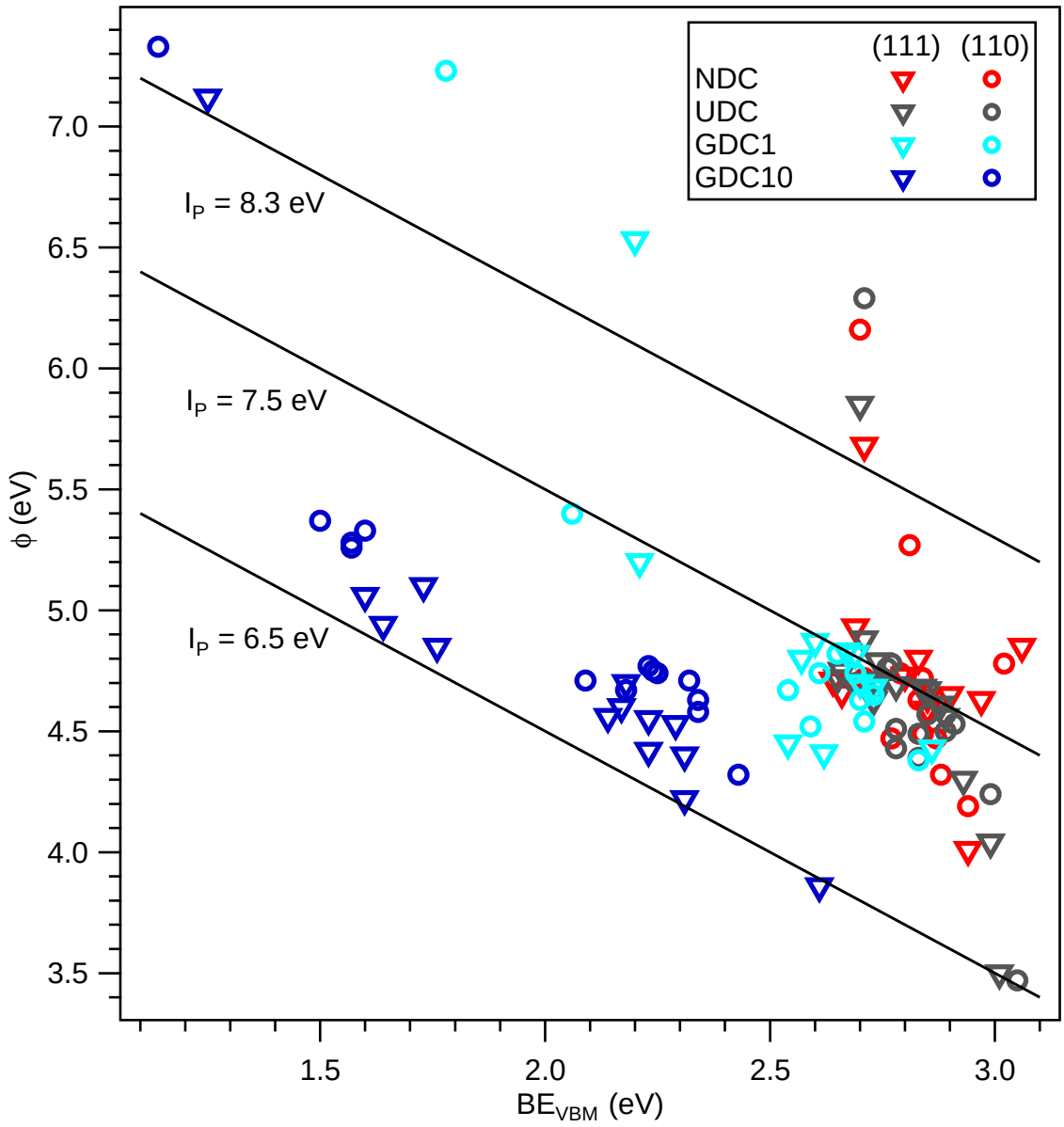

Fig. 5.16: Work function as a function of Fermi level position for 1.3 cat.% Nb-doped (NDC) and undoped (UDC) CeO_2 and ceria films doped with 0.95 cat.% Gd (GDC1) and 9.5 cat.% Gd (GDC10).

6 Electrical conductivity measurements of doped and undoped CeO_2 films

Within this chapter, the results from van-der-Pauw conductivity measurements, as described in section 3.3, will be presented. The first part of this chapter will discuss the equilibrium conductivities for doped and undoped ceria in dependence of oxygen partial pressure and temperature in comparison to calculated conductivities obtained from point defect calculations. In the second part of the chapter, the kinetics of the stoichiometry changes will be investigated to evaluate the oxygen exchange and diffusion coefficients of differently doped CeO_2.

6.1 Equilibrium conductivity of CeO_2

6.1.1 Conductivity of undoped CeO_2

The pO_2 dependence of the conductivity of a nominally undoped ceria thin film at temperatures from 500 to 650 °C is shown in Fig. 6.1. With conductivities from 1×10^{-5} S/cm^2 to 5×10^{-3} S/cm^2 at $pO_2 = 10^{-6}$ atm, the overall conductivity values are comparable to previous reports for nominally undoped CeO_2 films [69, 146, 147]. The conductivity is proportional to $pO_2{}^{-1/4}$ at higher oxygen partial pressures. With increasing temperature the pO_2 dependence of the conductivity deviates from the -1/4 slope at low oxygen pressures. Due to the high Fermi level positions ($E_F = 2.7 - 3.0$ eV) of nominally undoped ceria films presented in chapter 5, donor impurities were assumed to be present in the films causing n-doping. A -1/4 slope of the pO_2 dependence of the conductivity can be expected for donor-doped CeO_2 at higher oxygen pressures originating from donor compensation by oxygen interstitials [28].

In order to investigate possible donor impurities in the film, a secondary ion mass spectrometry (SIMS) measurement of a film deposited under the same conditions was executed (see Fig. 6.2). While no significant amount of cation impurities, that could act as donors in CeO_2, was found, fluorine and chlorine impurities were found, which could act as donors by anion substitution ($F_O^{\bullet}$ and $Cl_O^{\bullet}$).

In Fig. 6.3, calculated defect concentrations for undoped, donor-doped (D), acceptor-doped (A) and strongly compensated acceptor-doped (A+D) CeO_2 are shown in depen-

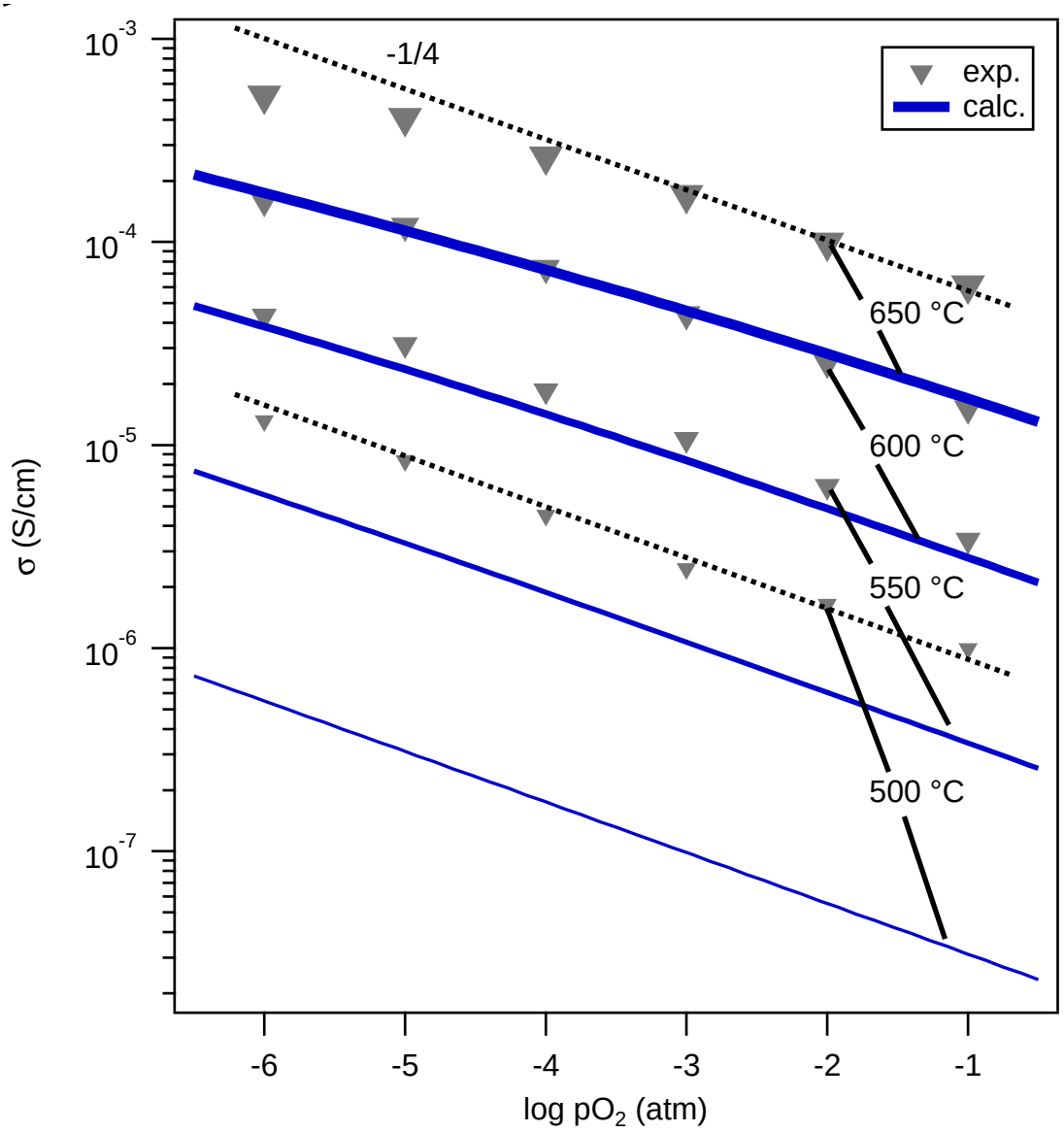

Fig. 6.1: Comparison of the oxygen partial pressure dependence of the conductivity of a CeO_2 thin film and calculated conductivities for strongly compensated acceptor doped CeO_2 ($c(\mathrm{A}) = 0.005$ cat.% and $c(\mathrm{D}) = 0.0045$ cat.%) at different temperatures. Dashed lines indicate the slope for a $pO_2{}^{-1/4}$ dependence.

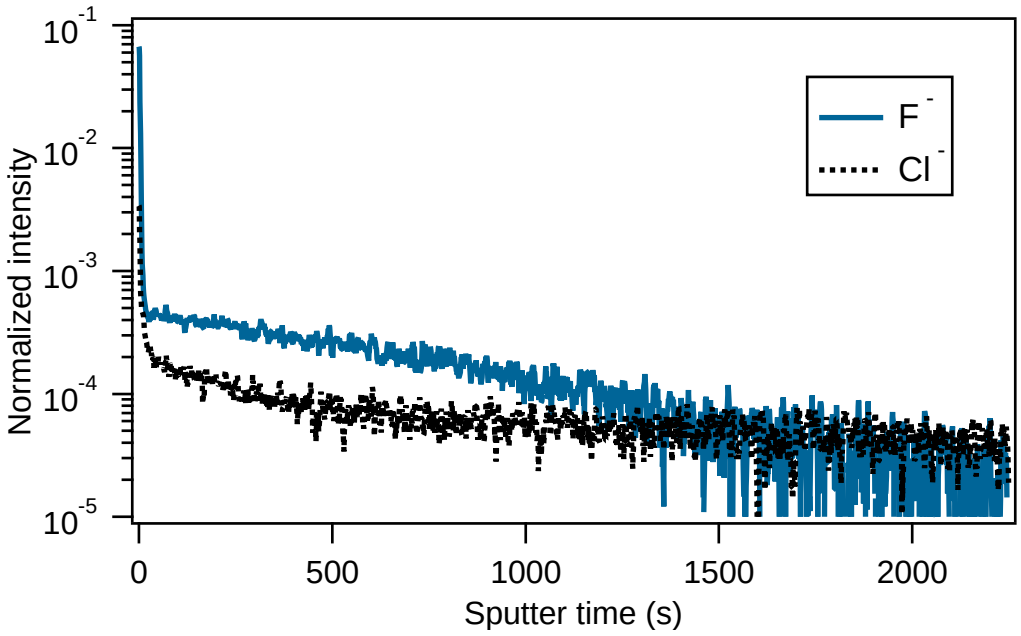

Fig. 6.2: Secondary ion mass spectrometry signal from ^{19}F and ^{37}Cl of a nominally undoped CeO_2 film. Intensity is normalized to ^{16}O intensity.

dence of oxygen partial pressure at 600 °C. The corresponding electronic conductivities are shown in Fig. 6.4. For the calculation of the donor-doped ceria, a donor concentration of $c(\mathrm{D}) = 0.001$ cat.% was used and for the acceptor-doped material an acceptor concentration of $c(\mathrm{A}) = 0.005$ cat.% which seems to be a reasonable value for a specified purity of 99.99 % of the sputter target, assuming that half of the possible impurities are active as singly charged acceptors. The defect concentrations and conductivities of the strongly compensated acceptor-doped ceria were calculated assuming an acceptor and donor concentration of $c(\mathrm{A}) = 0.005$ cat.% and $c(\mathrm{D}) = 0.0045$ cat.%, respectively, resulting in an effective p-doping with 0.0005 cat.%.

As expected for undoped ceria, the electron concentration is determined by the oxygen vacancy concentration from the thermal reduction reaction with $n \approx 2 \cdot c(V_O^{\bullet\bullet})$ resulting in a -1/6 slope of the pO_2 dependence. This regime occurs for the acceptor- or donor-doped material only at low oxygen pressures. For the donor-doped material the electron concentration and thus conductivity is independent of pO_2 even for low doping concentrations at medium oxygen pressures and n is determined by the doping concentration. At high pO_2 the electron concentration decreases slightly due to an increasing donor compensation by oxygen interstitials. It should be noted that for higher donor concentration the oxygen pressure independent region becomes larger and the region where compensation by oxygen interstitials occurs would shift to lower pO_2. In addition, an overestimation of the Gibb's free energy for Anti-Frenkel defect formation could have shifted this transition to higher oxygen pressures than expected from experimental data [28]. Nevertheless,

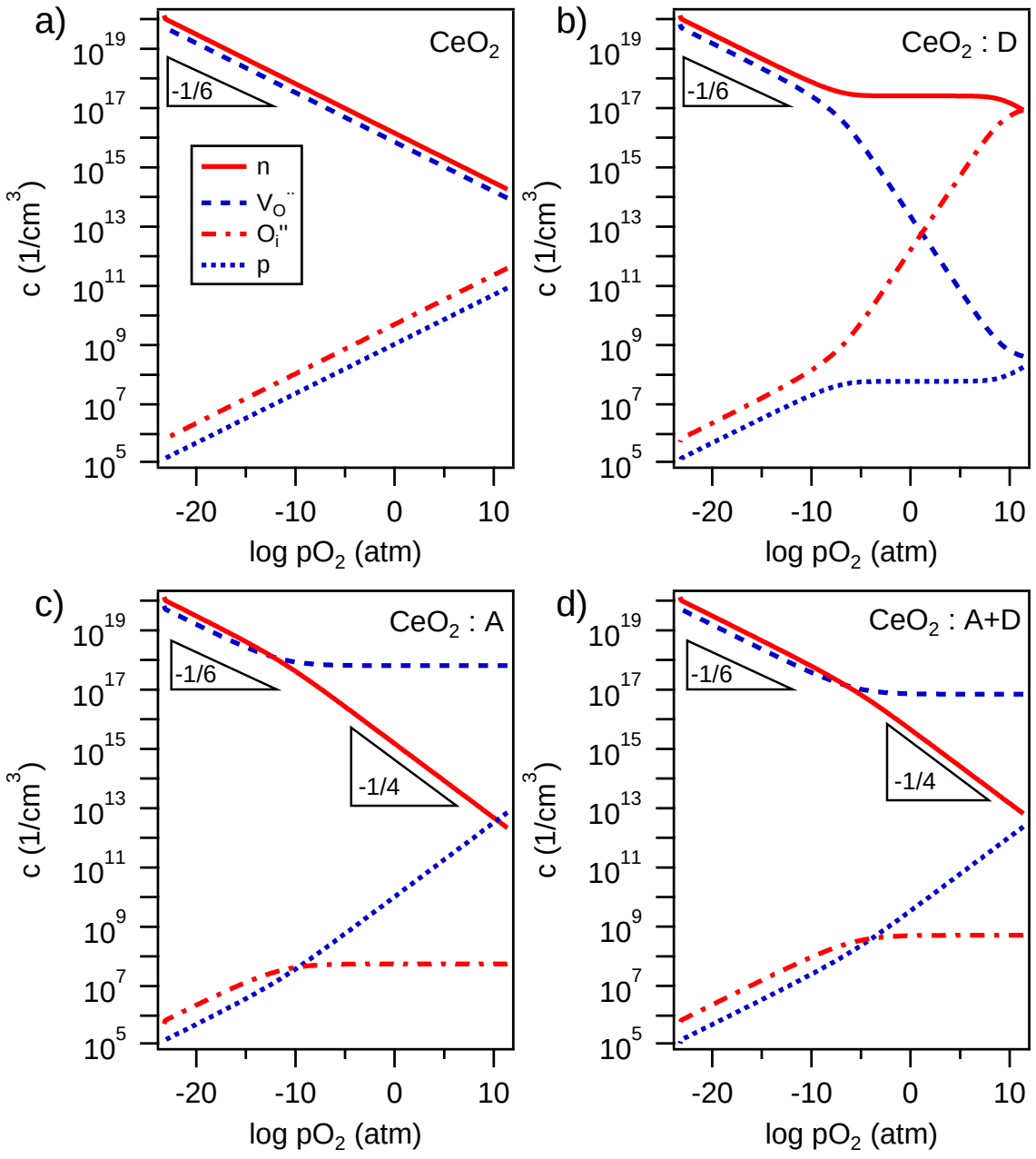

Fig. 6.3: Calculated defect concentrations at 600 °C for a) undoped CeO_2, b) donor-doped (D) CeO_2 ($c(\mathrm{D}) = 0.001$ cat.% or 2.55×10^{17} cm^{-3}), c) acceptor-doped (A) CeO_2 ($c(\mathrm{A}) = 0.005$ cat.% or 1.28×10^{18} cm^{-3}) and d) strongly compensated acceptor-doped CeO_2 ($c(\mathrm{A}) = 0.005$ cat.% and $c(\mathrm{D}) = 0.0045$ cat.% or an effective acceptor concentration $c_{eff}(\mathrm{A}) = 1.28 \times 10^{17}$ cm^{-3}).

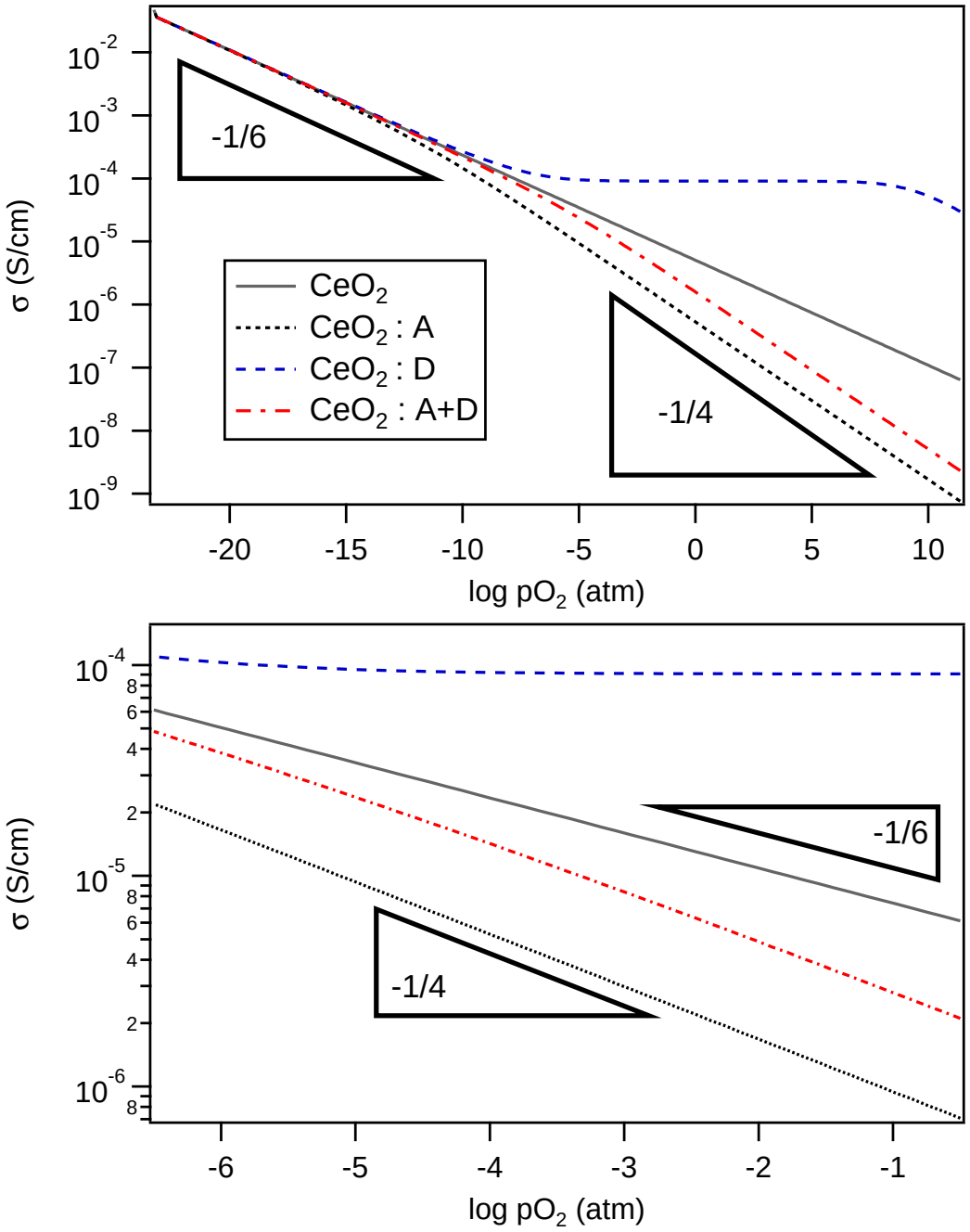

Fig. 6.4: Calculated electronic conductivities at $600\ ^\circ$C for undoped CeO_2, donor-doped (D) CeO_2 ($c(\mathrm{D}) = 0.001$ cat.%), acceptor-doped (A) CeO_2 ($c(\mathrm{A}) = 0.005$ cat.%) and strongly compensated acceptor-doped CeO_2 ($c(\mathrm{A}) = 0.005$ cat.% and $c(\mathrm{D}) = 0.0045$ cat.%). Zoom in on experimentally accessible pO_2 region is shown in bottom graph.

it is not possible to qualitatively reproduce the measured pO_2 dependence of the conductivity (see Fig. 6.1) while still using reasonable formation enthalpies. From this we conclude, that the conductivity behavior with oxygen pressure of the nominally undoped films cannot be explained solely by donor impurities.

Generally, a slope of -1/4 of the pO_2 dependence of the conductivity is assigned to acceptor impurities, which fix the oxygen vacancy concentration as can be seen from the plateau of $c(V_O^{\bullet\bullet})$ at higher oxygen pressures in Fig. 6.3c. While this reproduces the pO_2 dependence of the measured conductivities at lower temperatures (cf. Fig. 6.1), it does not fit the decreasing slope of the conductivity at higher temperatures and low pO_2. For the expected impurity concentration of the samples, the transition to the intrinsic regime with $\sigma \propto {pO_2}^{-1/6}$ is expected at lower oxygen pressures than the pO_2 range investigated by the experiment, as can be seen in Fig. 6.4. Taking compensation of acceptors by donor impurities into account, this transition shifts to higher oxygen pressures and is in better agreement with the experiment.

In Fig. 6.1 the calculated conductivities for strongly compensated acceptor-doped CeO_2 and the experimental data are compared for different temperatures and oxygen pressures. The pO_2 dependence of the calculated and measured conductivities are in good agreement. However, the calculated conductivities are significantly lower than the measured ones. At high temperatures the deviation from the experimental data is smaller than at lower temperatures. The reason for this lies in the different activation energies (E_a) between measurement (1.70 eV) and calculation (see Fig. 6.5). The calculated activation energies are 1.94 eV and 2.68 eV for undoped and acceptor-doped ceria, respectively. The activation energy for strongly compensated acceptor-doped CeO_2 lies in between these two values with $E_a = 2.43$ eV. The conductivity data at $pO_2 = 10^{-6}$ atm was used to determine E_a for better comparability to the experimental data. At this oxygen pressure the transition from oxygen vacancy generation by thermal reduction ($\sigma \propto {pO_2}^{-1/6}$) to a region where the oxygen vacancy concentration is determined by extrinsic defects ($\sigma \propto {pO_2}^{-1/4}$) takes place. Hence, it is reasonable that the activation energy of this case is in between the ones for the distinct regions.

The experimentally obtained activation energy is in good agreement with results from literature [71, 146–149]. Tschöpe *et al.* reported an activation energy of 1.7 eV for the conductivity of nanocrystalline ceria [150], indicating that the grain boundary conductivity is dominant in nanocrystalline ceria. In fact, sputtered thin films are expected to be nanocrystalline with a grain size of the order of 50 nm, which would fit to dominating grain boundary conductivity in the measured CeO_2 film. Since space charge layers at grain boundaries in CeO_2 are expected to have an increased electronic conductivity due to an electron accumulation caused by a positively charged grain boundary core [129, 130, 138, 151], a higher density of conducting grain boundaries in nanocrystalline

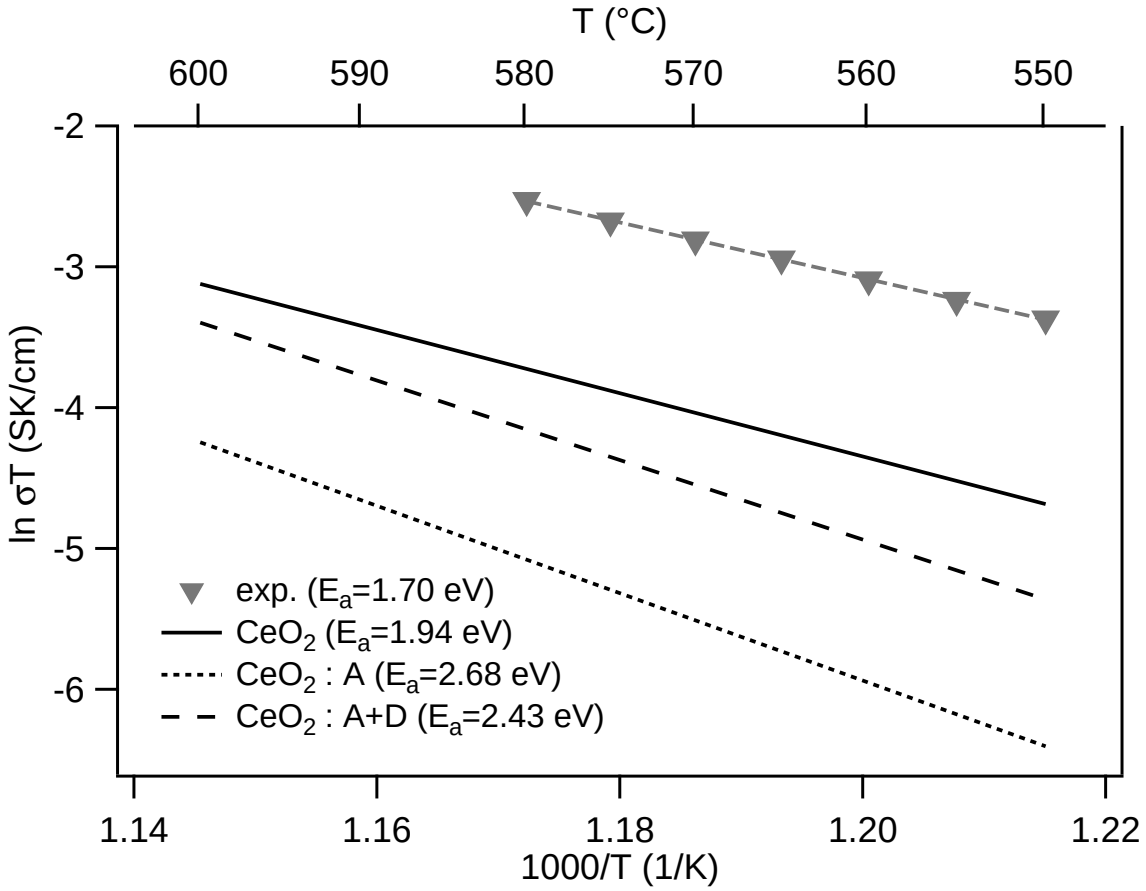

Fig. 6.5: Arrhenius plot for CeO_2 thin film and calculated data for undoped, acceptor-doped ($c(A) = 0.005$ cat.%) and strongly compensated acceptor-doped CeO_2 ($c(A) = 0.005$ cat.% and $c(D) = 0.0045$ cat.%) at $pO_2 = 10^{-6}$ atm.

ceria should lead to a higher electronic conductivity compared to samples with larger grains. Besides this "trivial" size effect, the space charge layers can overlap for very small grains causing an accumulation of electrons within the whole grain [129, 130, 151]. This fits known grain size effects from literature, where a significant decrease of the activation energy of the electronic conductivity with decreasing grain size was found. Kosacki *et al.* reported a decrease of E_a from 2.8 eV to 1 eV for a decrease of the grain size from 5 μm to 10 nm [149], while Rupp *et al.* showed a decrease from 1.55 eV to 0.9 eV with grain size decreasing from 230 nm to 37 nm [147]. These effects could be an explanation for the higher conductivity and lower activation energy of the experimental data compared to the calculated conductivities (Fig. 6.1), where microstructure effects were neglected.

6.1.2 Conductivity of Nb-doped CeO_2

The oxygen pressure dependence of the conductivity at temperatures from 500 to 700 °C for 1.3 cat.% Nb-doped CeO_2 is shown in Fig. 6.6. At low pO_2 ($\log pO_2 \leq -4$), the

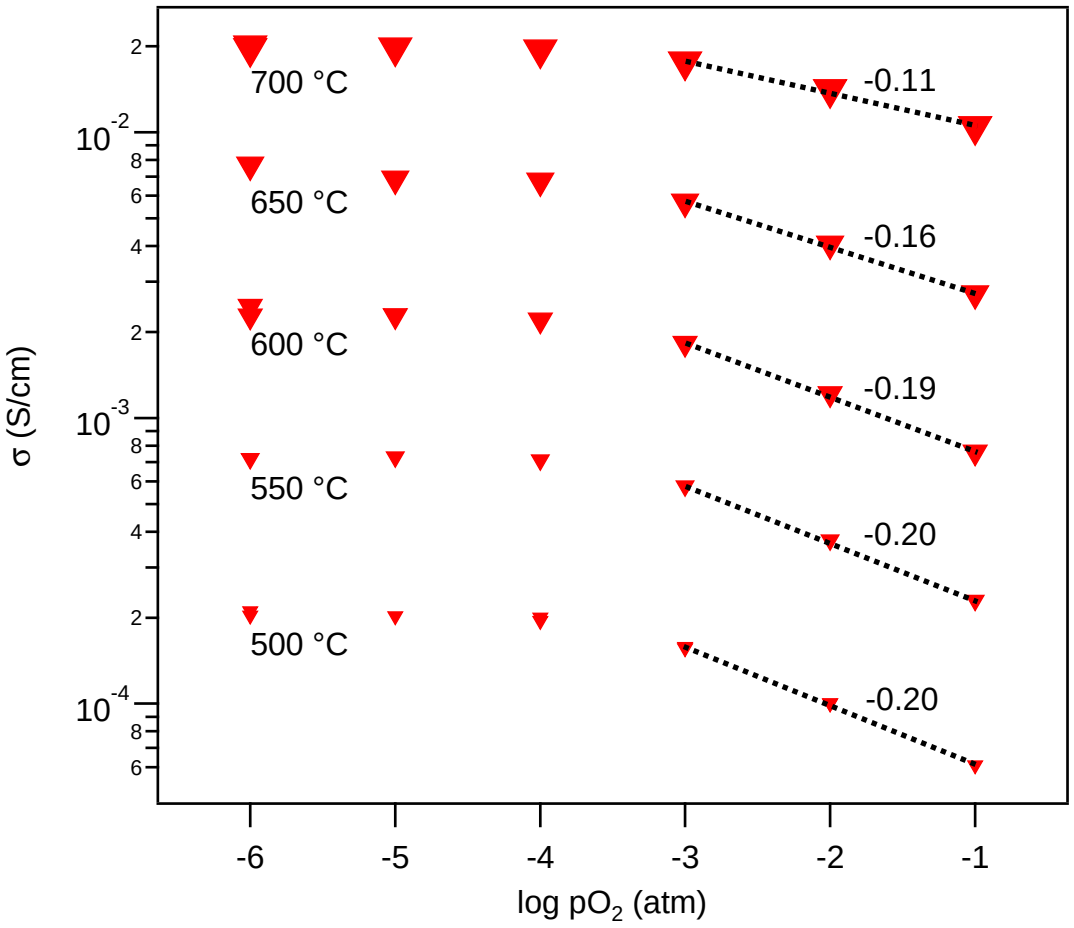

Fig. 6.6: Oxygen partial pressure dependence of the conductivity of a Nb-doped CeO_2 thin film.

conductivity is independent on the oxygen partial pressure, while at log $pO_2 \geq -3$ the conductivity decreases with oxygen pressure. For temperatures up to 600 °C a slope of −0.20 is measured for the pressure dependence of the conductivity. However, with increasing temperature the pO_2 dependence becomes less with a slope of only −0.11 at 700 °C. For comparison, the calculated conductivities from point defect calculations are shown in Fig. 6.7. In agreement with the measurements, a pO_2 independent region can be seen, where the electron concentration is determined by the donor concentration. At oxidizing conditions the conductivity decreases with a -1/4 slope. If the formation enthalpies, as introduced in section 3.4, are used for the calculation (red, dotted lines in Fig. 6.7), the transition to the pO_2 dependent region is at higher pressures. In this case, the conductivity should be oxygen pressure independent in the accessible pressure range for the experiment. As evident in Fig. 6.6, this is not the case.

Since the oxygen pressure dependence at higher pO_2 originates from donor compensation by doubly charged oxygen interstitials [26, 28] (cf. section 3.4), the pressure where this transition occurs is related to the defect formation enthalpies of the reduction reac-

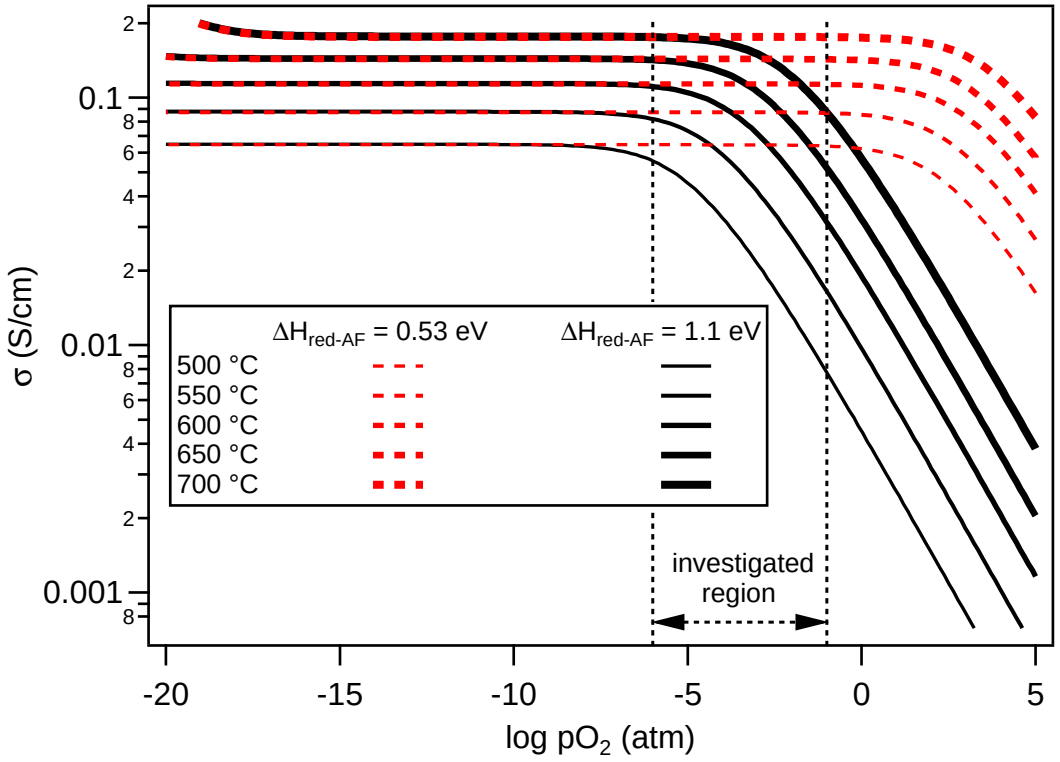

Fig. 6.7: Calculated conductivities of 1.3 cat.% Nb-doped CeO_2 in dependence of oxygen pressure and temperature for different $\Delta H_{red\text{-}AF} = \Delta H_{red} - \Delta H_{AF}$.

tion and the Anti-Frenkel defect pair. More precisely, it is determined by the difference between the Gibbs free energy of the reduction reaction (ΔG_{red}) and the Anti-Frenkel formation reaction (ΔG_{AF}) and thus, the difference of the formation enthalpies. The formation enthalpies introduced in section 3.4 result in a difference of the formation enthalpies of $\Delta H_{red\text{-}AF} = \Delta H_{red} - \Delta H_{AF} = 0.53$ eV. However, the calculated conductivities, using these values, do not reproduce the measured oxygen pressure dependence of the conductivity. By increasing this value to $\Delta H_{red\text{-}AF} = 1.1$ eV, the transition between pO_2 independent and dependent region in the Brouwer diagram shifts to the experimentally investigated region. Here, the increase of $\Delta H_{red\text{-}AF}$ was done by reducing the Anti-Frenkel formation enthalpy to $\Delta H_{AF} = 3.57$ eV. In this case, it is not crucial whether the increase of $\Delta H_{red\text{-}AF}$ is caused by an increase of ΔH_{red} or a decrease of ΔH_{AF}, since it does not change the outcome of the calculation.

The overall measured conductivities are significantly lower than the calculated values. While at 700 °C the experimental values are only lower by a factor of 8, the deviation at 500 °C is by a factor of 200. For a different sample (hw311a1), which was measured at temperatures from 400 to 500 °C, the difference between measurement and calculation is by a factor of 53 to 137 (see Figure 6.8). For a better comparability of the pO_2 dependence between calculated and experimental conductivities, the calculated conductivities in Fig. 6.8 are divided by these factors. At temperatures from 600

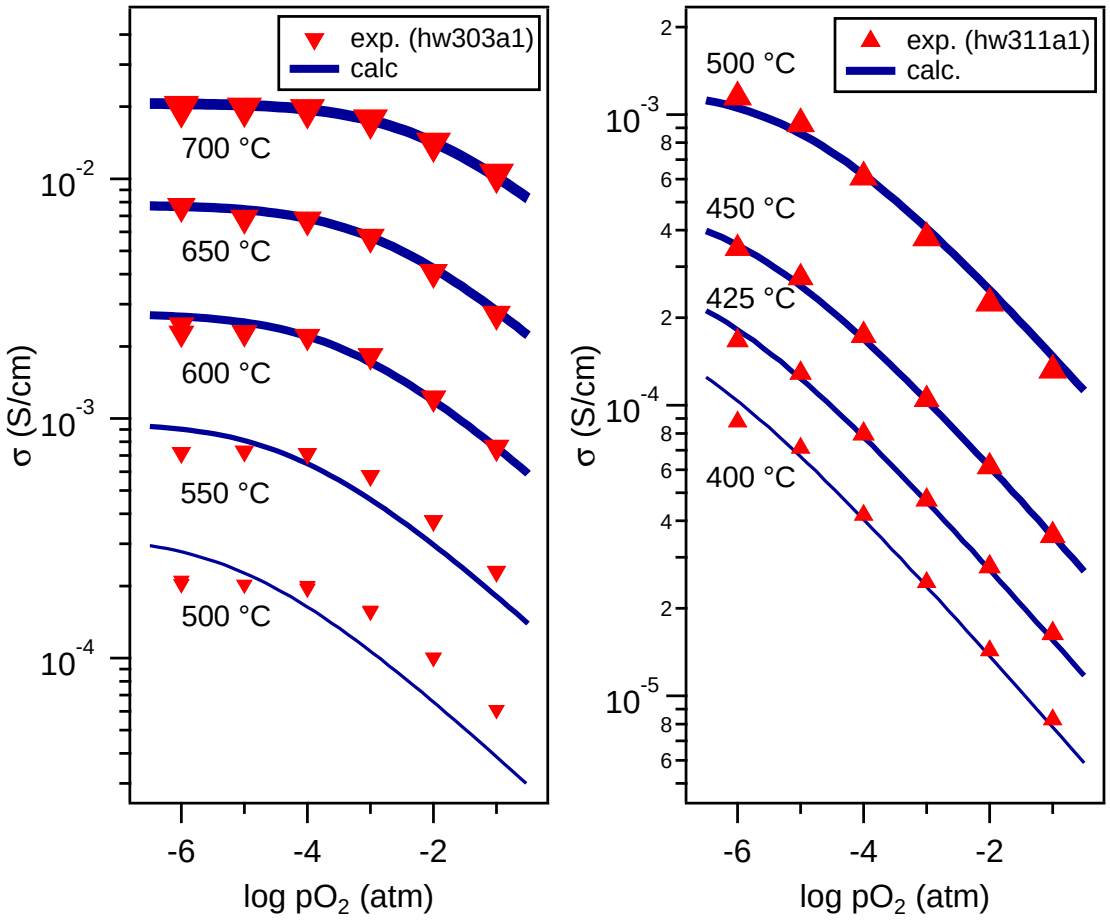

Fig. 6.8: Oxygen partial pressure dependence of the conductivity of two Nb-doped CeO_2 thin films deposited with the nominally the same parameters in comparison with calculated data using $\Delta H_{red\text{-}AF} = 1.1$ eV. The calculated data is divided by factors from 8 to 200 (left/hw303a1) and 53 to 137 (right/hw311a1) to fit the experimental data for better comparison of the pO_2 dependence.

to 700 °C the oxygen pressure dependence of the calculated conductivities is in good agreement with the experiment. At lower temperature the measured values deviate from the expected trend. However, for the other sample measured at temperatures $\leq$ 500 °C, the measured pO_2 dependence of the conductivity agrees well with the calculated trend. Overall, the employed defect model using a reduced Anti-Fenkel defect formation enthalpy of 3.57 eV reproduces the oxygen pressure dependence of the conductivity of Nb-doped CeO_2 thin films very well, although the absolute conductivities of the films are lower than expected and the experimental activation energy is significantly higher in this case.

In addition, the conductivities of the thin films are significantly lower than reported conductivities in literature for ceramic samples. De Guire *et al.* reported a conductivity of 0.25 S/cm for 0.8 cat.% Nb-doped CeO_2 at 700 °C [26], which agrees well with the calculated values (cf. Fig. 6.7). Göbel *et al.* reported conductivities for 2 mol% Nb-

doped CeO_2 thin films measured at 300 °C of 1×10^{-5} to 4×10^{-3} S/cm, depending on film morphology [28]. These values are of the same order as the conductivities presented in this work.

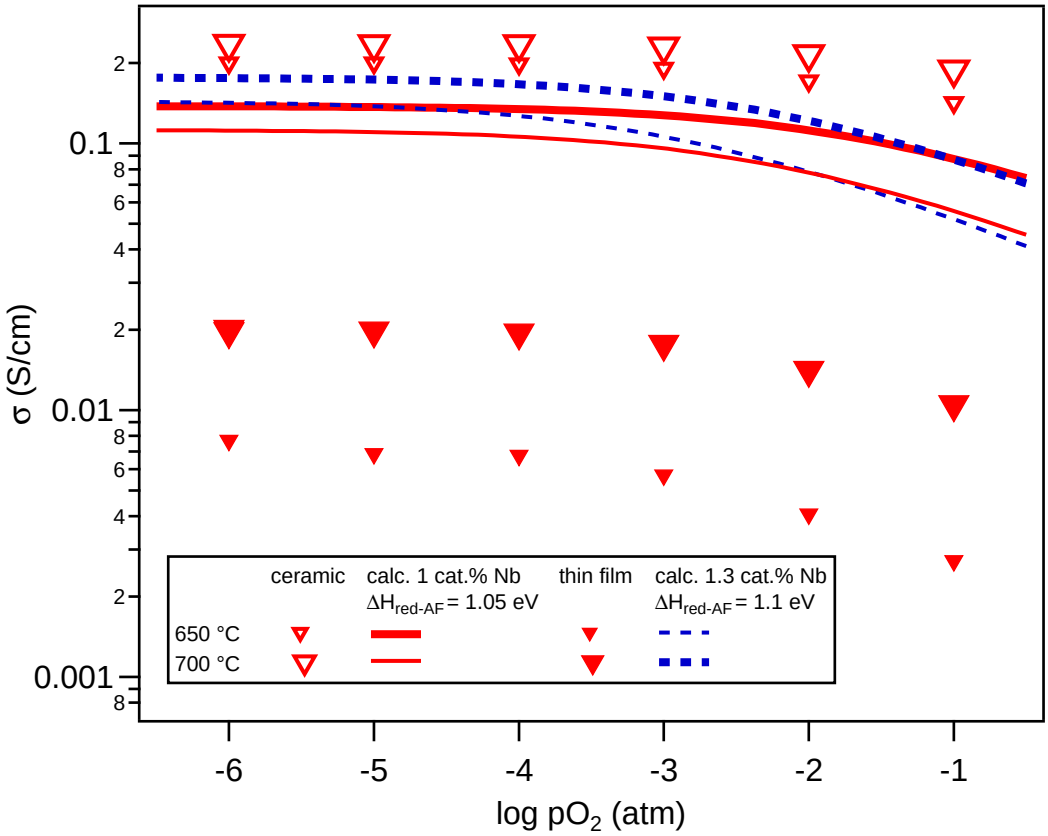

Fig. 6.9: Oxygen partial pressure dependence of the conductivity of 1.3 cat.% Nb-doped CeO_2 thin film (hw303a1) and 1 cat.% Nb-doped ceramic in comparison with calculated data.

The conductivity of a 1 cat.% Nb-doped CeO_2 ceramic, which was provided by Stephan Waldow from RWTH Aachen, is with ~ 0.2 S/cm at 700 °C in the same order of magnitude as the calculated conductivities. Fig. 6.9 shows the oxygen pressure dependence of the conductivity for the ceramic sample and a thin film in comparison to calculated values. The general pO_2 dependence of the ceramic sample is similar to the thin film. However, in order for the oxygen pressure dependence of the calculation to fit the experimental values of the ceramic, the Anti-Frenkel formation enthalpy has to be changed from 3.57 eV to $\Delta H_{AF} = 3.62$ eV, resulting in $\Delta H_{red\text{-}AF} = 1.05$ eV. This is slightly lower than the value of 1.1 eV, which reproduces the pO_2 dependence of the Nb-doped thin films. These necessary changes of the formation enthalpies to fit the experimental data might be related to the different doping level or strain within the thin films, which could have an influence on the formation enthalpies [152–154].

The origin of the differences in conductivity between the thin films and calculations is not known. One possible explanation could be a lower Nb concentration in the films than expected from the target composition. It is possible that the Nb is not incorporated efficiently in the CeO_2 lattice during sputtering, but segregates to grain boundaries and the surface, leaving the CeO_2 bulk mostly undoped. Such an effect has been found for sputtered Nb-doped $BaTiO_3$ thin films [155].
However, the pO_2 dependence of the conductivity fits very well. This makes it unlikely, that a lower Nb concentration is the main reason for the low conductivities of the thin films. In this context, it is interesting to consider the activation energies of the conductivities (see Fig. 6.10). The activation energy for the calculated conductivities is around 0.4 eV. This is expected, since the conductivity at log $pO_2 = -6$ was used. At this pO_2 the polaron concentration is given by the donor concentration and is mostly independent on the oxygen pressure. The resulting activation energies are thus determined by the polaron hopping process, which has an activation energy of 0.4 eV according to Tuller and Nowick [35], while Yashiro *et al.* [27] and Naik and Tien [156] reported a value of 0.29 eV. With $E_a = 0.28$ eV, the measured activation energy for the NDC ceramic fits well.

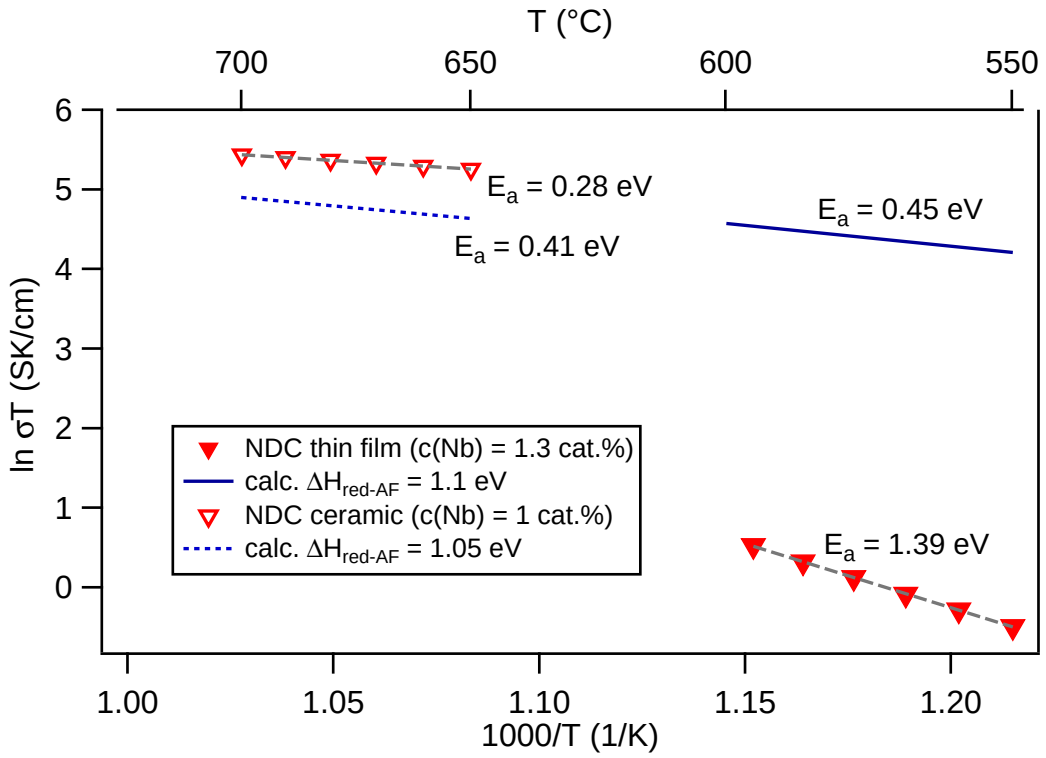

Fig. 6.10: Activation energies of the conductivity of 1.3 cat.% Nb-doped CeO_2 thin film (hw303a1) and 1 cat.% Nb-doped ceramic in comparison with calculated data. Data taken at log $pO_2 = -6$.

In contrast to this, the activation energy of the thin film is significantly higher with $E_a = 1.39$ eV. Since the pO_2 dependence agrees well with the calculation, the difference

of E_a is likely not related to the polaron concentration, but to a different carrier mobility in the thin films compared to the ideally calculated bulk. In Fig. 6.11, the "matching factors" (f_m) used to match the calculated conductivities to the experimental data in Fig. 6.8 are shown as an Arrhenius plot. A clear temperature dependence of f_m can be seen, which suggests an additional Boltzmann factor contributing to the carrier mobility. A possible origin for this additional temperature dependent factor might be the occurrence of depletion layers at grain boundaries, resulting in barriers for electron transport as shown schematically in Fig. 6.12. Such a model would fit previous reports of electronically blocking grain boundaries in Nb-doped ceria [28]. While for nominally undoped CeO_2, an electron accumulation is expected at grain boundaries [129, 130, 138, 151], the Nb-donor might lead to a different behavior. Due to Nb segregation to the grain boundary, additional grain boundary defect states might occur. Depending on the charge neutrality level of these states and the Fermi level position, these states might act as electron acceptors, which could result in a negative charge in the grain boundary core that would be compensated by an electron depletion close to the grain boundary. This depletion would translate into an upwards band bending at the grain boundaries, forming a barrier for electron transport. Such a phenomenon is known for oxide semiconductors such as doped In_2O_3, SnO_2 and ZnO [157–159].

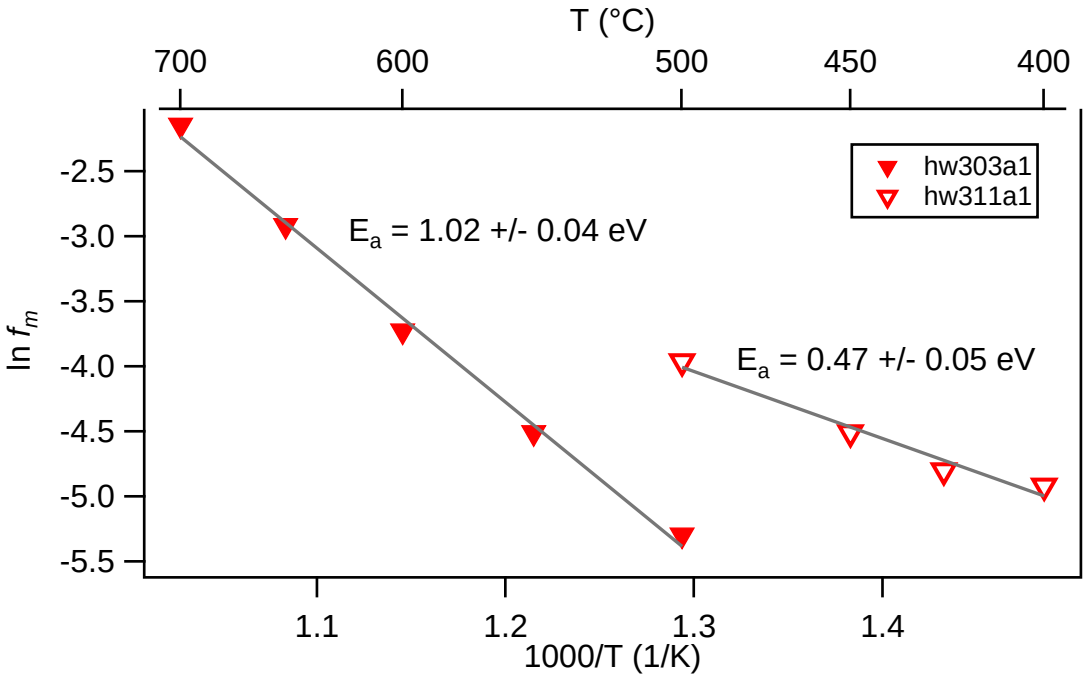

Fig. 6.11: Temperature dependence of the "matching factor" (f_m) of the conductivity of 1.3 cat.% Nb-doped CeO_2 thin films with the calculated values as used in Fig. 6.8.

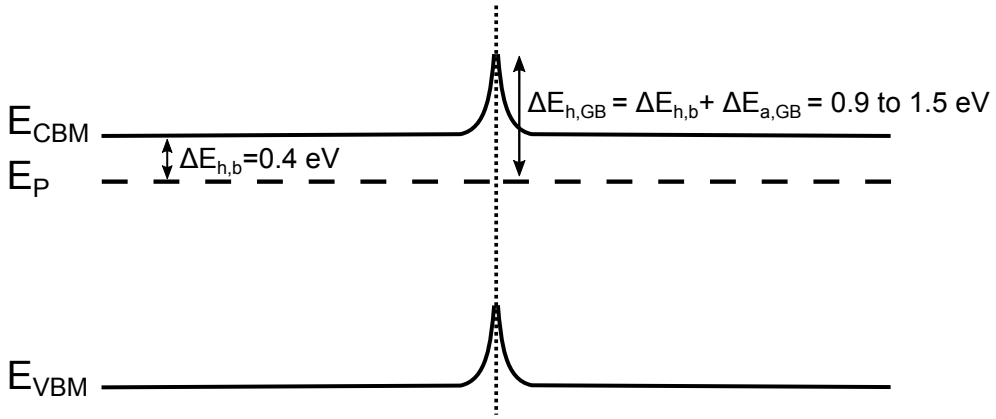

Fig. 6.12: Schematic band diagram with electronic energy barrier at grain boundaries. E_P is the polaron energy level, $\Delta E_{h,b}$ and $\Delta E_{h,GB}$ the activation energy for electron transport in the bulk and across grain boundaries, respectively, and $\Delta E_{a,GB}$ is the barrier height at the grain boundary.

Comparing the activation energy of f_m with $E_a = 1.02$ eV to the activation energies shown in Fig. 6.10, it is remarkable that the measured E_a of hw303a1 is close to the sum of the activation energy expected for the bulk material and f_m. This indicates that the calculated and measured conductivities are only different by an additional exponential factor which could come from grain boundary barriers and is thus not included in the calculations. It is further unclear where the differences in f_m between the two samples hw303a1 and hw311a1 come from, since both samples were deposited nominally under the same conditions. However, the samples were deposited over half a year apart. A possible explanation could be that the sample heater in the deposition chamber degraded during this time rendering the used temperature calibration of the heater inaccurate. Therefore, the actual substrate temperature during the deposition might be slightly different for the two samples, which could have an effect on the grain size and possible Nb segregation to the grain boundary.
It should be noted, that the electronic transport in the material should be very low with grain boundary barriers in the order of 1 eV. This contradicts the high conductivities measured for NDC films and could indicate that the transport across grain boundaries is not solely by thermal excitation, but could be by electron tunneling or thermally activated tunneling. The space charge layers are expected to be sufficiently narrow to enable tunneling.

6.1.3 Conductivity of Gd-doped CeO_2

Fig. 6.13 shows the oxygen pressure dependence of the conductivity of Gd-doped CeO_2 films in comparison to calculated conductivities. While the ionic conductivity could be neglected in comparison to the electronic conductivity for undoped and Nb-doped ce-

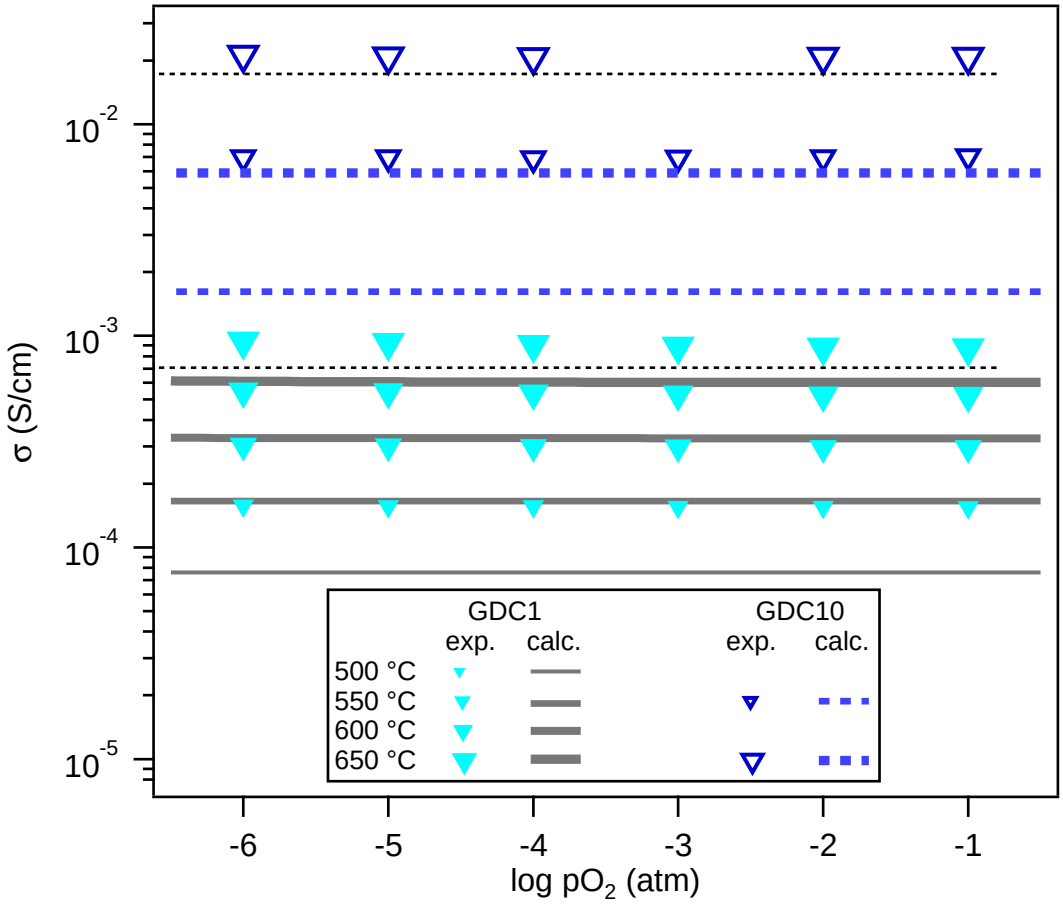

Fig. 6.13: Oxygen partial pressure dependence of the conductivity of 0.95 (GDC1) and 9.5 cat.% (GDC10) Gd-doped CeO_2 thin films in comparison to calculated conductivities. Dashed horizontal lines representing $pO_2{}^0$ dependence are included.

ria, it determines the overall conductivity for Gd-doped ceria in the investigated region ($-6 \leq \log pO_2 \leq -1$) by an oxygen vacancy mechanism. This can be seen in more detail in Fig. 6.14, where the ionic and overall conductivities are shown separately. At higher oxygen pressures, the conductivity is dominated by the ionic conductivity, which is pO_2 independent because the oxygen vacancy concentration in this region is defined by the acceptor concentration. Only at reducing conditions, the amount of $V_O^{\bullet\bullet}$ from thermal reduction becomes significant. This causes, besides a slight increase of the ionic conductivity, the electronic conductivity to dominate the overall conductivity.

For the strongly doped GDC10 the transition from ionic to electronic conductivity occurs at lower oxygen pressures than for GDC1 with a lower doping concentration. This results in a pO_2 independent behavior for GDC10 within the investigated region as observed experimentally (see Fig. 6.13). The transition to the intrinsic region for GDC1 is closer to the investigated region, which can be observed as well in the experiment. There, a very low oxygen pressure dependence of the conductivity for GDC1 at higher temperatures is

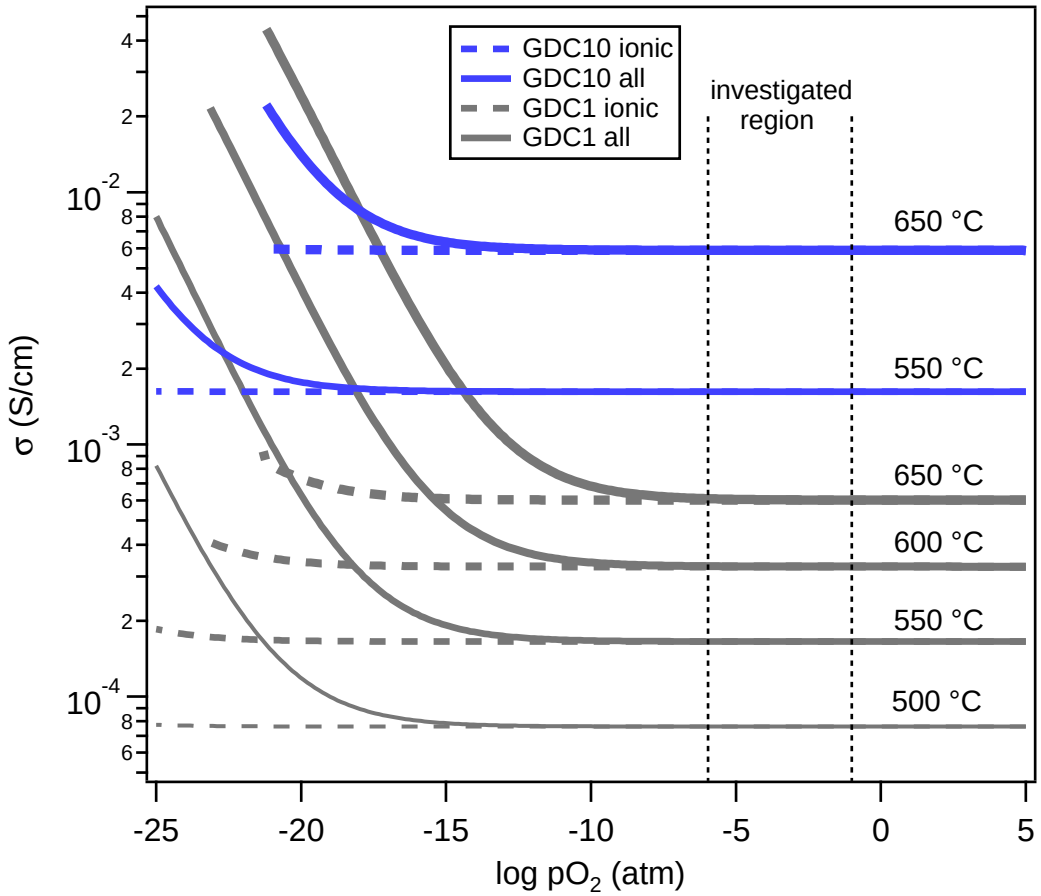

Fig. 6.14: Calculated Brouwer diagram for Gd-doped CeO_2 with 0.95 (GDC1) and 9.5 cat.% (GDC10) Gd-doping.

confirmed. However, since the electronic contribution is still small compared to the ionic conductivity, the measured pO_2 dependence is not very pronounced.

With a conductivity of $\sim 2 \times 10^{-2}$ S/cm at 650 °C for GDC10 the measured values are in good agreement with previously reported Gd-doped CeO_2 films with high doping concentrations deposited by pulsed laser deposition (PLD) on sapphire substrates. Joo *et al.* reported for 20 cat.% Gd-doping at 650 °C a conductivity of $\sim 1.3 \times 10^{-2}$ S/cm [61], while Goebel *et al.* obtained a conductivity of $3.3 - 4.1 \times 10^{-2}$ S/cm, depending on film thickness, for 10 cat.% doped films at 700 °C [69]. From this it can be concluded, that sputtered GDC films have similar conductivities as films deposited by PLD.

In general, there is a reasonable agreement between calculated and measured data (see Fig. 6.13), although the calculated conductivities are lower by a factor of $2 - 4$. These variations might come from grain boundary effects, since the conductivity, especially the grain boundary conductivity, of Gd-doped ceria depends on the grain size [62, 66]. Suzuki *et al.* reported an increasing conductivity with decreasing grain size with a difference in conductivity of nearly a factor of 10 for 20 cat.% Gd-doped CeO_2 films when the average grain size is varied from 11 to 36 nm [62]. Typically the ionic conductivity

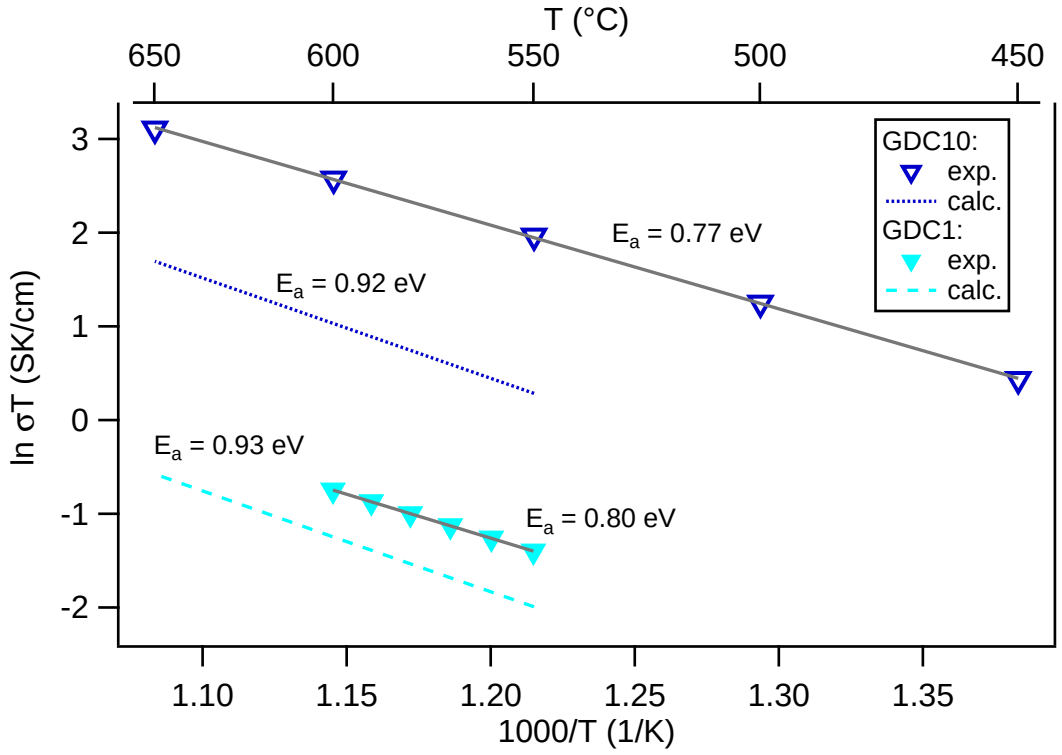

Fig. 6.15: Temperature dependence of conductivity for Gd-doped CeO_2 films with 0.95 (GDC1) and 9.5 cat.% (GDC10) Gd-doping in comparison to calculated data.

in GDC is reduced by grain boundaries. Due to a depletion of oxygen vacancies in the proximity of the grain boundary, oxygen transport is hindered perpendicular to grain boundaries [68, 71, 160, 161]. On the other hand, the high vacancy concentration in the grain boundary core enhances oxygen diffusion along the grain boundary in addition to an increased electronic conductivity caused by an electron accumulation [160–162]. For small grain sizes, the parallel grain boundary conductivity could become significant, compared to the blocking effect for the perpendicular transport, due the high amount of parallel grain boundaries. This could explain the higher experimental conductivities compared to the calculated data.

However, if the activation energies for the conductivity are taken into account (see Fig. 6.15), it seems more likely that the difference between experiment and calculation is mostly related to the different activation energies. The experimental activation energies for GDC1 and GDC10 films are around 0.8 eV which is a typical value for an ionic conducitivity via an oxygen vacancy mechanism. In literature activation energies for GDC thin films and bulk samples ranging from 0.7 to 0.9 eV are reported [61, 66, 69, 144], which is in good agreement with the experimental data from this work.

Since the activation energy was determined with the conductivity from a pO_2 regime, where the oxygen vacancy concentration is mostly given by the acceptor concentration, the calculated activation energy is defined by the migration enthalpy of the oxygen va-

cancy used for the calculation. The used value of $\Delta H_{mig} = 0.92$ eV [65] might be too high, which would explain why the calculated conductivities are too low.

6.2 Exchange kinetics and diffusivity of CeO_2

In the previous section, the equilibrium conductivities at different temperatures and oxygen partial pressures of nominally undoped and doped ceria films were investigated. In this section, the kinetics of the stoichiometry changes will be addressed. From this the oxygen exchange coefficient (k_{chem}) at the surface and the diffusivity (D_{chem}) of the films will be evaluated as described in section 3.3.

Unfortunately, a reliable determination of k_{chem} and D_{chem} from conductivity relaxation measurements was only possible for the undoped and Nb-doped films. As shown in the previous section, GDC10 samples show no change in conductivity when pO_2 is changed. While GDC1 films have a marginal oxygen pressure dependence of the conductivity within the investigated pO_2 range, it is only pronounced at higher temperatures. However, the relaxation time of the sample at high temperatures is only a few minutes, which is the same time scale as the gas exchange in the relaxation oven. Therefore, the exchange coefficient and diffusivity of Gd-doped films could not be determined exactly. Since it is not clear, if the relaxation time of GDC films is determined by the gas exchange in the oven or at the sample itself, only a lower limit for the exchange coefficient can be estimated from the relaxation time τ_k with Eq. 6.1 [163].

$$k_{chem} = \frac{5d}{2\tau_k} \tag{6.1}$$

The conductivity relaxation profiles and fits are shown in Fig. 6.16. In Table 6.1 the measurement parameters of the corresponding profiles are listed together with the values for k_{chem} and D_{chem} as obtained for the fit. For NDC samples, especially ceramics, good profile fits were obtained using equation 3.2. However, for the NDC thin films, the profile could not be reproduced very well at $pO_2 \geq 10^{-2}$ atm (profile 15 and 16). In addition, the measurements at 500 °C for undoped ceria (profiles 1-3) could only be fitted partially. The reason why the thin films cannot be fitted as well as the ceramics could be related to additional diffusion processes in the thin films. Due to the much smaller grain size of the thin films (~ 50 nm) compared to the ceramic sample ($\sim 1-10$ μm) it is likely that the diffusion along the grain boundary plays an important role for the thin films, while it can be mostly neglected for the ceramic.

The parameter $\frac{lk_{chem}}{D_{chem}}$ in Table 6.1 is a measure whether the oxygen exchange is limited by diffusion or by the surface exchange. As a rule of thumb, D and k can both be

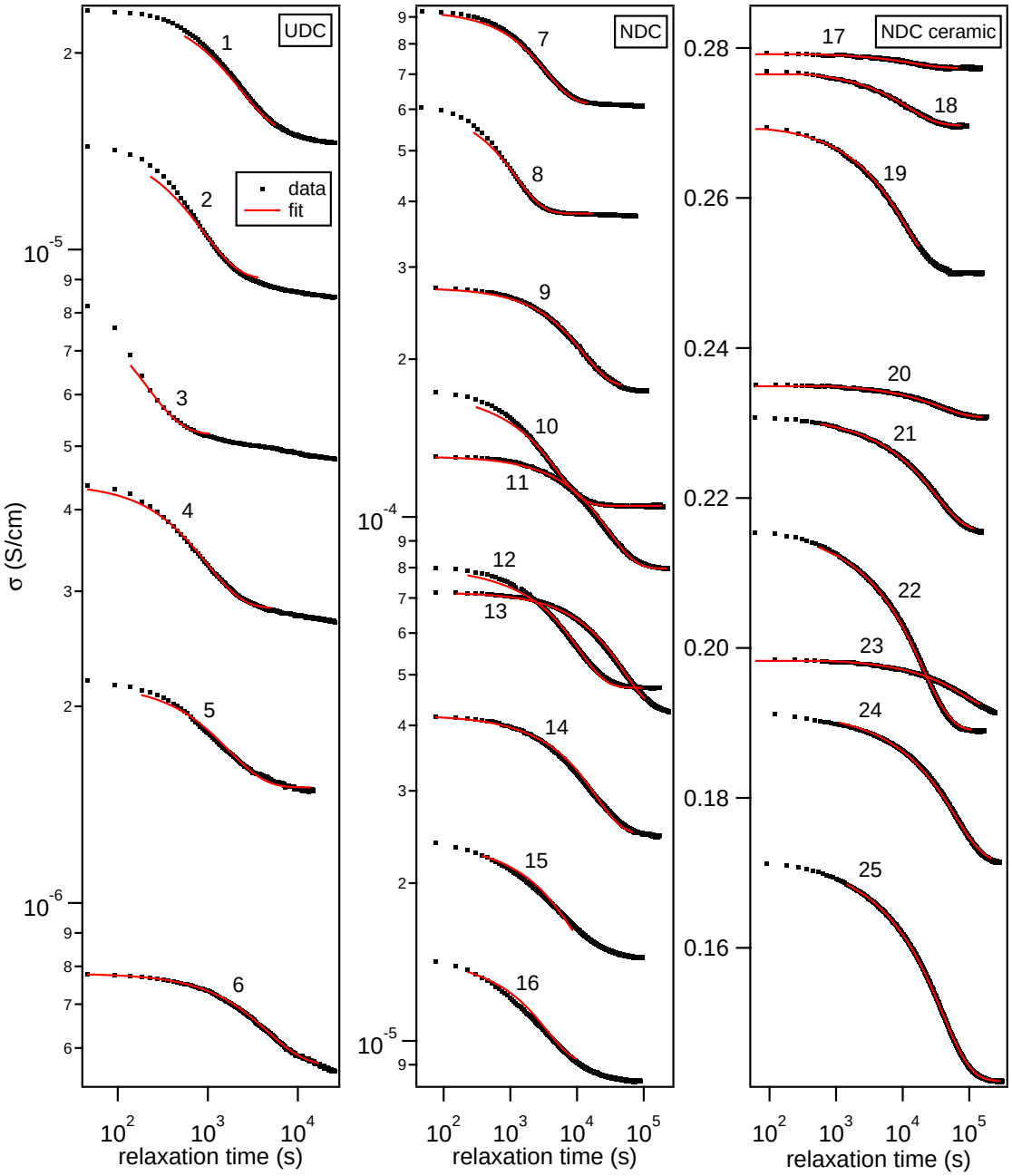

Fig. 6.16: Conductivity relaxation profiles with corresponding fits for undoped CeO_2 film and Nb-doped CeO_2 film and ceramic. The measurement parameters for each profile are given in Table 6.1.

Table 6.1: Measurement parameters for conductivity profiles shown in Fig. 6.16 with fitted D_{chem} and k_{chem} values. Error for D_{chem} and k_{chem} is below 10 % for undoped and below 5 % for Nb-doped CeO_2. Values for Gd-doped films are estimated from Eq. 6.1 and constitute only the lower limit of k_{chem}.

	Profile	T_{ex} (°C)	$pO_{2,in}$ (atm)	$pO_{2,\infty}$ (atm)	D_{chem} (m^2/s)	k_{chem} (m/s)	$\frac{lk_{chem}}{D_{chem}}$
undoped thin film	1	500	10^{-5}	10^{-4}	7.1×10^{-15}	4.6×10^{-10}	0.06
	2	500	10^{-4}	10^{-3}	1.7×10^{-15}	2.6×10^{-9}	1.38
	3	500	10^{-3}	10^{-2}	5.8×10^{-15}	6.9×10^{-9}	1.07
	4	475	10^{-4}	10^{-3}		1.1×10^{-9}	
	5	450	10^{-4}	10^{-3}		6.1×10^{-9}	
	6	425	10^{-4}	10^{-3}		2.5×10^{-10}	
Nb-doped thin film	7	500	10^{-5}	10^{-4}	5.1×10^{-17}	3.0×10^{-10}	2.65
	8	500	10^{-4}	10^{-3}	1.2×10^{-16}	1.1×10^{-9}	4.13
	9	450	10^{-5}	10^{-4}	1.2×10^{-17}	1.0×10^{-10}	3.75
	10	450	10^{-4}	10^{-3}	2.1×10^{-17}	1.7×10^{-9}	36.43
	11	425	10^{-5}	10^{-4}	4.6×10^{-18}	5.4×10^{-11}	5.28
	12	425	10^{-4}	10^{-3}	1.0×10^{-17}	5.0×10^{-10}	22.50
	13	400	10^{-5}	10^{-4}	2.7×10^{-18}	3.3×10^{-11}	5.50
	14	400	10^{-4}	10^{-3}	6.2×10^{-18}	1.4×10^{-10}	10.16
	15	400	10^{-3}	10^{-2}			
	16	400	10^{-2}	10^{-1}			
Nb-doped ceramic	17	750	10^{-4}	10^{-3}	1.6×10^{-12}	7.6×10^{-8}	11.40
	18	750	10^{-3}	10^{-2}	2.0×10^{-12}	7.9×10^{-8}	9.48
	19	750	10^{-2}	10^{-1}	2.2×10^{-12}	8.9×10^{-8}	9.71
	20	700	10^{-4}	10^{-3}	6.5×10^{-13}	2.9×10^{-8}	10.71
	21	700	10^{-3}	10^{-2}	3.8×10^{-13}	4.6×10^{-8}	29.05
	22	700	10^{-2}	10^{-1}	1.1×10^{-12}	7.3×10^{-8}	15.93
	23	650	10^{-4}	10^{-3}	2.8×10^{-13}	1.3×10^{-8}	11.14
	24	650	10^{-3}	10^{-2}	3.5×10^{-13}	3.2×10^{-8}	21.94
	25	650	10^{-2}	10^{-1}	5.6×10^{-13}	4.5×10^{-8}	19.29
0.95 cat.% Gd-doped thin film		650	10^{-6}	10^{-5}		$> 7.2 \times 10^{-9}$	
		650	10^{-5}	10^{-4}		$> 3.8 \times 10^{-9}$	
		650	10^{-4}	10^{-3}		$> 4.6 \times 10^{-9}$	
		650	10^{-3}	10^{-2}		$> 1.6 \times 10^{-8}$	
		600	10^{-6}	10^{-5}		$> 5.3 \times 10^{-9}$	
		600	10^{-5}	10^{-4}		$> 5.9 \times 10^{-9}$	
		600	10^{-4}	10^{-3}		$> 2.5 \times 10^{-9}$	
		600	10^{-3}	10^{-2}		$> 3.5 \times 10^{-9}$	
		550	10^{-6}	10^{-5}		$> 6.4 \times 10^{-9}$	
		550	10^{-5}	10^{-4}		$> 8.0 \times 10^{-9}$	

determined from conductivity relaxation measurements if $0.06 \geq \frac{lk_{chem}}{D_{chem}} \geq 30$ [164]. The obtained values fulfill this condition. If $\frac{lk_{chem}}{D_{chem}}$ is significantly smaller or higher than that, the exchange process is determined by the surface exchange or diffusivity, respectively.

For UDC films measured below 500 °C, the diffusion coefficient used for the fit could be increased several orders of magnitude without any influence on the shape of the fit. This means that the the oxygen exchange is determined by k. Since D could be chosen arbitrarily, a defined value for the diffusivity could not be obtained for UDC samples for $T_{ex} < 500$ °C.

The values for the lower limit of k_{chem} for GDC1 estimated with Eq. 6.1 are generally of reasonable order of magnitude. However, the data do not show a reasonable trend with temperature and scatter significantly, which indicates that the values do not represent the sample, but are more a measure of the gas exchange time in the oven. For this reason they will not be considered in further discussions.

Since the conductivity of the GDC films is mostly ionic and the electronic part negligible, the diffusivity can be calculated using the Nernst-Einstein equation (Eq. 3.14). The obtained values for different temperatures are summarized in table 6.2. In order to obtain D_{chem}, the oxygen vacancy concentration needs to be known. Therefore, the equilibrium conductivity at $pO_2 = 0.1$ atm was used to ensure that the $V_O^{\bullet\bullet}$ concentration is determined solely by the Gd acceptor concentration (cf. Fig. 6.14). Assuming that two acceptors are always compensated by one oxygen vacancy the resulting $V_O^{\bullet\bullet}$ concentrations used for the calculation are 1.21×10^{21} cm^{-3} and 1.21×10^{20} cm^{-3} for GDC10 and GDC1, respectively.

Table 6.2: Diffusion coefficients of Gd-doped CeO_2 thin films calculated from conductivity data at $pO_2 = 0.1$ atm using the Nernst-Einstein relation (Eq. 3.14).

	T (°C)	D_{chem} (m^2/s)
9.5 cat.% Gd-doped	550	6.42×10^{-11}
	650	2.13×10^{-10}
0.95 cat.% Gd-doped	500	1.33×10^{-11}
	550	2.69×10^{-11}
	600	5.06×10^{-11}
	650	8.97×10^{-11}

The presented results for the exchange kinetics and diffusivity from conductivity relaxation measurements will be discussed together with results from isotope exchange exchange experiments in chapter 8.

7 Secondary ion mass spectrometry of ^{18}O exchange profiles

A common method to obtain exchange and diffusion coefficients of a material is by isotope exchange experiments combined with secondary ion mass spectrometry (SIMS). For this, the samples are annealed in defined thermodynamic conditions, i.e. exchange temperature (T_{ex}) and oxygen pressure ($pO_{2,ex}$), in an isotope enriched gas atmosphere. After annealing for a certain exchange time, the samples are quenched and the resulting isotope profiles can be probed by SIMS. All following results were obtained after an exchange time of 30 min. In principle, by fitting the measured ^{18}O-exchange profile with a suitable model, the tracer diffusion (D^*) and exchange (k^*) coefficient can be determined. The first approach was to fit the profile with the equation by Crank [93] for a semi-infinite medium:

$$n_r(x,t) = \mathrm{erfc}\left[\frac{x}{2\sqrt{D^*t}}\right] - \left[\exp\left(\frac{k^*x}{D^*} + \frac{k^*2t}{D^*}\right) \times \mathrm{erfc}\left(\frac{x}{2\sqrt{D^*t}} + k^*\sqrt{\frac{t}{D^*}}\right)\right] \tag{7.1}$$

with

$$n_r(x,t) = \frac{c(x,t) - c_{bg}}{c_g - c_{bg}} \tag{7.2}$$

where $c(x,t) = I(^{18}O)/(I(^{18}O) + I(^{16}O))$ is the ^{18}O isotope fraction, c_{bg} the ^{18}O background fraction and $c_g = 0.765$ the isotope fraction in the exchange gas. While this model has been reported to be successful, e.g. for $La_{0.8}Sr_{0.2}MnO_3$ [165], it could not be used here. In Fig. 7.1 the ^{18}O-exchange profile for a 0.95 cat.% Gd-doped CeO_2 thin film fitted with Eq. 7.1 is displayed. While the fit looks well for the bulk of the material, it does not reproduce the first 10 *nm* of the profile. Since this part is especially important for the determination of k^*, this simple approch based on Eq. 7.1 is not sufficient. A reason for this is likely the occurrence of a surface space-charge layer where an accumulation of oxygen vacancies at the surface leads to a strong decrease of the $V_O^{\bullet\bullet}$ concentration in the near surface region, which results in a barrier for oxygen transport [132, 166]. In order to solve this problem and obtain k^* and D^* from the ^{18}O exchange profile, first the defect concentration profiles in the space-charge zone need to be calcu-

lated by solving Poisson's equation. In a second step, the tracer diffusion problem has to be solved including the obtained information about the defect concentration profiles in the space-charge zone. The details about this procedure are outlined in [166]. The results are shown exemplarily in Fig. 7.2 for a NDC and GDC1 thin film. Both fits were performed by S. P. Waldow at RWTH Aachen and are shown here with his permission.

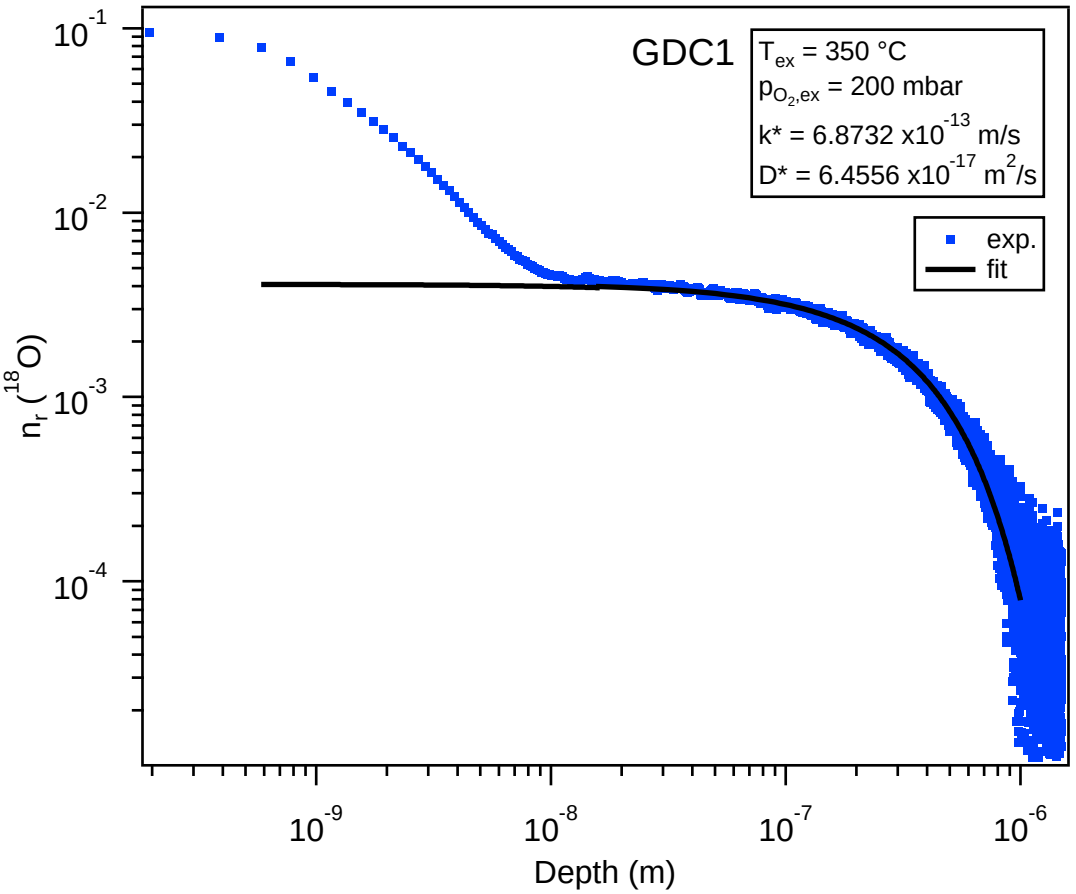

Fig. 7.1: ^{18}O-exchange profile for 0.95 cat.% Gd-doped ceria thin film after an exchange time of 30 min fitted with Eq. 7.1.

The fits from this procedure show a good agreement with the measured profile from a depth of 2 nm on. Further experimental results as well as a more detailed description of the ^{18}O exchange experiments and fitting of the SIMS profiles will be available within the work of our project partners from RWTH Aachen, R. A. De Souza and S. P. Waldow.

7.1 Surface modification of CeO_2 by In_2O_3:Sn surface layer

An In_2O_3:Sn (ITO) surface layer was investigated as a possible way to increase the oxygen exchange of doped and undoped ceria. ITO has a pronounced oxygen exchange and oxygen diffusivity at temperature above 300 °C [91, 167–169]. A NDC and GDC1 film was thus sputtercoated with a 3 nm thick ITO film and isotope exchange experiments

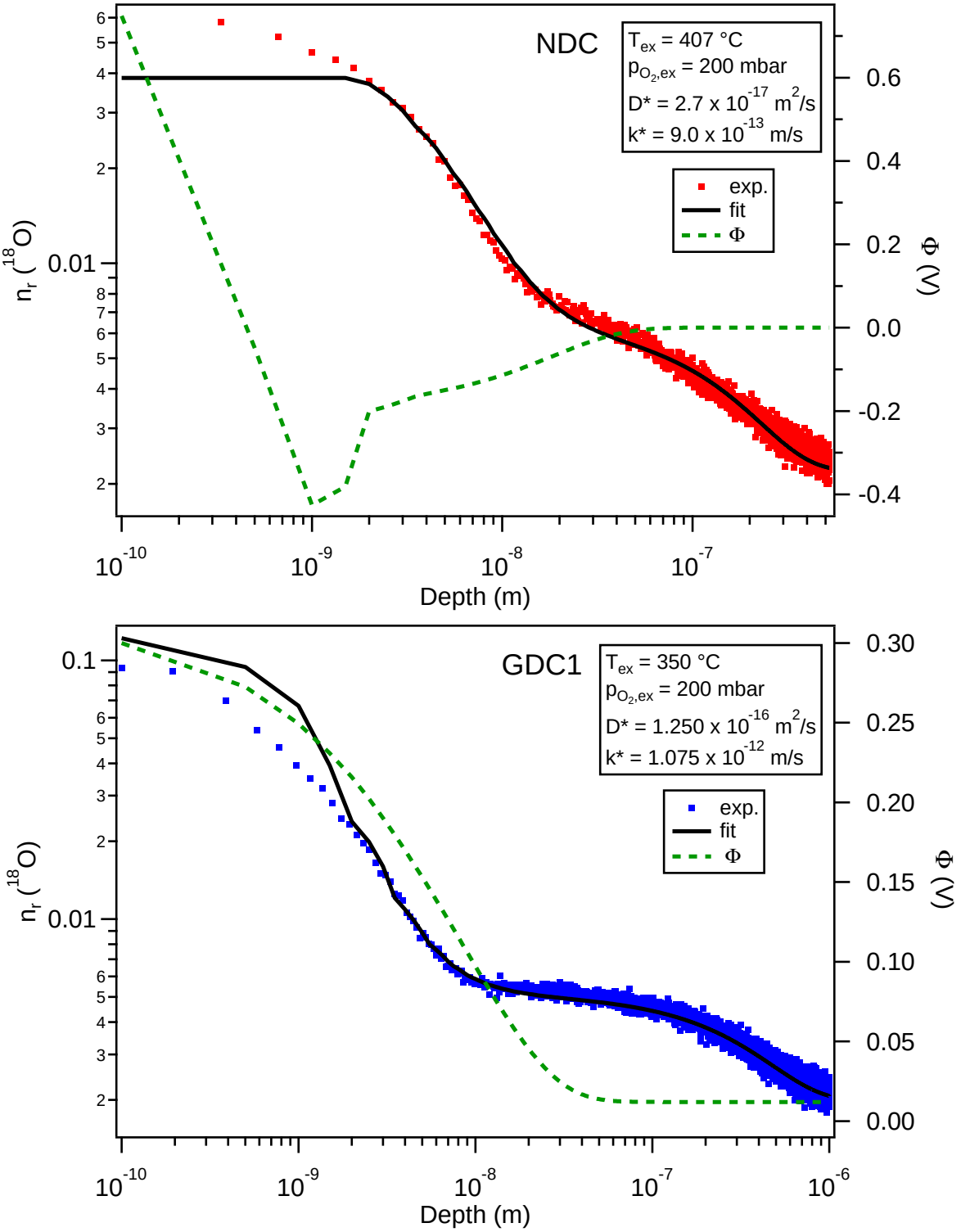

Fig. 7.2: ^{18}O-exchange profiles with fitted profile and electrostatic potential (Φ) for 1.3 cat.% Nb-doped (top) and 0.95 cat.% Gd-doped (bottom) ceria thin films after an exchange time of 30 min.

were conducted with bare and ITO covered NDC and GDC films under the same conditions. The resulting SIMS profiles are shown in Fig. 7.3. For both, NDC and GDC1, a significant difference in the ^{18}O-profiles can be seen between the bare films and ITO covered films. Contrary to the expected result, the profile for the samples with ITO top layer are significantly shorter and reach the ^{18}O-background concentration in a depth of around 20 nm, while the uncovered samples have extended profiles with depths of up 700 nm. Close to the surface, mostly within the ITO layer, the ^{18}O-concentration is significantly higher than in the uncovered films, which confirms the high exchange and diffusivity of ITO. However, the ^{18}O-concentration decreases strongly in the proximity of the ITO/CeO_2 interface.

To obtain more information about this effect, an interface experiment was performed with XPS. For this, ITO was deposited stepwise on a (111) oriented undoped CeO_2 film. XPS measurements of the clean UDC film and after each deposition step of ITO were executed. Since the valence band spectra of CeO_2 and ITO overlap, it is difficult to follow the Fermi level position shift from the valence band spectra. In order to still get information about a possible band bending in ceria at the ITO interface, the binding energy difference between the valence band and core levels are determined from the clean substrate film. Under the assumption that this binding energy difference stays constant, which is valid as long there are no major chemical shifts, the Fermi level position shift at the interface can be obtained by following the binding energy shift of the Ce3d emission line with increasing ITO film thickness. In order to avoid binding energy shifts from a change in oxidation state from Ce^{4+} to Ce^{3+}, the peak at $\sim$ 916.8 eV (Ce3d v''') was used to determine the shift in E_B, because this peak originates only from Ce^{4+} with no overlap from Ce^{3+} related emission lines (cf. section 3.2.1). A detailed description of the used procedure for XPS interface experiments can be found in references [75, 170].

The shift of the Fermi level position in UDC with ITO deposition time is shown in Fig. 7.4. An increase of BE_{VBM} of 0.2 eV with increasing deposition time can be seen, which corresponds to a downwards band bending at the interface, i.e. an electron accumulation layer (see Fig. 7.5). This is also confirmed by the increase of the Ce^{3+} concentration. For ITO, no significant band bending could be measured, which is likely due to the significantly higher electron density in ITO (n(ITO)$\sim 10^{20}$ cm^{-3}), which would cause a very narrow space charge region. In addition, a determination of the band banding in the film, that is deposited, is complicated since the electronic structure might not have developed fully if the film thickness is still only a few monolayers or less. This is the reason why the band banding can be probed typically better in the substrate layer.

With the information from the interface experiment, the decreased oxygen exchange into the ITO covered ceria films can be explained. From literature, a high oxygen vacancy con-

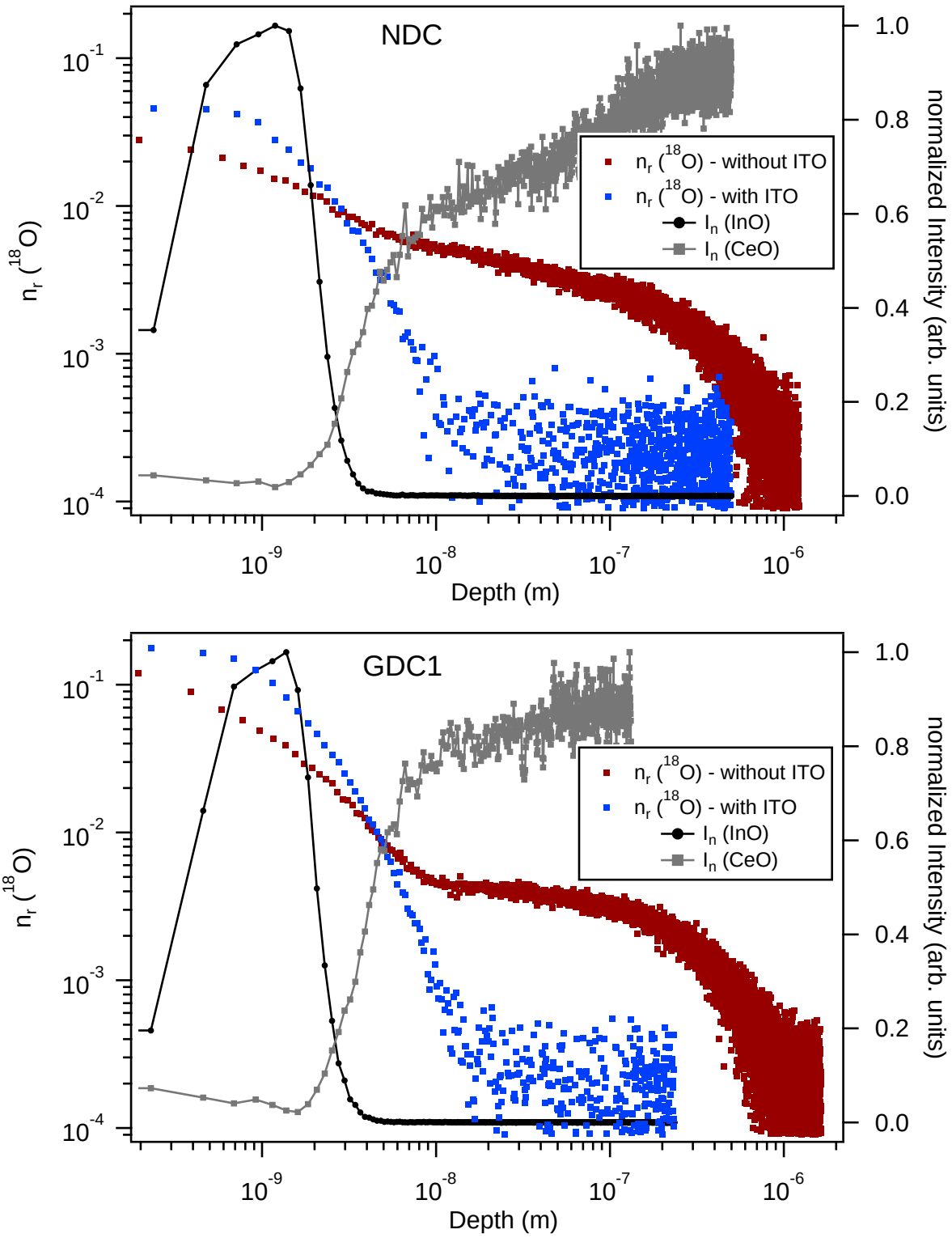

Fig. 7.3: ^{18}O-exchange profile for 1.3 cat.% Nb-doped (top) and 0.95 cat.% Gd-doped (bottom) ceria thin films with and without 3 nm thick In_2O_3:Sn (ITO) top layer after an exchange time of 30 min at 350 °C. In addition, the normalized intensities of the InO^- and CeO^- species are shown.

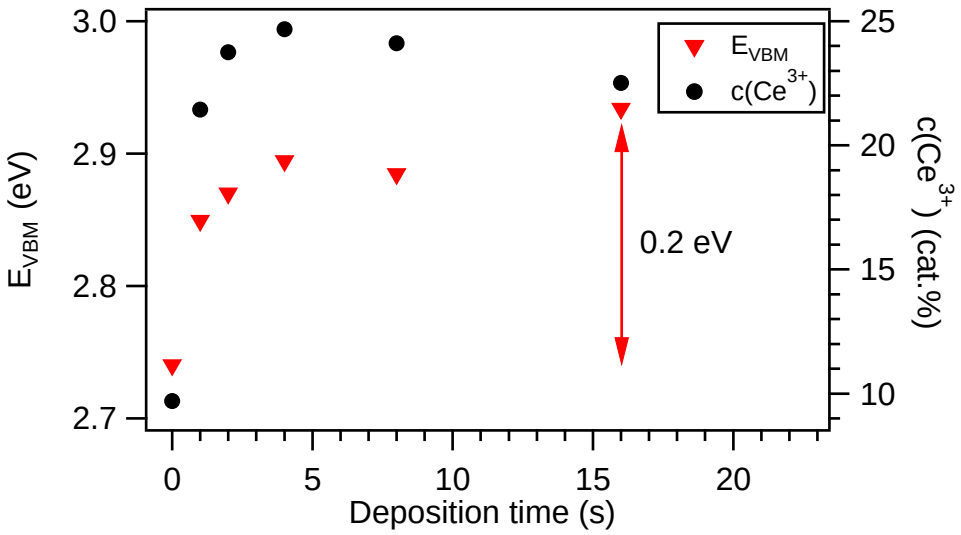

Fig. 7.4: Fermi level position shift of undoped CeO_2 at the CeO_2 /In_2O_3:Sn (ITO) interface and Ce^{3+} concentration with increasing ITO deposition time.

centration is expected to be at the surface and in grain boundary cores. The associated charges are typically compensated by electron polaron accumulation and, in case of acceptor doped ceria, partly by acceptor accumulation at the surface and grain boundary [69, 132, 171]. As a consequence of the increased $V_O^{\bullet\bullet}$ and acceptor concentration at the surface and grain boundaries, the oxygen vacancy concentration close to these interfaces is depleted, which results in an increased oxygen transport resistance perpendicular to the surface and grain boundaries. In analogy to this, the electron accumulation in ceria at the CeO_2/ITO-interface will likely increase $V_O^{\bullet\bullet}$ segregation to the interface and thus also enhance the oxygen vacancy depletion zone, which is hindering oxygen transport in the material.

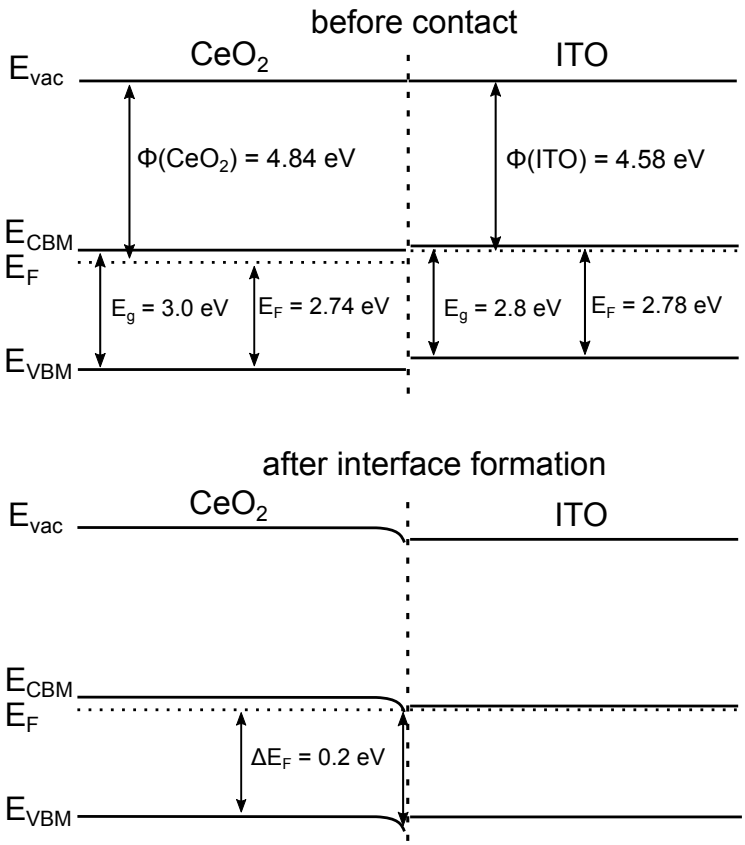

Fig. 7.5: Band diagram of the CeO_2-ITO interface before and after contact formation.

8 Surface exchange and diffusivity of doped and undoped CeO_2

In this chapter the exchange coefficients and diffusivity for differently doped ceria obtained from conductivity relaxation measurements as described in section 6.2 are discussed and compared with literature results.

8.1 Exchange coefficient and diffusivity

In Fig. 8.1, the chemical exchange and diffusion coefficients for undoped und Nb-doped CeO_2 are shown in dependence of temperature. The dotted black line is inserted as an interpolation between data from ceramic and thin film samples for comparison. The extrapolated diffusivities for the ceramic NDC samples are higher compared to the diffusivities of the NDC thin films, although the activation energies are similar.
Within the error of the measurement, k_{chem} of the ceramic NDC is comparable to the NDC thin film. However, the activation energy of the exchange coefficient scatters significantly for the ceramic samples from approximately 0.6 to 1.5 eV, while k_{chem} is around 1 eV for the thin film. The exchange coefficients and the corresponding activation energy of 1.15 eV for UDC are comparable to the NDC thin films within the error margin. It should be noted that in further studies of the ceramic NDC samples an enrichment of SiO_2 was found at the surface with XPS and SIMS [96]. The determined exchange coefficients for the ceramic samples should thus be considered with caution, since the surface exchange might be determined by a SiO_2 surface layer. Nevertheless, due to the reasonable values compared to the thin film results, the effect of a possible SiO_2 surface layer will be neglected in the following discussion.

Despite the temperature dependence of k_{chem} and D_{chem}, a significant effect of the oxygen pressure is observed. This is shown in more detail in Fig. 8.2. With the exception of D_{chem} of UDC, an increase in oxygen exchange and diffusivity is observed with increasing pO_2 for NDC and UDC. The effect on D_{chem} can be explained by the defect chemistry of the material since the diffusivity depends on the defect concentration and underlying transport mechanism. Oygen transport in Nb-doped ceria is expected via oxygen interstitials. From the defect model for the NDC thin films and ceramics at different temperatures the oxygen interstitial concentration has an expected oxygen pressure dependence ranging

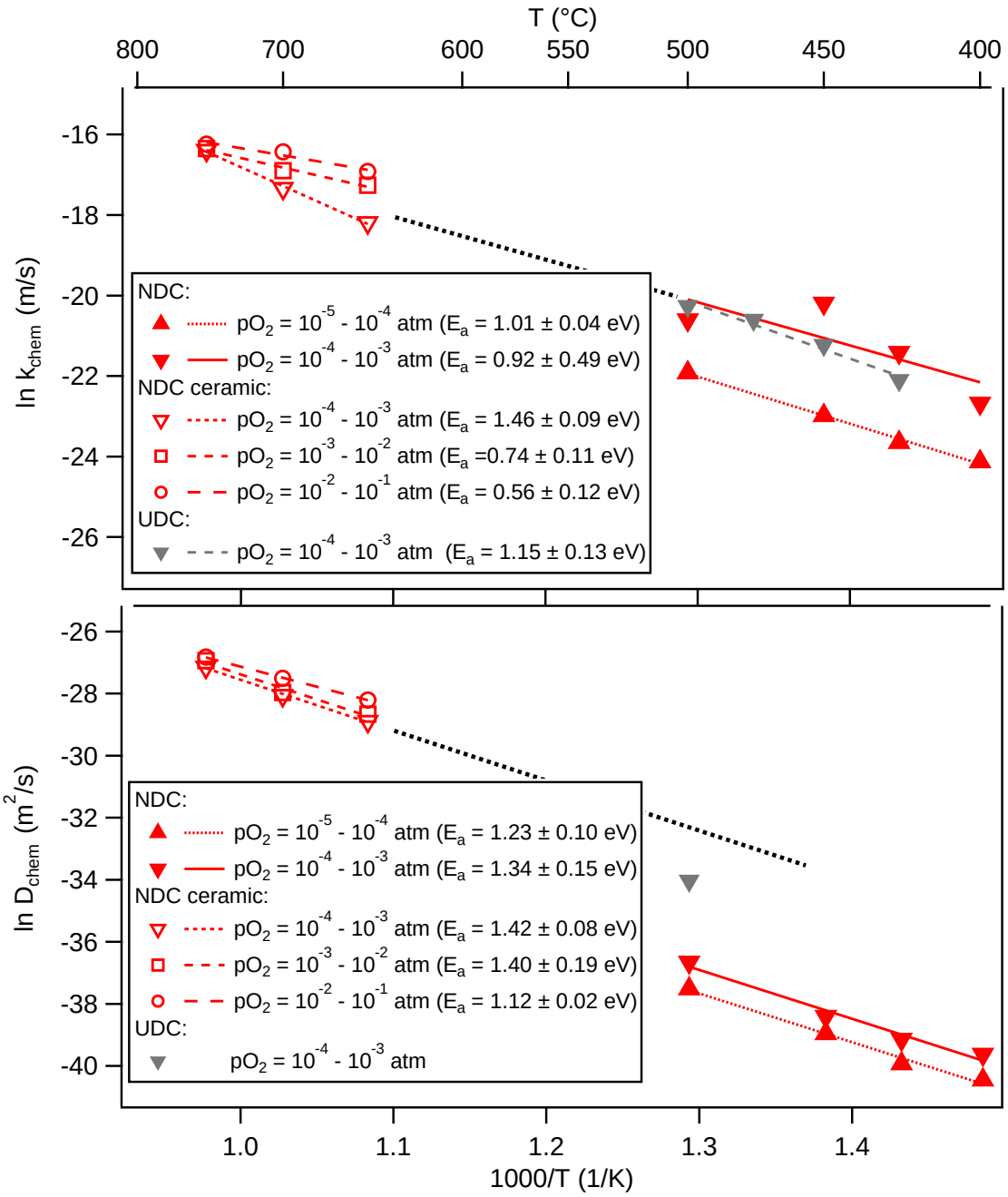

Fig. 8.1: Temperature dependence of the exchange and diffusion coefficients for undoped and Nb-doped CeO_2 thin films and Nb-doped ceria ceramic samples.

from $\sim pO_2^{0.06}$ to $\sim pO_2^{0.45}$ in the investigated pressure region (cf. table 8.1). Although the expected values do not match the measured pO_2 dependence of D_{chem}, it explains qualitatively the increase of the diffusivity with oxygen pressure.

Analogously, the diffusivity of UDC has no significant trend with pO_2. In UDC, oxygen is transported via a vacancy mechanism. In the investigated temperature and oxygen pressure range, the oxygen vacancy concentration is determined by the acceptor impurity concentration and therefore independent on pO_2 (cf. Fig 6.3 on page 68).

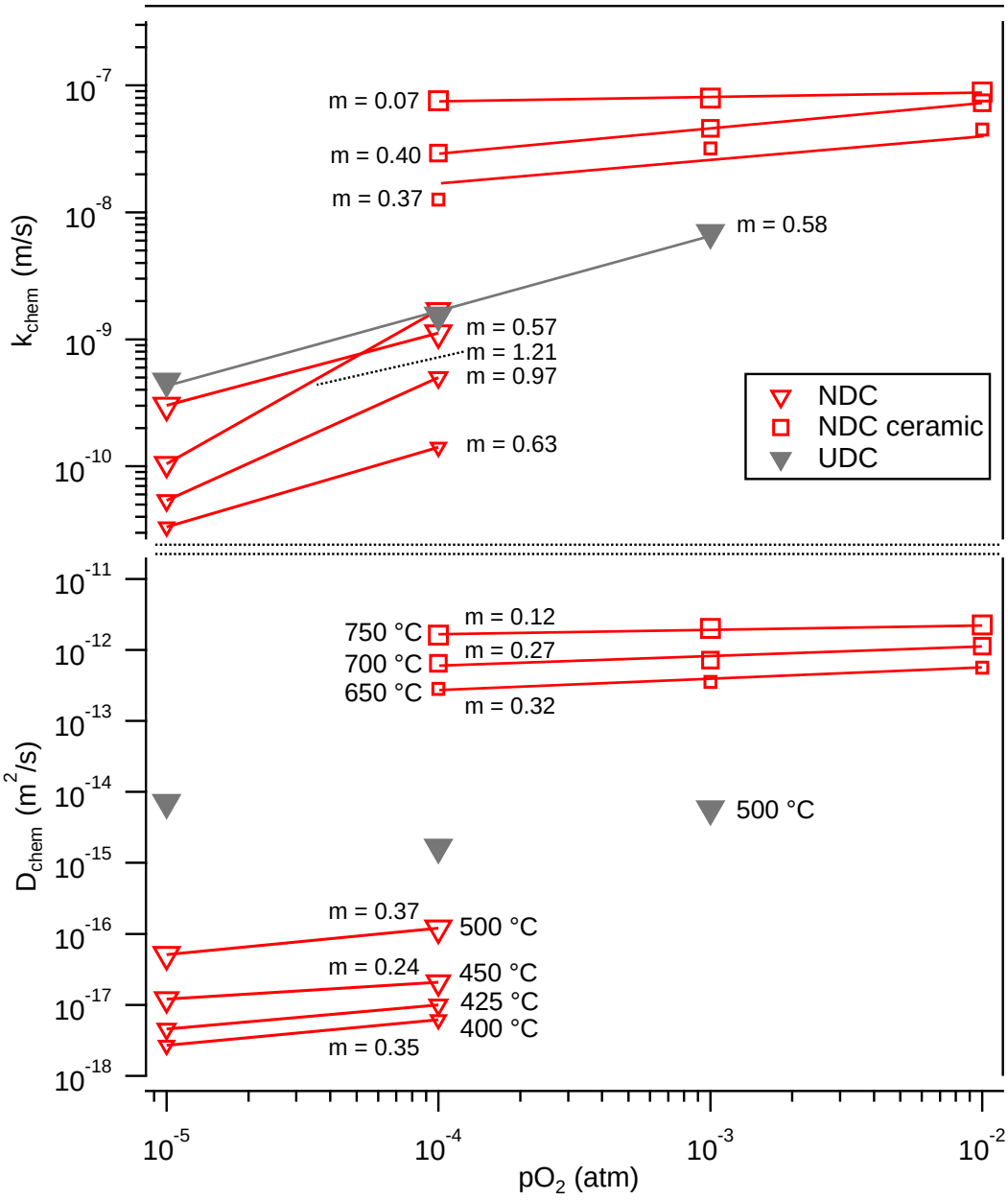

Fig. 8.2: Oxygen pressure dependence ($\sim pO_2{}^m$) of the exchange and diffusion coefficients for undoped and Nb-doped CeO_2 thin films and Nb-doped ceria ceramic samples.

In order to explain the oxygen pressure dependence of the exchange coefficient, the partial reactions of oxygen incorporation, introduced in section 2.3.1 (pp. 8f) have to be taken into account. With the pO_2 dependence of the charge carrier density n and the oxygen vacancy and interstitial concentration, obtained from the equilibrium conductivity and defect model for NDC in chapter 6, the oxygen pressure dependence of each partial reaction of oxygen incorporation can be calculated.

The results are summarized in Table 8.1. r_1 represents the adsorption reaction of molecular oxygen on the surface and is thus $\sim pO_2$ for all samples. r_2, r_3 and r_4 correspond to

the first electron transfer, electron transfer with dissociation of the peroxide and further reduction of O^- to O^{2-}, respectively. In the last reaction step, the oxygen anion is incorporated into the lattice by occupying either an oxygen vacancy (r_{5a}) or an interstitial lattice position (r_{5b}).

Comparing the calculated oxygen pressure dependence of the partial reactions with the measured pO_2 dependence of the exchange coefficient indicates, which reaction step is likely rate determining for the exchange of oxygen. From this can be concluded, that the transfer of the first and second electron, corresponding to r_2 and r_3, are likely the rate determining step for UDC and NDC at temperatures up to 500 °C.

For the NDC ceramic samples the exponent of the oxygen pressure dependence is decreased compared to the NDC thin films, which were also measured at a lower temperature. At 650 and 700 °C the measured pO_2 dependence fits best with the reaction rate for the last electron transfer (r_4). While for all samples investigated below 700 °C electron transfer is rate determining, the mechanism changes at higher temperature. At 750 °C the oxygen pressure dependence of k_{chem} indicates that the interstitial incorporation of the O^{2-} anion into the lattice becomes the rate determining step.

A reason for this shift of the rate determining step from the first electron transfer to second electron transfer to lattice incorporation with increasing temperature for NDC samples could be related to the different energy levels of the differently charged oxygen adsorbates. From the much lower first electron affinity of oxygen ($\Delta H = -141$ kJ/mol) compared to the second electron affinity ($\Delta H = +845$ kJ/mol) [172], the energetic barrier for the transfer of one electron to an O_2 molecule is expected to be lower than the transfer of an additional electron to O^- resulting in a reduction to O^{2-}, while the final lattice incorporation of oxygen should be related to the migration enthalpy of an oxygen interstitial. Thus, with increasing temperature the reaction steps with lower activation energies are likely not limiting the overall oxygen exchange.

The data points for NDC at $pO_2 = 10^{-4}$ atm at 425 and 450 °C were not included in the discussion since these are likely not accurate. The fits of the corresponding conductivity relaxation profiles (profiles 10 and 12 in Fig. 6.16 on p. 83) did not match as well as the other NDC samples at the beginning of the profile, which is the crucial part especially for the determination of k_{chem}.

8.2 Comparison with literature results

In order to compare k and D for Nb-doped ceria with results of undoped and acceptor-doped CeO_2 from literature results, the chemical exchange coefficients and diffusivity obtained from conductivity relaxation experiments were converted into tracer coeffi-

Table 8.1: Exponents m of the oxygen pressure dependence ($\sim pO_2{}^m$) of the exchange coefficients and diffusivity of undoped und Nb-doped CeO_2 in comparison to the pO_2 dependence expected for each partial reaction of oxygen incorporation calculated according to Eqs. 2.5-2.8,2.10 and 2.12 in section 2.3.1. Values correspond to the pO_2 range shown in Fig. 8.2.

	UDC 500 °C	NDC 400 °C	NDC 500 °C	NDC ceramic 650 °C	NDC ceramic 700 °C	NDC ceramic 750 °C
D_{chem}	-	0.35	0.37	0.32	0.27	0.12
n	-0.25	-0.23	-0.20	-0.05	-0.03	-0.01
$[O_i'']$	-	0.06	0.18	0.31	0.38	0.45
Reaction rate						
r_1	1	1	1	1	1	1
r_2	**0.75**	**0.77**	**0.80**	0.95	0.97	0.99
r_3	0.25	0.27	**0.30**	0.45	0.47	0.49
r_4	0	0.04	0.10	**0.40**	**0.44**	0.48
r_{5a}	0	-	-	-	-	-
r_{5b}	-	-0.02	-0.08	0.09	0.06	**0.03**
k_{chem}	0.58	0.63	0.57	0.37	0.40	0.07

cients as described in section 2.3.2. The thermodynamic factors, which are necessary for the conversion, were calculated with the defect concentrations obtained from the same point defect model which was used to fit the conductivity data in chapter 6.

Fig. 8.3 shows the tracer exchange and diffusion coefficients for Nb-, Gd- and undoped CeO_2 samples. The general trend of the diffusivity with $D^*(\text{NDC}) < D^*(\text{UDC}) < D^*(\text{GDC})$ is as expected from the transport mechanisms. For GDC and UDC, an oxygen vacancy mechanism is dominating, while oxygen interstitial diffusion is dominating in NDC. With a migration enthalpy of 1.28 eV for interstitial oxygen in Nb-doped CeO_2 [96] the diffusivity via interstitials is expected to be much lower compared to a vacancy mechanism with typical migration enthalpies of ~ 0.8 eV. In addition, the $V_O^{\bullet\bullet}$ concentration is higher in GDC, due to the acceptor-doping. This explains why Gd-doped ceria has the higher diffusivity compared to undoped CeO_2.

The D^* from conductivity measurements for the ceramic NDC samples compares well with the results for ceramic NDC from SIMS measurements, which validates that reasonable results can be obtained from conductivity relaxation measurements. It is striking, that, besides the significantly higher diffusivity compared to thin films, the activation energy also differs significantly. While E_a for the NDC films is with 1.66 eV in a range where it could be expected from the migration enthalpy for oxygen interstitials, the activation energy for D^* is surprisingly low with $E_a = 0.66 \pm 0.18$ eV for the ceramic samples, despite the large scatter of the data.

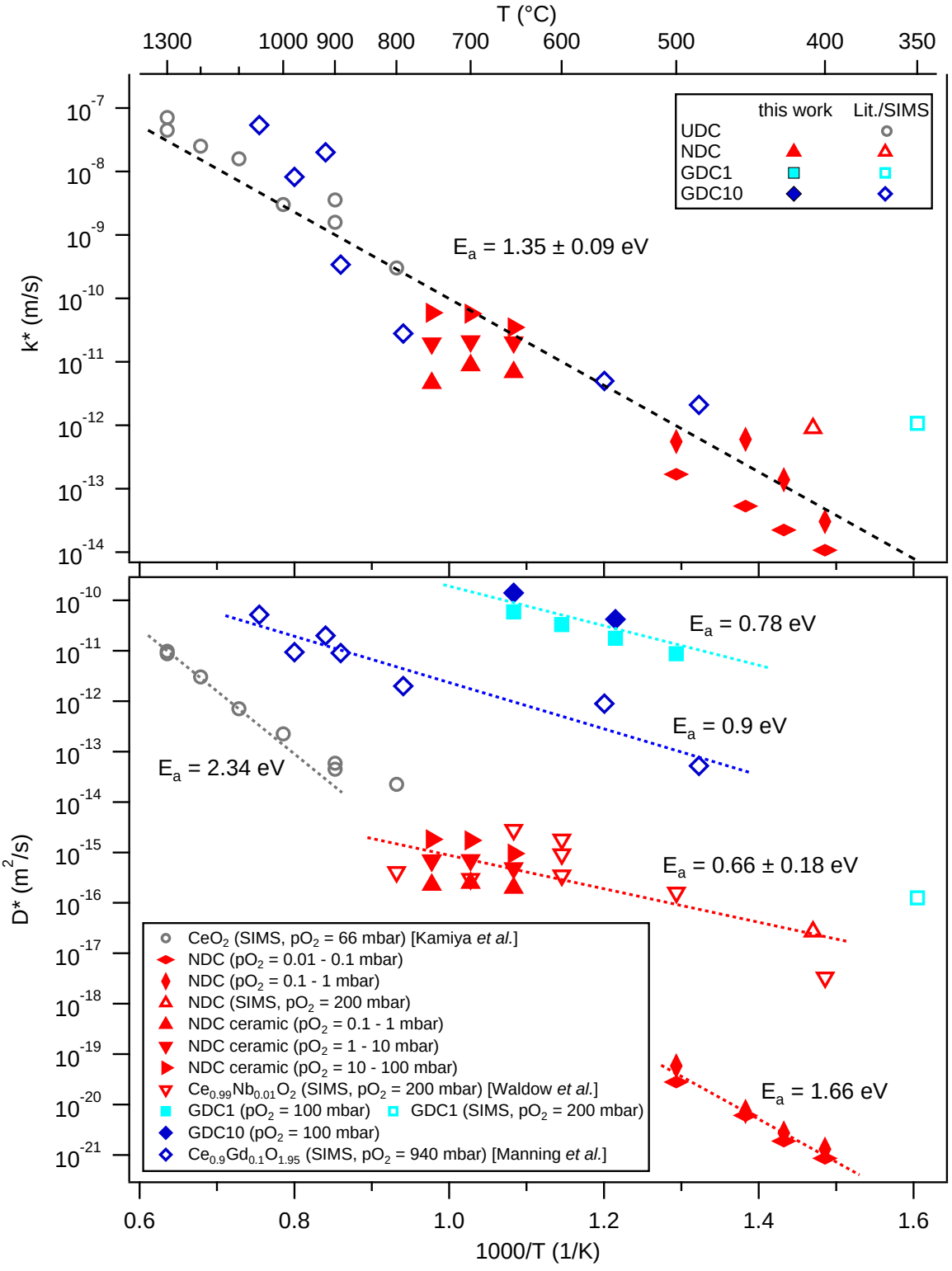

Fig. 8.3: Comparison of exchange and diffusion coefficients for differently doped CeO_2. Literature results from tracer exchange and SIMS experiments for ceramic samples are included from Kamiya *et al.*[72], Waldow *et al.*[96] and Manning *et al.*[12]. Diffusion coefficients from conductivity relaxation measurements were transformed into tracer diffusion coefficients for better comparability.

Comparing the exchange coefficients of differently doped CeO_2, no significant trend of k^* can be seen between acceptor-, undoped or donor-doped ceria. The difference in the exchange coefficients are mostly due to the different temperatures and to some extent from the effect of pO_2 on k. An activation energy of 1.35 ± 0.09 eV fits the tracer exchange coefficients independent on doping. This is an interesting result, since major differences between acceptor- and donor- doped CeO_2 were expected from the different oxygen incorporation mechanisms ($V_O^{\bullet\bullet}$ vs. O_i'') and the significantly higher charge carrier density in Nb-doped CeO_2 compared to undoped and Gd-doped ceria. It suggests, that the surface properties of CeO_2 are not influenced significantly by doping, but are determined by surface effects that are intrinsic to ceria.

8.3 Summary

Within this chapter, the diffusion and oxygen exchange coefficients of Nb- and undoped ceria obtained from conductivity relaxation measurements were investigated. For Nb-doped CeO_2 the activation energy of the diffusivity ranges from 1.1 to 1.4 eV and is similar for thin films and ceramic samples, although the absolute diffusivity is higher in ceramic samples, which is likely an effect of the smaller grain size of the thin films. The exchange coefficients of UDC, NDC ceramics and thin films were determined to be in a comparable range, with similar activation energies.

From the oxygen pressure dependence of the exchange coefficients of NDC, it was concluded, that for temperatures up to 700 °C the electron transfer to the adsorbate is the rate determining step, despite the higher electron concentration in NDC, which was expected to promote the electronic transfer.

From the comparison of the Nb-doped ceria data with exchange coefficients for undoped and Gd-doped CeO_2 from literature, no significant influence of doping on the oxygen exchange coefficients was found, but on contrary, the exchange coefficients of Nb-, Gd- and undoped ceria are comparable. In addition, the activation energy for the exchange was determined to be independent of doping with 1.35 eV. This result is even more surprising since a strong Gd segregation is expected at the surface in the case of GDC as was shown in chapter 5 (cf. Fig. 5.9 on page 52).

9 Summary and Conclusion

The goal of this thesis was to investigate a correlation between the surface potentials of ceria and its surface exchange coefficients. In order to do this, differently doped thin films were prepared to vary the Fermi level position. In addition, for a variation of the surface dipole, films with different crystallographic orientations were investigated. Depending on doping and film deposition conditions an overall variation of 1.9 eV of the Fermi level position is found. Furthermore, the ionization potential ranges from 6.5 to 8.0 eV, if oxygen plasma treated films are not considered. While this, in general, would lead to a huge variation of the work function, films with higher E_F show simultaneously higher ionization potentials, which reduces the effect of the Fermi level shift on the work function. As a result, the work functions of most films are similar with an average value around 4.7 ± 0.5 eV independent on doping. With the results from last chapter, where no significant influence of doping on the exchange coefficient is found, it becomes clear, that a correlation between work function and surface exchange cannot be concluded from this thesis.

The reason for this, however, is likely not due to the underlying hypothesis, but rather due to the fact that CeO_2 is not a suitable model system for such an investigation. As discussed in chapter 5, the surface chemistry of CeO_2 is very complex. Generally, surface space charge layers [132] and high Ce^{3+} surface concentrations [85] are expected for ceria. From the results of this work, the former is expected to be very narrow. However, this affects the determination of the electronic structure. Although photoelectron spectroscopy is a very surface sensitive method, narrow space charge regions of about 1 nm do not have a strong effect on the measurement result as mostly bulk is probed in this case. Moreover, the high Ce^{3+} concentration at the surface, which is found independently of doping, are likely the determining factor for the oxygen exchange. In addition, the diffusion mechanism changes from an oxygen vacancy to an oxygen interstitial mechanism when ceria is donor-doped, since the vacancy concentration is reduced significantly by Nb-doping while the oxygen interstitial concentration increases. As a result, the comparison of donor- with acceptor-doped CeO_2 should have been done with caution, even if the surface chemistry of ceria was not as complex.

Despite that, this thesis provides the first systematic study of surface potentials of CeO_2 in dependence of doping and surface orientation. Due to the different Tasker types of

the investigated surfaces, significant changes in the ionization potential were expected for the polar (100), type III, surface, but not for the unpolar (111) and (110) surfaces, type II and I, respectively. However, a significant difference of the ionization potential of the different surface orientation is not found. In addition, the Ce^{3+} surface concentrations of acceptor-, donor- and undoped ceria were similar. In literature, the high Ce^{3+} concentrations of ceria are mostly explained by a space charge potential at the surface [129–132], where vacancies accumulate at the surface. However this model does not fully explain the results from this thesis, especially why the Ce^{3+} surface concentrations are the same in Nb-doped CeO_2 as in Gd-doped ceria. Nb-doping is expected to suppress the formation of oxygen vacancies (cf. Fig. 3.5 on 25). A significant effect on the Ce^{3+} concentration due to vacancy diffusion to the surface is unlikely when the overall vacancy concentration is as low as in Nb-doped ceria. It appears more likely that the high Ce^{3+} concentration at the surface is due to surface vacancy formation as a consequence of surface reconstruction as an intrinsic property of CeO_2. Another possible explanation could be a surface dipole at the surface involving Ce^{3+} and peroxide species, that could also be related to the reconstruction of the surface. Such a dipole might exist instead or in addition to a surface space charge layer.

The conductivity as a function of temperature and oxygen partial pressure was measured for Nb-, Gd- and undoped CeO_2 thins films, as well as Nb-doped ceramic samples. While this is a well studied subject for Gd- and undoped ceria, there are only few reports on Nb-doped ceria. Especially the comparison of thin film samples with ceramics revealed new information about the influence of grain boundaries on the electronic conductivity of donor-doped ceria. Electronically blocking grain boundaries in Nb-doped CeO_2 thin films have been reported in literature [28]. The comparison between ceramics and thin films in this work lead to the conclusion that the barriers for electron transport due to depletion layers at grain boundaries are only present in thin film samples and are thus related to the deposition process. It is assumed, that Nb is not incorporated entirely into the CeO_2 lattice during the physical vapor deposition process, as has been shown before for Nb-doped $BaTiO_3$ [155].

From conductivity relaxation measurements, the exchange and diffusion coefficients of donor- and undoped CeO_2 were determined. Although no direct correlation to the surface potentials could be made, this work constitutes, to the author's best knowledge, the first investigation of the oxygen exchange coefficient of donor-doped ceria.

Bibliography

[1] A. Trovarelli, "Structural and Oxygen Storage/Release Properties of CeO_2-Based Solid Solutions," *Comments on Inorganic Chemistry*, vol. 20, pp. 263–284, 1999.

[2] T. Bunluesin, R. Gorte, and G. Graham, "CO oxidation for the characterization of reducibility in oxygen storage components of three-way automotive catalysts," *Applied Catalysis B: Environmental*, vol. 14, pp. 105–115, 1997.

[3] T. Bunluesin, R. Gorte, and G. Graham, "Studies of the water-gas-shift reaction on ceria-supported Pt, Pd, and Rh: Implications for oxygen-storage properties ," *Applied Catalysis B: Environmental*, vol. 15, pp. 107–114, 1998.

[4] B. Steele, "Appraisal of $Ce_{1-y}Gd_yO_{2-y/2}$ electrolytes for IT-SOFC operation at 500 °C," *Solid State Ionics*, vol. 129, pp. 95–110, 2000.

[5] H. Inaba and H. Tagawa, "Ceria-based solid electrolytes," *Solid State Ionics*, vol. 83, pp. 1–16, 1996.

[6] Y. Leng, S. Chan, S. Jiang, and K. Khor, "Low-temperature SOFC with thin film GDC electrolyte prepared in situ by solid-state reaction," *Solid State Ionics*, vol. 170, pp. 9–15, 2004.

[7] Z. Shao, S. M. Haile, J. Ahn, P. D. Ronney, Z. Zhan, and S. A. Barnett, "A thermally self-sustained micro solid-oxide fuel-cell stack with high power density," *Nature*, vol. 435, pp. 795–798, 2005.

[8] R. J. Gorte, S. Park, J. M. Vohs, and C. Wang, "Anodes for Direct Oxidation of Dry Hydrocarbons in a Solid-Oxide Fuel Cell," *Advanced Materials*, vol. 12, pp. 1465–1469, 2000.

[9] M. Mogensen, T. Lindegaard, U. R. Hansen, and G. Mogensen, "Physical Properties of Mixed Conductor Solid Oxide Fuel Cell Anodes of Doped CeO_2 ," *Journal of The Electrochemical Society*, vol. 141, pp. 2122–2128, 1994.

[10] V. Matolín, M. Cabala, I. Matolínová, M. Łkoda, M. Václavů, K. Prince, T. Skála, T. Mori, H. Yoshikawa, Y. Yamashita, S. Ueda, and K. Kobayashi, "Pt and Sn Doped Sputtered CeO_2 Electrodes for Fuel Cell Applications," *Fuel Cells*, vol. 10, pp. 139–144, 2010.

[11] R. Merkle and J. Maier, "How Is Oxygen Incorporated into Oxides? A Comprehensive Kinetic Study of a Simple Solid-State Reaction with $SrTiO_3$ as a Model Material," *Angewandte Chemie International Edition*, vol. 47, pp. 3874–3894, 2008.

[12] P. Manning, J. Sirman, and J. Kilner, "Oxygen self-diffusion and surface exchange studies of oxide electrolytes having the fluorite structure," *Solid State Ionics*, vol. 93, pp. 125–132, 1997.

[13] J. Lane and J. Kilner, "Oxygen surface exchange on gadolinia doped ceria," *Solid State Ionics*, vol. 136-137, pp. 927–932, 2000.

[14] P. B. Weisz, "Effects of Electronic Charge Transfer between Adsorbate and Solid on Chemisorption and Catalysis," *The Journal of Chemical Physics*, vol. 21, pp. 1531–1538, 1953.

[15] K. Hauffe, "The Application of the Theory of Semiconsuctors to Problems of Heterogeneous Catalysis," *Advances in Catalysis*, vol. 7, pp. 213–257, 1955.

[16] K. Hauffe, "Über den Mechanismus von Gasreaktionen an Oberflächen halbleitender Katalysatoren," *Advanced in Catalysis*, vol. 9, pp. 187–203, 1957.

[17] J. Haber and M. Witko, "Oxidation catalysis - electronic theory revisited," *Journal of Catalysis*, vol. 216, pp. 416–424, 2003.

[18] A. Klein, "Transparent Conducting Oxides: Electronic Structure-Property Relationship from Photoelectron Spectroscopy with in situ Sample Preparation," *Journal of the American Ceramic Society*, vol. 96, pp. 331–345, 2013.

[19] H. L. Tuller and A. S. Nowick, "Defect Structure and Electrical Properties of Nonstoichiometric CeO_2 Single Crystals," *Journal of The Electrochemical Society*, vol. 126, pp. 209–217, 1979.

[20] Y.-M. Chiang, E. Lavik, and D. Blom, "Defect thermodynamics and electrical properties of nanocrystalline oxides: pure and doped CeO_2 ," *Nanostructured Materials*, vol. 9, pp. 633–642, 1997.

[21] T. Zacherle, A. Schriever, R. A. De Souza, and M. Martin, "Ab initio analysis of the defect structure of ceria," *Physical Review B*, vol. 87, no. 134104, 2013.

[22] M. Martin, T. Zacherle, A. Schriever, R. A. De Souza, and S. Grieshammer, "Ab Initio Calculation of the Defect Structure of Ceria," *ECS Transactions*, vol. 57, pp. 2405–2410, 2013.

[23] S. Grieshammer, T. Zacherle, and M. Martin, "Entropies of defect formation in ceria from first principles," *Phys. Chem. Chem. Phys.*, vol. 15, pp. 15935–15942, 2013.

[24] S. Wang, H. Inaba, H. Tagawa, M. Dokiya, and T. Hashimoto, "Nonstoichiometry of $Ce_{0.9}Gd_{0.1}O_{1.95-x}$," *Solid State Ionics*, vol. 107, pp. 73–79, 1998.

[25] S. Lübke and H.-D. Wiemhöfer, "Electronic conductivity of Gd-doped ceria with additional Pr-doping," *Solid State Ionics*, vol. 117, pp. 229–243, 1999.

[26] M. R. De Guire, M. J. Shingler, and E. Dincer, "Point defect analysis and microstructural effects in pure and donor-doped ceria," *Solid State Ionics*, vol. 52, pp. 155–163, 1992.

[27] K. Yashiro, T. Suzuki, A. Kaimai, H. Matsumoto, Y. Nigara, T. Kawada, J. Mizusaki, J. Sfeir, and J. V. herle, "Electrical properties and defect structure of niobia-doped ceria ," *Solid State Ionics*, vol. 175, pp. 341–344, 2004.

[28] M. C. Göbel, G. Gregori, and J. Maier, "Electronically blocking grain boundaries in donor doped cerium dioxide," *Solid State Ionics*, vol. 215, pp. 45–51, 2012.

[29] R. W. G. Wyckoff *, Crystal Structures (Interscience, New York)*, vol. 1, p. 298, 1963.

[30] PDF #00-004-0593 *, PDF-4+ 2014 (Database), edited by Dr. Soorya Kabekkodu, International Centre for Diffraction Data, Newtown Square, PA, USA*, 2014.

[31] K. Momma and F. Izumi, "VESTA 3 for three-dimensional visualization of crystal, volumetric and morphology data," *Journal of Applied Crystallography*, vol. 44, pp. 1272–1276, 2011.

[32] E. Wuilloud, B. Delley, W.-D. Schneider, and Y. Baer, "Spectroscopic Evidence for Localized and Extended f-Symmetry States in CeO_2," *Physical Review Letters*, vol. 53, pp. 202–205, 1984.

[33] R. Gillen, S. J. Clark, and J. Robertson, "Nature of the electronic band gap in lanthanide oxides," *Physical Review B*, vol. 87, no. 125116, 2013.

[34] D. Mullins, S. Overbury, and D. Huntley, "Electron spectroscopy of single crystal and polycrystalline cerium oxide surfaces ," *Surface Science*, vol. 409, pp. 307–319, 1998.

[35] H. Tuller and A. Nowick, "Small polaron electron transport in reduced CeO_2 single crystals," *Journal of Physics and Chemistry of Solids*, vol. 38, pp. 859–867, 1977.

[36] L. D. Landau, "Electron motion in crystal lattices," *Physikalische Zeitschrift der Sowjetunion*, vol. 3, p. 664, 1933.

[37] J. Devreese, "Polarons," *Encyclopedia of Applied Physics*, vol. 1, pp. 383–409, 1996.

[38] D. Emin, "Lattice Relaxation and Small-Polaron Hopping Motion," *Physical Review B*, vol. 4, pp. 3639–3651, 1971.

[39] P. W. Tasker, "The stability of ionic crystal surfaces," *Journal of Physics C: Solid State Physics*, vol. 12, p. 4977, 1979.

[40] J. Goniakowski, F. Finocchi, and C. Noguera, "Polarity of oxide surfaces and nanostructures," *Reports on Progress in Physics*, vol. 71, no. 016501, 2008.

[41] Y. Lin, Z. Wu, J. Wen, K. R. Poeppelmeier, and L. D. Marks, "Imaging the Atomic Surface Structures of CeO_2 Nanoparticles," *Nano Letters*, vol. 14, pp. 191–196, 2014.

[42] V. Stetsovych, F. Pagliuca, F. Dvorak, T. Duchon, M. Vorokhta, M. Aulická, J. Lachnitt, S. Schernich, I. Matolínová, K. Veltruská, T. Skála, D. Mazur, J. Myslivecek, J. Libuda, and V. Matolín, "Epitaxial Cubic Ce_2O_3 Films via Ce-CeO_2 Interfacial Reaction," *The Journal of Physical Chemistry Letters*, vol. 4, pp. 866–871, 2013.

[43] B. Chen, Y. Ma, L. Ding, L. Xu, Z. Wu, Q. Yuan, and W. Huang, "Reactivity of Hydroxyls and Water on a CeO_2(111) Thin Film Surface: The Role of Oxygen Vacancy," *The Journal of Physical Chemistry C*, vol. 117, pp. 5800–5810, 2013.

[44] H. Nörenberg and G. A. D. Briggs, "Defect Structure of Nonstoichiometric CeO_2(111) Surfaces Studied by Scanning Tunneling Microscopy," *Physical Review Letters*, vol. 79, pp. 4222–4225, 1997.

[45] N. V. Skorodumova, M. Baudin, and K. Hermansson, "Surface properties of CeO_2 from first principles," *Physical Review B*, vol. 69, no. 075401, 2004.

[46] M. Nolan, S. Grigoleit, D. C. Sayle, S. C. Parker, and G. W. Watson, "Density functional theory studies of the structure and electronic structure of pure and defective low index surfaces of ceria," *Surface Science*, vol. 576, pp. 217–229, 2005.

[47] Y. Namai, K.-i. Fukui, and Y. Iwasawa, "Atom-Resolved Noncontact Atomic Force Microscopic Observations of CeO_2(111) Surfaces with Different Oxidation States: Surface Structure and Behavior of Surface Oxygen Atoms," *The Journal of Physical Chemistry B*, vol. 107, pp. 11666–11673, 2003.

[48] H. Nörenberg and G. Briggs, "The surface structure of CeO_2(110) single crystals studied by STM and RHEED," *Surface Science*, vol. 433, pp. 127–130, 1999.

[49] C. Yang, X. Yu, S. Heißler, A. Nefedov, S. Colussi, J. Llorca, A. Trovarelli, Y. Wang, and C. Wöll, "Surface Faceting and Reconstruction of Ceria Nanoparticles," *Angewandte Chemie International Edition*, vol. 56, pp. 375–379, 2017.

[50] P. Ágoston and K. Albe, "Thermodynamic stability, stoichiometry, and electronic structure of bcc-In_2O_3 surfaces," *Physical Review B*, vol. 84, p. 045311, 2011.

[51] P. Ágoston, "Point Defect and Surface Properties of In_2O_3 and SnO_2: a Comparative Study by First-Principles Methods," *Technische Universität Darmstadt*, 2011.

[52] M. V. Hohmann, P. Ágoston, A. Wachau, T. J. M. Bayer, J. Brötz, K. Albe, and A. Klein, "Orientation dependent ionization potential of In_2O_3: a natural source for inhomogeneous barrier formation at electrode interfaces in organic electronics," *Journal of Physics: Condensed Matter*, vol. 23, no. 334203, 2011.

[53] H. Nörenberg and J. Harding, "The surface structure of CeO_2(001) single crystals studied by elevated temperature STM," *Surface Science*, vol. 477, pp. 17–24, 2001.

[54] T. Ishihara, J. A. Kilner, M. Honda, N. Sakai, H. Yokokawa, and Y. Takita, "Oxygen surface exchange and diffusion in $LaGaO_3$ based perovskite type oxides," *Solid State Ionics*, vol. 113-115, pp. 593–600, 1998.

[55] F. Kröger and H. Vink, "Relations between the Concentrations of Imperfections in Crystalline Solids," *Solid State Ionics*, vol. 3, pp. 307–435, 1956.

[56] X. Zhu and W. Yang, "Mixed Conducting Ceramic Membranes; Fundamentals, Materials and Applications," *Springer-Verlag GmbH Germany*, 2017.

[57] E. G. Seebauer and M. C. Kratzer, "Charged Semiconductor Defects; Structure, Thermodynamics and Diffusion," *Springer-Verlag London Limited*, 2009.

[58] K. Yashiro, S. Onuma, A. Kaimai, Y. Nigara, T. Kawada, J. Mizusaki, K. Kawamura, T. Horita, and H. Yokokawa, "Mass transport properties of $Ce_{0.9}Gd_{0.1}O_{2-\delta}$ at the surface and in the bulk," *Solid State Ionics*, vol. 152-153, pp. 469–476, 2002.

[59] G. Gottstein, "Physikalische Grundlagen der Materialkunde," *Springer-Verlag Berlin Heidelberg, Dritte Auflage*, 2007.

[60] G. Murch, "The haven ratio in fast ionic conductors," *Solid State Ionics*, vol. 7, pp. 177–198, 1982.

[61] J. H. Joo and G. M. Choi, "Electrical conductivity of thin film ceria grown by pulsed laser deposition," *Journal of the European Ceramic Society*, vol. 27, pp. 4273–4277, 2007.

[62] T. Suzuki, I. Kosacki, and H. U. Anderson, "Defect and Mixed Conductivity in Nanocrystalline Doped Cerium Oxide," *Journal of the American Ceramic Society*, vol. 85, pp. 1492–1498, 2002.

[63] W. J. Bowman, J. Zhu, R. Sharma, and P. A. Crozier, "Electrical conductivity and grain boundary composition of Gd-doped and Gd/Pr co-doped ceria," *Solid State Ionics*, vol. 272, pp. 9–17, 2015.

[64] R. A. De Souza, "A universal empirical expression for the isotope surface exchange coefficients (k*) of acceptor-doped perovskite and fluorite oxides," *Physical Chemistry Chemical Physics*, vol. 8, pp. 890–897, 2006.

[65] R. A. De Souza, "Limits to the rate of oxygen transport in mixed-conducting oxides," *Journal of Materials Chemistry A*, vol. 5, no. 20334, 2017.

[66] G. Christie and F. van Berkel, "Microstructure - ionic conductivity relationships in ceria-gadolinia electrolytes," *Solid State Ionics*, vol. 83, pp. 17–27, 1996.

[67] W. Zajac and J. Molenda, "Properties of doped ceria solid electrolytes in reducing atmospheres," *Solid State Ionics*, vol. 192, pp. 163 –167, 2011.

[68] P. P. Dholabhai, J. B. Adams, P. Crozier, and R. Sharma, "A density functional study of defect migration in gadolinium doped ceria," *Physical Chemistry Chemical Physics*, vol. 12, pp. 7904–7910, 2010.

[69] M. C. Göbel, G. Gregori, X. Guo, and J. Maier, "Boundary effects on the electrical conductivity of pure and doped cerium oxide thin films," *Physical Chemistry Chemical Physics*, vol. 12, pp. 14351–14361, 2010.

[70] P. P. Dholabhai, J. B. Adams, P. Crozier, and R. Sharma, "Oxygen vacancy migration in ceria and Pr-doped ceria: A DFT+U study," *The Journal of Chemical Physics*, vol. 132, no. 094104, 2010.

[71] X. Guo, W. Sigle, and J. Maier, "Blocking Grain Boundaries in Yttria-Doped and Undoped Ceria Ceramics of High Purity," *Journal of the American Ceramic Society*, vol. 86, pp. 77–87, 2003.

[72] M. Kamiya, E. Shimada, Y. Ikuma, M. Komatsu, and H. Haneda, "Intrinsic and Extrinsic Oxygen Diffusion and surface Exchange Reaction in Cerium Oxide," *Journal of The Electrochemical Society*, vol. 147, pp. 1222–1227, 2000.

[73] M. Henderson, C. Perkins, M. Engelhard, S. Thevuthasan, and C. Peden, "Redox properties of water on the oxidized and reduced surfaces of $CeO_2(111)$," *Surface Science*, vol. 526, pp. 1–18, 2003.

[74] M. Björck and G. Andersson, "GenX: an extensible X-ray reflectivity refinement program utilizing differential evolution," *Journal of Applied Crystallography*, vol. 40, pp. 1174–1178, 2007.

[75] A. Klein, T. Mayer, A. Thissen, and W. Jaegermann, "Photoelectron Spectroscopy in Materials Science and Physical Chemistry: Analysis of Composition, Chemical Bonding and Electronic Structure of Surfaces and Interfaces," *BUNSEN-MAGAZIN*, vol. 10, pp. 124–139, 2008.

[76] M. Ohring, "Materials science of thin films," *Academic Press, San Diego, Calif., 2nd edition edition*, 2002.

[77] D. A. Shirley, "High-Resolution X-Ray Photoemission Spectrum of the Valence Bands of Gold," *Physical Review B*, vol. 5, pp. 4709–4714, 1972.

[78] J. F. Moulder, W. F. Stickle, P. E. Sobol, and K. D. Bomben, "Handbook of X-ray Photoelectron Spectroscopy," *Physical Electronics Inc., Eden Prairie, Minn.*, 1995.

[79] H. F. Wardenga and A. Klein, "Surface potentials of (111), (110) and (100) oriented CeO_{2-x} thin films," *Applied Surface Science*, vol. 377, pp. 1–8, 2016.

[80] A. Pfau and K. Schierbaum, "The electronic structure of stoichiometric and reduced CeO_2 surfaces: an XPS, UPS and HREELS study," *Surface Science*, vol. 321, pp. 71–80, 1994.

[81] P. Luches, F. Pagliuca, S. Valeri, and F. Boscherini, "Structure of Ultrathin CeO_2 Films on Pt(111) by Polarization-Dependent X-ray Absorption Fine Structure," *Journal of Physical Chemistry C*, vol. 117, pp. 1030–1036, 2013.

[82] P. Luches, F. Pagliuca, and S. Valeri, "Structural and morphological modifications of thermally reduced cerium oxide ultrathin epitaxial films on Pt(111)," *Physical Chemistry Chemical Physics*, vol. 16, pp. 18848–18857, 2014.

[83] D. R. Mullins, P. M. Albrecht, T.-L. Chen, F. C. Calaza, M. D. Biegalski, H. M. Christen, and S. H. Overbury, "Water Dissociation on CeO_2(100) and CeO_2(111) Thin Films," *The Journal of Physical Chemistry C*, vol. 116, pp. 19419–19428, 2012.

[84] J. Zhang, F. Wei, Z. Yang, Q. Chen, J. Chen, and S. Wang, "Structure and chemical states of highly eptiaxial CeO_2(001) films grown on $SrTiO_3$ substrate by laser molecular beam epitaxy ," *Journal of Rare Earths*, vol. 31, pp. 1191–1194, 2013.

[85] W. C. Chueh, A. H. McDaniel, M. E. Grass, Y. Hao, N. Jabeen, Z. Liu, S. M. Haile, K. F. McCarty, H. Bluhm, and F. El Gabaly, "Highly Enhanced Concentration and

Stability of Reactive Ce^{3+} on Doped CeO_2 Surface Revealed In Operando," *Chemistry of Materials*, vol. 24, pp. 1876–1882, 2012.

[86] A. Kotani and H. Ogasawara, "Theory of core-level spectroscopy of rare-earth oxides ," *Journal of Electron Spectroscopy and Related Phenomena*, vol. 60, pp. 257–299, 1992.

[87] D. A. Creaser, P. G. Harrison, M. Morris, and B. Wolfindale, "X-ray photoelectron spectroscopic study of the oxidation and reduction of a cerium(III) oxide / cerium foil substrate," *Catalysis Letters*, vol. 23, pp. 13–24, 1994.

[88] P. Burroughs, A. Hamnett, A. F. Orchard, and G. Thornton, "Satellite structure in the x-ray photoelectron spectra of some binary and mixed oxides of lanthanum and cerium," *Journal of the Chemical Society, Dalton Transactions*, pp. 1686–1698, 1976.

[89] A. Kotani, T. Jo, and J. Parlebas, "Many-body effects in core-level spectroscopy of rare-earth compounds," *Advances in Physics*, vol. 37, pp. 37–85, 1988.

[90] M. Romeo, K. Bak, J. El Fallah, F. Le Normand, and L. Hilaire, "XPS Study of the Reduction of Cerium Dioxide," *Surface and Interface Analysis*, vol. 20, pp. 508–512, 1993.

[91] M. V. Hohmann, A. Wachau, and A. Klein, "In situ Hall effect and conductivity measurements of ITO thin films," *Solid State Ionics*, vol. 262, pp. 636–639, 2014.

[92] J. Lane and J. Kilner, "Measuring oxygen diffusion and oxygen surface exchange by conductivity relaxation," *Solid State Ionics*, vol. 136-137, pp. 997–1001, 2000.

[93] J. Crank, "The Mathematics of Diffusion," *Oxford University Press*, 1975.

[94] M. H. Hebb, "Electrical Conductivity of Silver Sulfide," *The Journal of Chemical Physics*, vol. 20, pp. 185–190, 1952.

[95] C. Wagner, "Galvanische Zellen mit festen Elektrolyten mit gemischter Stromleitung," *Zeitschrift für Elektrochemie, Berichte der Bunsengesellschaft für physikalische Chemie*, vol. 60, pp. 4–7, 1956.

[96] S. P. Waldow, H. Wardenga, S. Beschnitt, A. Klein, and R. A. De Souza, "The Concentration and Diffusivity of Oxygen Interstitials in Niobia-Doped Ceria," *Journal of Physical Chemistry C*, vol. 123, pp. 6340–6350, 2019.

[97] M. Nakayama and M. Martin, "First-principles study on defect chemistry and migration of oxide ions in ceria doped with rare-earth cations," *Physical Chemistry Chemical Physics*, vol. 11, pp. 3241–3249, 2009.

[98] H. Yahiro, T. Ohuchi, K. Eguchi, and H. Arai, "Electrical properties and microstructure in the system ceria-alkaline earth oxide," *Journal of Materials Science*, vol. 23, pp. 1036–1041, 1988.

[99] T. Kobayashi, S. Wang, M. Dokiya, H. Tagawa, and T. Hashimoto, "Oxygen nonstoichiometry of $Ce_{1-y}Sm_yO_{2-0.5y-x}$ (y=0.1, 0.2)," *Solid State Ionics*, vol. 126, pp. 349–357, 1999.

[100] S. M. Sze and K. K. Ng, "Physics of Semiconductor Devices," *John Wiley & Sons, Inc., Hoboken, New Jersey*, 2007.

[101] Y. J. Kim, Y. Gao, G. S. Herman, S. Thevuthasan, W. Jiang, D. E. McCready, and S. A. Chambers, "Growth and structure of epitaxial CeO_2 by oxygen-plasma-assisted molecular beam epitaxy," *Journal of Vacuum Science & Technology A: Vacuum, Surfaces, and Films*, vol. 17, pp. 926–935, 1999.

[102] M. I. Nandasiri, P. Nachimuthu, T. Varga, V. Shutthanandan, W. Jiang, S. V. N. T. Kuchibhatla, S. Thevuthasan, S. Seal, and A. Kayani, "Influence of growth rate on the epitaxial orientation and crystalline quality of CeO_2 thin films grown on Al_2O_3(0001)," *Journal of Applied Physics*, vol. 109, no. 013525, 2011.

[103] J. J. Yeh and I. Lindau, "Atomic Subshell Photoionization Cross Sections and Asymmetry Parameters: $1 \leq Z \leq 103$," *Atomic Data and Nuclear Data Tables*, vol. 32, pp. 1–155, 1985.

[104] M. Perego and G. Seguini, "Charging phenomena in dielectric/semiconductor heterostructures during X-ray photoelectron spectroscopy measurements," *Journal of Applied Physics*, vol. 110, no. 053711, 2011.

[105] M. Alonso, R. Cimino, and K.Horn, "Surface Photovoltage Effects in Photoemission from Metal-GaP(110) Interfcaes: Importance for Band-Bending Evaluation," *Physical Review Letters*, vol. 64, pp. 1947–1950, 1990.

[106] R. Schafranek, S. Payan, M. Maglione, and A. Klein, "Barrier heights at (Ba,Sr)TiO_3/Pt interfaces studied by photoemission," *Physical Review B*, vol. 77, no. 195310, 2008.

[107] G. Chiodelli, G. Flor, and M. Scagliotti, "Electrical properties of the ZrO_2-CeO_2 system ," *Solid State Ionics*, vol. 91, pp. 109–121, 1996.

[108] A. Gassmann, S. V. Yampolskii, A. Klein, K. Albe, N. Vilbrandt, O. Pekkola, Y. A. Genenko, M. Rehahn, and H. von Seggern, "Study of electrical fatigue by defect engineering in organic light-emitting diodes," *Materials Science and Engineering B*, vol. 192, pp. 26–51, 2015.

[109] M. Nolan, J. E. Fearon, and G. W. Watson, "Oxygen vacancy formation and migration in ceria," *Solid State Ionics*, vol. 177, pp. 3069–3074, 2006.

[110] A. Klein, C. Körber, A. Wachau, F. Säuberlich, Y. Gassenbauer, R. Schafranek, S. P. Harvey, and T. O. Mason, "Surface potentials of magnetron sputtered transparent conducting oxides," *Thin Solid Films*, vol. 518, pp. 1197–1203, 2009.

[111] A. Klein, C. Körber, A. Wachau, F. Säuberlich, Y. Gassenbauer, S. P. Harvey, D. E. Proffit, and T. O. Mason, "Transparent Conducting Oxides for Photovoltaics: Manipulation of Fermi Level,Work Function and Energy Band Alignment," *Materials*, vol. 3, pp. 4892–4914, 2010.

[112] R. Schafranek, S. Li, F. Chen, W. Wu, and A. Klein, "$PbTiO_3/SrTiO_3$ interface: Energy band alignment and its relation to the limits of Fermi level variation," *Physical Review B*, vol. 84, no. 045317, 2011.

[113] K. Rachut, C. Körber, J. Brötz, and A. Klein, "Growth and surface properties of epitaxial SnO_2," *Physica Status Solidi A: Applications and Materials Science*, vol. 211, pp. 1997–2004, 2014.

[114] V. E. Henrich, G. Dresselhaus, and H. J. Zeiger, "Observation of Two-Dimensional Phases Associated with Defect States on the Surface of TiO_2 ," *Physical Review Letters*, vol. 36, pp. 1335–1339, 1976.

[115] V. E. Henrich, G. Dresselhaus, and H. J. Zeiger, "Surface defects and the electronic structure of $SrTiO_3$ surfaces ," *Physical Review B*, vol. 17, pp. 4908–4921, 1978.

[116] M. M. Branda, R. M. Ferullo, M. Causà, and F. Illas, "Relative Stabilities of Low Index and Stepped CeO_2 Surfaces from Hybrid and GGA + U Implementations of Density Functional Theory," *The Journal of Physical Chemistry C*, vol. 115, pp. 3716–3721, 2011.

[117] Y. Zhu, N. Jain, M. K. Hudait, D. Maurya, R. Varghese, and S. Priya, "X-ray photoelectron spectroscopy analysis and band offset determination of CeO2 deposited on epitaxial (100), (110), and (111)Ge," *Journal of Vacuum Science & Technology B*, vol. 32, no. 011217, 2014.

[118] Z. Yang, T. K. Woo, M. Baudin, and K. Hermansson, "Atomic and electronic structure of unreduced and reduced CeO_2 surfaces: A first-principles study," *The Journal of Chemical Physics*, vol. 120, pp. 7741–7749, 2004.

[119] M. V. Ganduglia-Pirovano, J. L. F. Da Silva, and J. Sauer, "Density-Functional Calculations of the Structure of Near-Surface Oxygen Vacancies and Electron Localization on $CeO_2(111)$," *Physical Review Letters*, vol. 102, no. 026101, 2009.

[120] G. E. Murgida and M. V. Ganduglia-Pirovano, "Evidence for Subsurface Ordering of Oxygen Vacancies on the Reduced $CeO_2(111)$ Surface Using Density-Functional and Statistical Calculations," *Physical Review Letters*, vol. 110, no. 246101, 2013.

[121] S. Torbrügge, M. Reichling, A. Ishiyama, S. Morita, and O. Custance, "Evidence of Subsurface Oxygen Vacancy Ordering on Reduced $CeO_2(111)$," *Physical Review Letters*, vol. 99, no. 056101, 2007.

[122] D. C. Grinter, R. Ithnin, C. L. Pang, and G. Thornton, "Defect Structure of Ultrathin Ceria Films on Pt(111): Atomic Views from Scanning Tunnelling Microscopy," *The Journal of Physical Chemistry C*, vol. 114, pp. 17036–17041, 2010.

[123] G. Praline, B. Koel, R. Hance, H.-I. Lee, and J. White, "X-ray photoelectron study of the reaction of oxygen with cerium," *Journal of Electron Spectroscopy and Related Phenomena*, vol. 21, pp. 17–30, 1980.

[124] T. Hasegawa, S. M. F. Shahed, Y. Sainoo, A. Beniya, N. Isomura, Y. Watanabe, and T. Komeda, "Epitaxial growth of $CeO_2(111)$ film on Ru(0001): Scanning tunneling microscopy (STM) and x-ray photoemission spectroscopy (XPS) study," *The Journal of Chemical Physics*, vol. 140, no. 044711, 2014.

[125] J. Holgado, G. Munuera, J. Espinós, and A. González-Elipe, "XPS study of oxidation processes of CeOx defective layers," *Applied Surface Science*, vol. 158, pp. 164–171, 2000.

[126] G. Wang, D. Kong, Y. Pan, H. Pan, and J. Zhu, "Low energy Ar-ion bombardment effects on the CeO_2 surface," *Applied Surface Science*, vol. 258, pp. 2057–2061, 2012.

[127] G. S. Herman, Y. J. Kim, S. A. Chambers, and C. H. F. Peden, "Interaction of D_2O with $CeO_2(001)$ Investigated by Temperature-Programmed Desorption and X-ray Photoelectron Spectroscopy," *Langmuir*, vol. 15, pp. 3993–3997, 1999.

[128] Y. Zhao, B.-T. Teng, X.-D. Wen, Y. Zhao, Q.-P. Chen, L.-H. Zhao, and M.-F. Luo, "Superoxide and Peroxide Species on $CeO_2(111)$, and Their Oxidation Roles," *The Journal of Physical Chemistry C*, vol. 116, pp. 15986–15991, 2012.

[129] J. Maier, "Nano-Ionics: Trivial and Non-Trivial Size Effects on Ion Conduction in Solids," *Zeitschrift für Pyhsikalische Chemie*, vol. 217, pp. 415–436, 2003.

[130] J. Maier, "Defect chemistry and ion transport in nanostructured materials: Part II. Aspects of nanoionics ," *Solid State Ionics*, vol. 157, pp. 327–334, 2003.

[131] X. Guo and R. Waser, "Space charge concept for acceptor-doped zirconia and ceria and experimental evidences," *Solid State Ionics*, vol. 173, pp. 63–67, 2004.

[132] A. F. Zurhelle, X. Tong, A. Klein, D. S. Mebane, and R. A. De Souza, "A Space-Charge Treatment of the Increased Concentration of Reactive Species at the Surface of a Ceria Solid Solution," *Angewandte Chemie International Edition*, vol. 129, pp. 14708–14712, 2017.

[133] D. C. Sayle, S. A. Maicaneanu, and G. W. Watson, "Atomistic Models for CeO_2(111), (110), and (100) Nanoparticles, Supported on Yttrium-Stabilized Zirconia," *Journal of the American Chemical Society*, vol. 124, pp. 11429–11439, 2002.

[134] E. Aneggi, D. Wiater, C. de Leitenburg, J. Llorca, and A. Trovarelli, "Shape-Dependent Activity of Ceria in Soot Combustion," *ACS Catalysis*, vol. 4, pp. 172–181, 2014.

[135] T. Désaunay, G. Bonura, V. Chiodo, S. Freni, J.-P. Couzinié, J. Bourgon, A. Ringuedé, F. Labat, C. Adamo, and M. Cassir, "Surface-dependent oxidation of H_2 on CeO_2 surfaces," *Journal of Catalysis*, vol. 297, pp. 193–201, 2013.

[136] H. Yahiro, Y. Eguchi, K. Eguchi, and H. Arai, "Oxygen ion conductivity of the ceria-samarium oxide system with fluorite structure," *Journal of Applied Electrochemistry*, vol. 18, pp. 527–531, 1988.

[137] D. Pérez-Coll, D. Marrero-López, J. Ruiz-Morales, P. Núñez, J. Abrantes, and J. Frade, "Reducibility of $Ce_{1-x}Gd_xO_{2-\delta}$ in prospective working conditions," *Journal of Power Sources*, vol. 173, pp. 291–297, 2007.

[138] A. Tschöpe, "Grain size-dependent electrical conductivity of polycrystalline cerium oxide II: Space charge model ," *Solid State Ionics*, vol. 139, pp. 267–280, 2001.

[139] W. Lee, H. J. Jung, M. H. Lee, Y.-B. Kim, J. S. Park, R. Sinclair, and F. B. Prinz, "Oxygen Surface Exchange at Grain Boundaries of Oxide Ion Conductors," *Advanced Functional Materials*, vol. 22, pp. 965–971, 2012.

[140] P. Scanlon, R. Bink, F. van Berkel, G. Christie, L. van IJzendoorn, H. Brongersma, and R. van Welzenis, "Surface composition of ceramic CeGd-oxide," *Solid State Ionics*, vol. 112, pp. 123–130, 1998.

[141] Y. Lei, Y. Ito, N. D. Browning, and T. J. Mazanec, "Segregation Effects at Grain Boundaries in Fluorite-Structured Ceramics," *Journal of the American Ceramic Society*, vol. 85, pp. 2359–2363, 2002.

[142] G. Harrington, "Oxygen ion transport and dopant segregation in strained oxide thin films," *Imperial College London*, 2015.

[143] H. Kudo, T. Obayashi, "Oxygen ion conduction of the fluorite-type $Ce_{1-x}Ln_xO_{2-x/2}$ (Ln = lanthanoid element)," *Journal of the Electrochemical Society*, vol. 122, pp. 142–147, 1975.

[144] H. J. Avila-Paredes, K. Choi, C.-T. Chen, and S. Kim, "Dopant-concentration dependence of grain-boundary conductivity in ceria: A space-charge analysis," *J. Mater. Chem.*, vol. 19, pp. 4837–4842, 2009.

[145] A. Klein, "Interface Properties of Dielectric Oxides," *Journal of the American Ceramic Society*, vol. 99, pp. 369–387, 2016.

[146] T. Suzuki, I. Kosacki, H. U. Anderson, and P. Colomban, "Electrical Conductivity and Lattice Defects in Nanocrystalline Cerium Oxide Thin Films," *Journal of the American Ceramic Society*, vol. 84, pp. 2007–2014, 2001.

[147] J. L. Rupp and L. J. Gauckler, "Microstructures and electrical conductivity of nanocrystalline ceria-based thin films," *Solid State Ionics*, vol. 177, pp. 2513–2518, 2006.

[148] R. Gerhardt and A. S. Nowick, "Grain-Boundary Effect in Ceria Doped with Trivalent Cations: I, Electrical Measurements," *Journal of the American Ceramic Society*, vol. 69, pp. 641–646, 9 1986.

[149] I. Kosacki, T. Suzuki, V. Petrovsky, and H. U. Anderson, "Electrical conductivity of nanocrystalline ceria and zirconia thin films," *Solid State Ionics*, vol. 137, pp. 1225–1233, 2000.

[150] A. Tschöpe, E. Sommer, and R. Birringer, "Grain size-dependent electrical conductivity of polycrystalline cerium oxide: I. Experiments," *Solid State Ionics*, vol. 139, pp. 255–265, 2001.

[151] J. Maier, "Ionic transport in nano-sized systems," *Solid State Ionics*, vol. 175, pp. 7–2, 2004.

[152] B. Wang and A. N. Cormack, "Strain Modulation of Defect Structure in Gadolinia-Doped Ceria," *The Journal of Physical Chemistry C*, vol. 117, pp. 146–151, 2013.

[153] W. Donner, C. Chen, M. Liu, A. J. Jacobson, Y.-L. Lee, M. Gadre, and D. Morgan, "Epitaxial Strain-Induced Chemical Ordering in $La_{0.5}Sr_{0.5}CoO_{3-\delta}$ Films on $SrTiO_3$," *Chemistry of Materials*, vol. 23, pp. 984–988, 2011.

[154] A. Kushima, S. Yip, and B. Yildiz, "Competing strain effects in reactivity of $LaCoO_3$ with oxygen," *Physical Review B*, vol. 82, no. 115435, 2010.

[155] E. Arveux, S. Payan, M. Maglione, and A. Klein, "Surface segregation in Nb-doped $BaTiO_3$ films," *Applied Surface Science*, vol. 256, pp. 6228–6232, 2010.

[156] I. K. Naik and T. Tien, "Electrical Conduction in Nb_2O_5-Doped Cerium Dioxide," *Journal of The Electrochemical Society*, vol. 126, pp. 562–566, 1979.

[157] M. V. Frischbier, H. F. Wardenga, M. Weidner, O. Bierwagen, J. Jia, Y. Shigesato, and A. Klein, "Influence of dopant species and concentration on grain boundary scattering in degenerately doped In_2O_3 thin films," *Thin Solid Films*, vol. 614, pp. 62–68, 2016.

[158] M. Weidner, J. Jia, Y. Shigesato, and A. Klein, "Comparative study of sputter-deposited SnO_2 films doped with antimony or tantalum," *physica status solidi (b)*, vol. 253, pp. 923–928, 2016.

[159] K. Ellmer, A. Klein, and B. Rech, "Transparent Conductive Zinc Oxide: Basics and Applications in Thin Film Solar Cells," *Springer-Verlag Berlin Heidelberg*, 2008.

[160] X. Guo and R. Waser, "Electrical properties of the grain boundaries of oxygen ion conductors: Acceptor-doped zirconia and ceria," *Progress in Materials Science*, vol. 51, pp. 151–210, 2006.

[161] J. Luo, "Interfacial engineering of solid electrolytes," *Journal of Materiomics*, vol. 1, pp. 22 –32, 2015.

[162] S. Kim and J. Maier, "On the Conductivity Mechanism of Nanocrystalline Ceria," *Journal of the Electrochemical Society*, vol. 149, pp. 73–83, 2002.

[163] R. A. De Souza, "Oxygen Diffusion in $SrTiO_3$ and Related Perovskite Oxides," *Advanced Functional Materials*, vol. 25, pp. 6326–6342, 2015.

[164] T. H. Wan, M. Saccoccio, and F. Ciucci, "Assessing the Identifiability of k and D in Electrical Conductivity Relaxation via Analytical Results and Nonlinearity Estimates," *Oral presentation at the 21st International Conference on Solid State Ionics*, Padua, Italy, June 2017.

[165] R. De Souza, J. Kilner, and J. Walker, "A SIMS study of oxygen tracer diffusion and surface exchange in $La_{0.8}Sr_{0.2}MnO_{3+\delta}$," *Materials Letters*, vol. 43, pp. 43–52, 2000.

[166] R. A. De Souza and M. Martin, "Using $^{18}O/^{16}O$ exchange to probe an equilibrium space-charge layer at the surface of a crystalline oxide: method and application," *Physical Chemistry Chemical Physics*, vol. 10, pp. 2356–2367, 2008.

[167] M. Frischbier, "Die elektrischen Eigenschaften von Indiumoxid-Dünnschichten: in-situ Hall-Effekt-Messungen zur Aufklärung des Einflusses von Punktdefekten und Korngrenzen," *Technische Universität Darmstadt*, 2015.

[168] A. Wachau, "Sauerstoffaustausch polykristalliner kathodenzerstäubter Indiumoxid-Dünnschichten," *Technische Universität Darmstadt*, 2015.

[169] T. J. Bayer, A. Wachau, A. Fuchs, J. Deuermeier, and A. Klein, "Atomic Layer Deposition of Al_2O_3 onto Sn-Doped In_2O_3: Absence of Self-Limited Adsorption during Initial Growth by Oxygen Diffusion from the Substrate and Band Offset Modification by Fermi Level Pinning in Al_2O_3," *Chemistry of Materials*, vol. 24, pp. 4503–4510, 2012.

[170] A. Klein, "Energy band alignment at interfaces of semiconducting oxides: A review of experimental determination using photoelectron spectroscopy and comparison with theoretical predictions by the electron affinity rule, charge neutrality levels, and the common anion rule," *Thin Solid Films*, vol. 520, pp. 3721–3728, 2012.

[171] J. Maier, "Ionic conduction in space charge regions," *Progress in Solid State Chemistry*, vol. 23, pp. 171–263, 1995.

[172] C. E. Mortimer and U. Müller, "Chemie, Das Basiswissen der Chemie," *Georg Thieme Verlag, Stuttgart, 8. Auflage*, 2003.

List of Abbreviations

A	acceptor
a	lattice parameter
AFM	atomic force microscopy
ALD	atomic layer deposition
arb. units	arbitrary units
BE_{VBM}	binding energy of the valence band
γ	surface energy
cat.	cation
c(A)	acceptor concentration
$c(Ce^{3+})$	Ce^{3+} concentration
c(D)	donor concentration
c_{eff}(A)	effective acceptor concentration
c_i	concentration of element i
c(O)	concentration of oxygen
CTL	charge transition level
D	donor
D	diffusion coefficient
d	film thickness
D^*	tracer diffusion coefficient
DAISY-MAT	Darmstadt's Integrated System for Materials Reserach
D_{chem}	chemical diffusion coefficient
D_i	self diffusion coefficient via an interstitial mechanism
DOS	density of states
D_v	self diffusion coefficient via a vacancy mechanism
E	energy
E_a	activation energy
$E_{a,\sigma}$	activation energy of the conductivity
E_B	binding energy
E_{CBM}	energy level of the conduction band minimum
E_F	Fermi energy
$E_{F,qu}$	quenched Fermi level
E_g	band gap
E_{VBM}	energy level of the valence band maximum
E_{vac}	vacuum energy level
fcc	face centered cubic

f_i	tracer correlation factor
f_m	matching factor
FWHM	full width at half maximum
G_{AF}	Gibb's free energy of Anti-Frenkel reaction
GDC	gadolinia-doped ceria
GDC1	gadolinia-doped ceria with 1 wt.% Gd_2O_3
GDC10	gadolinia-doped ceria with 10 wt.% Gd_2O_3
G_{red}	Gibb's free energy of the reduction reaction
θ	diffraction angle
H_{AF}	enthalpy of Anti-Frenkel reaction
H_{mig}	migration enthalpy
H_{red}	enthalpy of the reduction reaction
H_{red-AF}	difference between H_{red} and H_{AF}
HREM	high resolution electron microscopy
I_i	integrated intensity of emission line of element i
I_P	ionization potential
ITO	tin dopes indium oxide
k	surface exchange coefficient
k^*	tracer exchange coefficient
K_{AF}	equilibrium constant of the Anti-Frenkel reaction
k_{chem}	chemical exchange coefficient
K_i	reaction rate constant of reaction i
K_{red}	equilibrium constant of the reduction reaction
LSMO	$La_{0.7}Sr_{0.3}MnO_3$
μ_d	electrical dipole moment perpendicular to the surface
m_e	electron mass
m_e^*	effective electron mass
m_h^*	effective electron hole mass
n	charge carrier density of electrons
N_C	effective density of states in the conduction band
NDC	niobia-doped ceria
N_V	effective density of states in the valence band
p	electron hole concentration
PES	photoelectron spectroscopy
PLD	pulsed lases deposition
pO_2	oxygen partial pressure
$pO_{2,ex}$	exchange oxygen pressure
PTFE	polytetrafluoroethylene
σ	conductivity
σ_e	electronic conductivity
σ_i	ionic conductivity
S_{AF}	entropy of the Anti-Frenkel reaction
S_i	atomic sensitivity factor of element i
SIMS	secondary ion mass spectrometry
SOFC	solid oxide fuel cell
S_{red}	entropy of the reduction reaction

T	temperature
T_{ex}	exchange temperature
T_m	measuring temperature
UDC	nominally undoped ceria
UPS	ultraviolet photoelectron spectroscopy
ϕ	work function
ϕ_{UPS}	work function obtained from UPS measurement
ϕ_{XPS}	work function obtained from I_P from UPS and BE_{VBM} from XPS
XPS	X-ray photoelectron spectroscopy
XRD	X-ray diffraction
XRR	X-ray reflectivity
χ	electron affinity
ω_0	thermodynamic factor

List of Figures

List of Tables

Résumé

Hans Florian Wardenga
born 17.09.1990 in Erkelenz

Professional Experience

05/2018 - today **Development Engineer**
eta plus electronics gmbh, Nürtingen

01/2014 - 12/2017 **Research Assistant**
Surface Science Division, Technische Universität Darmstadt

Education

01/2014 - today **Doctoral Studies**
Technische Universität Darmstadt, Surface Science Division
Title of Thesis: "Surface potentials of ceria and their influence on the surface exchange of oxygen"

10/2011 - 12/2013 **Master's degree Materials Science**
Technische Universität Darmstadt
Degree: Master of Science
Title of Thesis: "Characterization of Zr and H doped In_2O_3 films deposited by radio frequency magnetron sputtering"

10/2008 - 09/2011 **Bachelors's degree Materials Science**
Technische Universität Darmstadt
Degree: Bachelor of Science
Title of Thesis: "Deintercalation of sodium and intercalation of water in Na_xCoO_2 thin films made by pulsed laser deposition technique"

08/1999 - 06/2008 **Cusanus Gymnasium Erkelenz**
Degree: Abitur

List of Publications

2014 F. Muench, U. Kunz, H. F. Wardenga, H.-J. Kleebe and W. Ensinger, “Metal Nanotubes and Nanowires with Rhombohedral Cross-Section Electrolessly Deposited in Mica Templates”, *Langmuir*, vol. 30, pp. 10878-10885, 2014.

2015 H. F. Wardenga, M. V. Frischbier, M. Morales-Masis and A. Klein, “In Situ Hall Effect Monitoring of Vacuum Annealing of In_2O_3:H Thin Films”, *Materials*, vol. 8, pp. 561-574, 2015.

2016 H. F. Wardenga and A. Klein, “Surface potentials of (111), (110) and (100) oriented CeO_{2-x} thin films”, *Applied Surface Science*, vol. 377, pp. 1-8, 2016.

M. V. Frischbier, H. F. Wardenga, M. Weidner, O. Bierwagen, J. Jia, Y. Shigesato and A. Klein, “Influence of dopant species and concentration on grain boundary scattering in degenerately doped In_2O_3 thin films”, *Thin Solid Films*, vol. 614, pp. 62-68, 2016.

J. Deuermeier, H. F. Wardenga, J. Morasch, S. Siol, S. Nandy, T. Calmeiro, R. Martins, A. Klein and E. Fortunato, “Highly conductive grain boundaries in copper oxide thin films”, *Journal of Applied Physics*, vol. 119, no. 235303, 2016.

J. Morasch, H. F. Wardenga, W. Jaegermann and A. Klein, “Influence of grain boundaries and interfaces on the electronic structure of polycrystalline CuO thin films”, *Physica Status Solidi A*, vol. 213, pp. 1615-1624, 2016.

2019 S. P. Waldow, H. Wardenga, S. Beschnitt, A. Klein and R. A. De Souza, “The Concentration and Diffusivity of Oxygen Interstitials in Niobia-Doped Ceria”, *Journal of Physical Chemistry C*, vol. 123, pp. 6340-6350, 2019.

Attended Workshops and Conferences

2014 European Materials Research Society Spring Meeting 2014, Lille
"In-situ Hall-effect monitoring of vacuum annealing of In_2O_3:H_2O thin films" Hans F. Wardenga, Mareike V. Hohmann, Andreas Klein. *Oral presentation*

International Symposium on Transparent Conductive Materials 2014, Crete
"In-situ Hall-effect monitoring of vacuum annealing of In_2O_3:H_2O thin films" Hans F. Wardenga, Mareike V. Hohmann, Andreas Klein. *Oral presentation*

2015 International Conference on Electroceramics 2015, State College, PA
"In-situ Photoelectron Spectroscopy of Differently Oriented CeO_2 Thin Films Deposited by Magnetron Sputtering", Hans F. Wardenga, Kai Kühne, Andreas Klein. *Oral presentation*

Workshop on Ceria-based Materials in Catalysis and Electrochemistry, Ebsdorfergrund
"In-situ Photoelectron Spectroscopy of Differently Oriented CeO_2 Thin Films Deposited by Magnetron Sputtering", - Hans F. Wardenga, Rabea Zeuch, Kai Kühne, Andreas Klein. *Poster presentation*

2016 European Materials Research Society Spring Meeting 2016, Lille
"Electrical conduction in differently doped CeO_2 thin films", Hans F. Wardenga, Stephan Waldow, Roger A. de Souza, Andreas Klein. *Oral presentation*

"Surface Properties of Differently Oriented CeO_2:Gd and CeO_2:Nb Thin Films" Determined by Photoelectron Spectroscopy", Hans F. Wardenga, Katharina Schuldt, Andreas Klein. *Poster presentation*

2017 21st International Conference on Solid State Ionics 2017, Padua
"Electrical conductivities and Fermi level positions of ceria thin films: Comparisons between experiment and theory", Hans F. Wardenga, Stephan Waldow, Roger A. de Souza, Andreas Klein. *Oral presentation*

"Fermi level in Gd doped ceria thin films", Hans F. Wardenga, Katharina Schuldt, Andreas Klein. *Oral presentation*

Danksagung

An erster Stelle bedanke ich mich bei **Prof. Andreas Klein** für die Annahme als Doktorand und für das interessante Forschungsthema. Vorallem danke ich dir aber für die großzügigen Freiheiten bei der Bearbeitung des Themas, dafür, dass du mich auch mal einfach hast “machen lassen”, selbst wenn sich mein Interesse mal auf Nebenschauplätze des eigentlichen Themas konzentrierte, dem damit entgegengebrachten Vertrauen und dafür, dann in den notwendigen Momenten stets für Diskussionen und Rat zur Verfügung gestanden zu haben.

Prof. Wolfgang Ensinger danke ich für die Übernahme des Zweitgutachtens.

Unseren Projektpartnern vom IPC an der RWTH Aachen, **Prof. Roger De Souza** und **Stephan Waldow**, danke ich für intensive Diskussionen, SIMS Messungen und die produktive Kooperation. Ebenso bedanke ich mich für die freundliche Aufnahme in die Gruppe während meines Aufenthalts in Aachen.

Rabea Zeuch danke ich für ihre engagierte und zuverlässige Unterstützung bei der Herstellung und Vermessung von Proben. **Dominik Dietz** danke ich für AFM Messungen. Ich bedanke mich bei den von mir betreuten Studenten **Kai Kühne** für die guten Vorarbeiten zur CeO_2 Schichtabscheidung und insbesondere bei **Katharina Schuldt** für die vielen guten Daten zu Gd-dotiertem Ceroxid.

Danke an die gesamte Gruppe der **Oberflächenforschung** für die anregenden wissenschaftlichen Diskussionen, die weniger wissenschaftlichen Diskussionen in der freitäglichen Zopf-Runde, die tollen Seminarwochen in La Clusaz und gemeinsamen Konferenzbesuche. Insbesondere danke ich der Untergruppe **Halbleitende Oxide** für die schöne Zeit im Labor und Büro, vorallem **Jan Morasch**, **Andreas H. Hubmann** und **Philipp Wendel**.

Der **MaWi-Werkstatt** danke ich für die schnelle Umsetzung von mechanischen Komponenten, vorallem danke ich **Jochen Rank** für die zahlreichen Tipps zum konstruieren. **Michael Weber** danke ich für die Hilfe bei Elektronik-Probleme.

Ich bin dankbar für meine Freunde, die mich in turbulenteren Zeitabschnitten aufgefangen haben und mich mit willkommener Zerstreuung und Ablenkung versorgt haben. Im besonderen danke ich: **Tanju**, **Ralph**, **Max**, **Rabea**, **Céline**, **Sandra**, **Silke** und dem **Christian**.
Für die Möglichkeit zum regelmäßigem Frustabbau möchte ich allen meinen Sparrings- und Trainingspartnern herzlich danken.

Mein besonderer Dank gilt meiner **Lisa** für die vielen Tage, die du mit Jonathan aus unserer Wohnung 'geflüchtet' bist um mir den nötigen Raum zu schaffen diese Arbeit fertig zu bekommen. Danke, dass du mir immer durch meine Frustrationen geholfen hast, wenn wieder etwas nicht so lief oder deutlich länger dauerte als gedacht. Vielen Dank für das Licht.

Meinen **Eltern** danke ich für ihre Unterstützung und ihren Rückhalt.

Desweiteren möchte ich Jedem danken, der in irgendeiner Weise zum Erfolg dieser Arbeit beigetragen hat, ich aber vergessen habe an dieser Stelle namentlich zu erwähnen.